STRUCTURAL INVESTIGATION OF THE ODESSA METEORITE CRATER USING HIGH RESOLUTION GEOPHYSICS IN A COMPLEX ENVIRONMENT

A Thesis

by

CHARLES EDWARD STANFORD

Submitted to the Office of Graduate and Professional Studies of
Texas A&M University
in partial fulfillment of the requirements for the degree of

MASTER OF SCIENCE

Chair of Committee,	Mark E. Everett
Committee Members,	Masako Tominaga
	Jean-Louis Briaud
Head of Department,	Michael Pope

August 2017

Major Subject: Geophysics

ABSTRACT

From its discovery in 1921, the Odessa Meteorite Crater has interested researchers and mining companies who had initially hoped to locate a buried mass of meteoric iron. To find the impactor, a major geologic study of the crater was conducted in 1941. Even though the impactor has not been found, the thorough geologic constraints make the crater an excellent location to test the application of near-surface geophysical methods to complex environments. Recently, researchers have focused on determining the age of the crater, the environmental effects of the impact, and the size, incident angle, and direction of the impactor responsible for the crater. However, the heavily eroded and anthropogenically modified state of the exposed crater presents several challenges to impactor attribute estimation. The exposed rim is irregular in shape such that the original size and shape of the crater is indeterminate, only ~3 m of the estimated 30 m of original crater depth remain unfilled by post impact sediment, and previous geologic studies have left the remains of several large trenches transecting the crater rim.

To more accurately determine the original size of the crater, ERT and GPR geophysical methods were used to image the exposed and unexposed rim strata. However, the geologic complexity of the crater and the presence of anthropogenic or "cultural" noise posed problems to both ERT and GPR data acquisition and processing. Geophysical results point to a main crater of ~120 m in diameter and ~35 m depth. Additionally, the eastern non-circular portion of the expose crater rim is hypothesized to have form from the simultaneous impact of a small meteorite broken from the main meteorite during atmospheric entry. Further ERT study is recommended to investigate the secondary crater further.

DEDICATION

I would like to dedicate this thesis to my parents, Chand and Sandra, who have constantly provided their love, care, and support. This work, and all of my past accomplishments would not have been possible without them.

I would also like to dedicate this thesis to Thomas E Rodman. Tom, and his generous donations to the crater and its museum through the years have preserved the crater for future studies and helped attract the surprising number of visitors.

ACKNOWLEDGEMENTS

While this work is the accumulation of my master's studies, there are several critical individuals who made this possible that I must acknowledge. I would like to thank the professors of the Texas A&M Geology and Geophysics Department, who have made my six years in both my undergraduate and masters program an excellent experience. I would like to thank all my friends (and our weekly happy hours) who have made the last few years enjoyable. I would also like to thank my committee members Dr. Masako Tominaga and Dr. Jean-Louis Briaud whose insightful comments and discussion helped polish this work. Most importantly I would like to thank Dr. Mark Everett for all that he has done for this project and for me in general. Dr. Everett is largely responsible for me becoming the geophysicist that I am today. His near-surface geophysics class my junior year revealed the world of geophysics, his direction during our many projects together has revealed insights that only the most intelligent could provide, and he has been a constant role model for how to conduct myself as a professional. I hope to someday be half the geophysicist that Dr. Everett has become.

CONTRIBUTORS AND FUNDING SOURCES

Contributors

This work was supervised by a thesis committee consisting of Professors Mark E. Everett [chair] and Masako Tominaga of the Department of Geology and Geophysics and Professor Jean-Louis Briaud of the Department of Civil Engineering.

Data collection for this thesis was assisted by Dr. Mark E. Everett, Roy Bowling, Matthew Couchman, Andrea Darrh, Simon Murillo, and Tyler Ruchala. Several sections of the matlab GPR processing code, were adapted from code written by Roy Bowling.

All other work conducted for the thesis was completed by the student independently.

Funding Sources

Field work of this thesis was partially supported by a grant ($650) from Texas A&M University Scholars program and from the Howard Karen Research Fund. Tom Rodman provided lunch on several occasions during geophysical field work. There were no other outside funding contributions to acknowledge related to the research and compilation of this document.

NOMENCLATURE

ERT	Electrical Resistivity Tomography
GPR	Ground Penetrating Radar
MEM	Micro-erosion Meter
Tx	Transmitter
Rx	Receiver
OSL	Optically Stimulated Luminescence
Az	Azimuth

TABLE OF CONTENTS

Page

LIST OF FIGURES

LIST OF TABLES

Page

1. INTRODUCTION

The impact of a meteorite with the earth's surface can be one of the most powerful and devastating natural process. The energy released from a meteorite impact can be responsible for local, regional, and even global level extinction events, and have significantly shaped the history of the earth. It is crucial to understand the size and energy release of an impacted meteorite to determine its environmental effect. Accurate estimation of the impactor responsible for the formation of the Odessa Meteorite Crater will allow for more accurate estimation of the environmental impacts of this, and other meteorite impacts throughout the world.

1.1 Research Problem

Unlike most craters, the Odessa Meteorite Crater is not circular, with the exposed rim of the crater ranging from 160-190 m in diameter (Figure 1). It has been proposed by *Holliday et al.* (2005) that the crater is the result of an oblique impact, in order to explain the crater's low depth to diameter ratio (0.16 rather than the expected .25-.33 (*Melosh*, 1989)) and the estimated low impact velocity of the meteorite (*Holliday et al.,* 2005; *Littlefield et al.*, 2007). The subsequent erosion of the original crater has largely been overlooked as a source of the abnormal depth to diameter ratio except by *Monnig and Brown* (1935).

The Odessa Meteorite Crater formed by an extraterrestrial impact estimated at 63.5 ± 4.5 ka (*Holliday et al.*, 2005). The crater morphology has experienced significant modification since its formation and the original depth has been reduced ~90% by lacustrine and aeolian sediment fill. It is well known that in general, the steep inner rim of a crater should erode at a faster rate than the gentle sloping outer rim (*Melosh,* 1989). This erosional pattern produces an apparent widening of a crater through time which, unaccounted for, could result in an overestimation of the impactor's size and energy release. It is clear from the sediment infill, irregular crater rim, and estimated age, in addition to the late Pleistocene-Holocene climate history, that the Odessa Meteorite Crater has experienced erosion and widening since its formation, but the overall evaluation on the amount of widening and the cause of the non-circular crater shape requires further study.

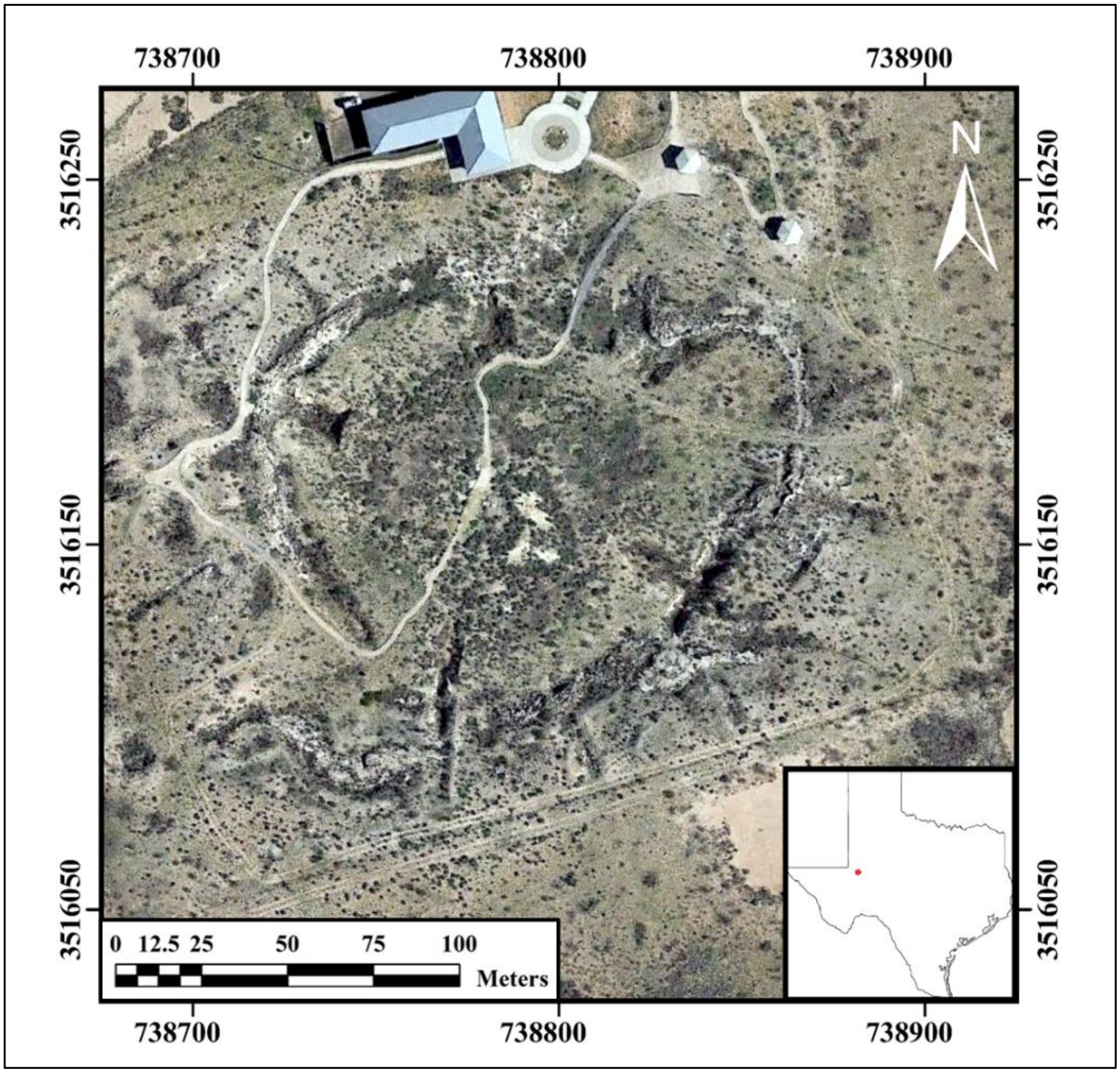

Figure 1 – Aerial map of the Odessa Meteorite Crater and surrounding area. Crater museum and associated infrastructure north of crater. Scale bar in lower left, inset map showing approximate location of the crater in lower right, and north arrow in top right. Easting and Northing UTM coordinates from zone 13N.

1.2 Study Objective

To enable the refinement of existing estimates of the impactor attributes, this study aims to determine the original size of the Odessa Meteorite Crater. This is accomplished mainly through the application and analysis of multiple near-surface applied geophysical techniques. Electrical resistivity tomography (ERT) was used to image the limestone rim of the crater and the fallback or ejecta fill which lined the original crater wall. The latter, not being continuously subaerially exposed to long-term weathering processes, is less susceptible to erosion and modification than the rim of the crater. Ground penetrating radar (GPR) was used to identify the sub-surface structure of the deformed crater rim strata. While the Odessa Meteorite Crater is well constrained geologically by previous studies, it presents severe environmental challenges that must be overcome to properly interpret data acquired with near-surface geophysical methods. At the Odessa Meteorite Crater, ERT interpretation is affected by electric currents flowing in near-surface heterogeneities, such as the highly resistive and fractured limestone rim, requiring careful "geologic noise" removal, while GPR analysis is affected by anthropogenic and environmental electromagnetic interference that must be removed with advanced filtering and imaging techniques.

2. BACKGROUND

Since the crater in Arizona, and the Odessa crater shortly after, were first confirmed to have been caused by impact, the study of meteorite impacts has developed significantly (*Barringer*, 1906; *Barringer Jr*, 1928). Studies began with simple descriptions of the geology and deformation associated with the impact (*Eugene Merle Shoemaker*, 1959; *E. M. Shoemaker and Eggleton*, 1961). Crater scaling equations were then derived from the study of nuclear explosions and the resulting craters, that resembled those formed by meteorite impacts (*Melosh*, 1989; *Nordyke*, 1962; *Schmidt and Housen*, 1987). Eventually, programs that considered fine scale details related to the impact, such as target rock type, meteorite composition, and impact obliquity, were developed that allowed for the simulation of an impact (*Littlefield et al.*, 2007; *O'Neill and Heine*, 2005; *Pierazzo et al.*, 1998; *Pierazzo and Melosh*, 1999). Further geophysical studies of remnant meteorite craters will attempt constrain attributes and reveal details to aid in impactor estimation that could not otherwise be known.

2.1 Impact Cratering

At first glance, the geologic process that forms impact craters appears simply to be a high-velocity collision of a meteorite with the earth resulting in large scale destruction similar to that caused by a large explosive device. However, the hypervelocities of the projectiles involved in common meteorite impacts can trigger complicated responses and stresses that are only being better understood and simulated recently with the increasing availability of hydrodynamic modeling codes that run on supercomputers (*Jutzi et al.*, 2008; *Pierazzo and Melosh*, 1999; *Wünnemann et al.*, 2006). Herein only the gross observable effects of the processes related to terrestrial non-marine impacts are considered since modeling the intricacies of the impact process is beyond the scope of this thesis and because the Odessa meteorite impacted a non-marine environment. A good compilation of the basic physics involved in the impact process can be found in H.J. Melosh's (1989) monograph "Impact Cratering A Geologic Process".

2.1.1 Impact stages

While the impact process is a single continuous event, attempts have been made to partition an impact event into distinct stages in order to conceptualize and identify the rapidly changing effects of an impact (*Gault et al.*, 1968). The contact and initial compression stage (Figure 2) begins with the first contact of the meteorite with the earth. As the meteorite impacts, the surface material is compressed and accelerated. Shock waves are generated from the point of impact within both the impactor and the impacted surface. In the impacted surface, the shockwaves propagate outward from the impact site at supersonic velocities that exceed those of elastic waves. The shockwaves simultaneously propagate upward through the impactor. The end of the contact and compression stage is marked by the shockwaves having completely propagated through the impactor and the resultant transfer of ~90% of the impactors kinetic energy to the impacted surface (*Melosh*, 1989).

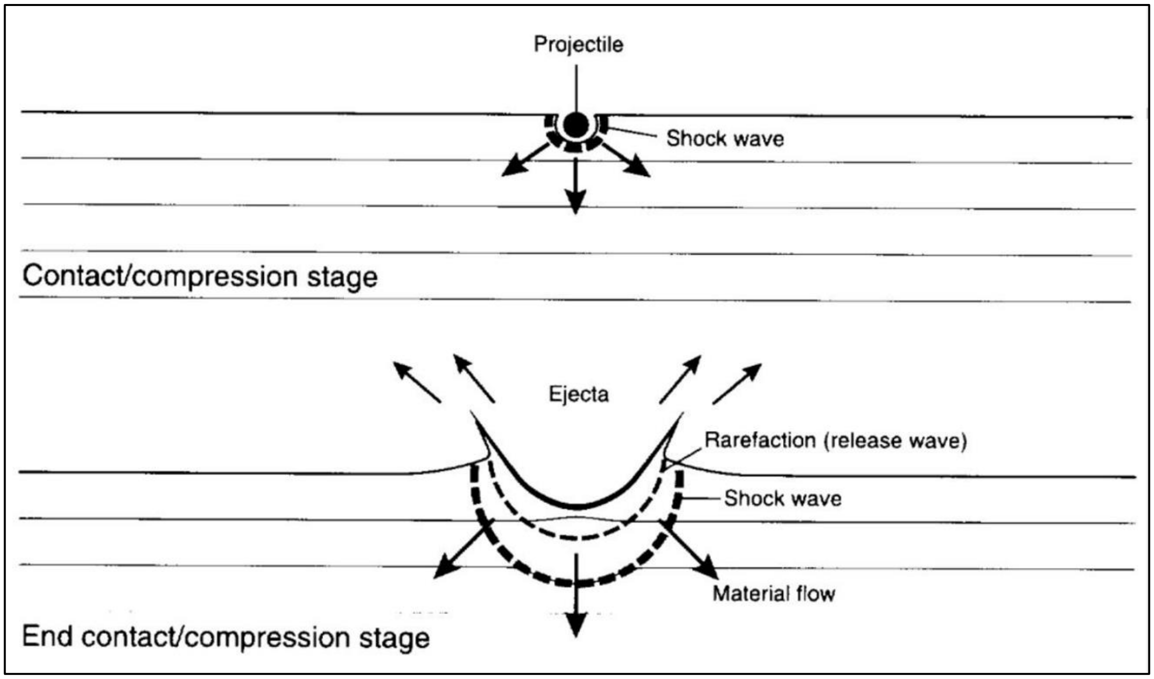

Figure 2 – Contact and compression impact stage. Top - initiation of contact and compression stage as the shockwave begin propagation. Bottom – End of contact and compression stage as rarefaction wave completes upward propagation. Modified from French (1998).

The excavation stage (Figure 3) follows the end of the contact and compression stage as the shockwave continues to propagate through the impacted surface material. The supersonic shock wave eventually weakens to an elastic wave as energy is lost due to plastic deformation of the rock. Prior to the transition from a shockwave to an elastic wave, the propagating shock-front induces an upward-directed pressure gradient within the material it passes through, resulting in the ejection of debris from the crater into the air. The ejected material then falls back to earth, inside an area including and surrounding the impact zone. Debris that falls within the crater is termed "ejecta fill" while debris that falls outside the impact zone is called "ejecta blanket." The “transient crater” is the result of the excavation stage and is generally many times larger than the size of the impactor (*Melosh*, 1989).

The modification stage (Figure 4) begins after the completion of crater excavation. In this stage, the “transient crater” becomes further modified by a wide range of geologic processes operating at varying time scales. Modifications can include debris slides along the crater wall, the uplift of central peaks and formation of slump terraces especially in large craters, continuous weathering and erosion of the exposed crater rim, and filling of the crater basin with sediments (*Melosh*, 1989). It is worth noting that because the shockwave propagates radially outward from the point of impact, only extremely oblique impacts (impact angle less than ~10°) or extensive geologic heterogeneity will cause the resulting crater to deviate from the circular shape observed in almost all craters (*Melosh*, 1989). The effect of obliquity of an impact is primarily to reduce the amplitude of the shockwave and decrease its penetration depth (*Melosh*, 1989).

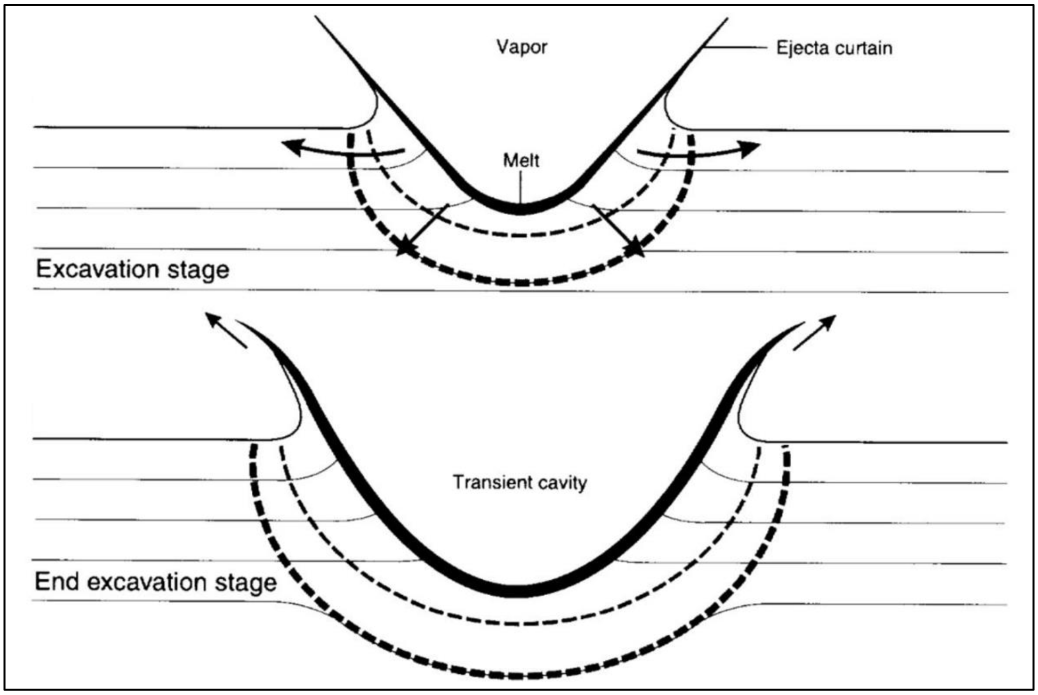

Figure 3 – Excavation Impact Stage. Top – beginning of excavation stage as shockwave sets target material in motion, ejecting it from the crater. Bottom – end of excavation stage as shockwave attenuates to elastic wave and transient crater is formed. Modified from French (1998)

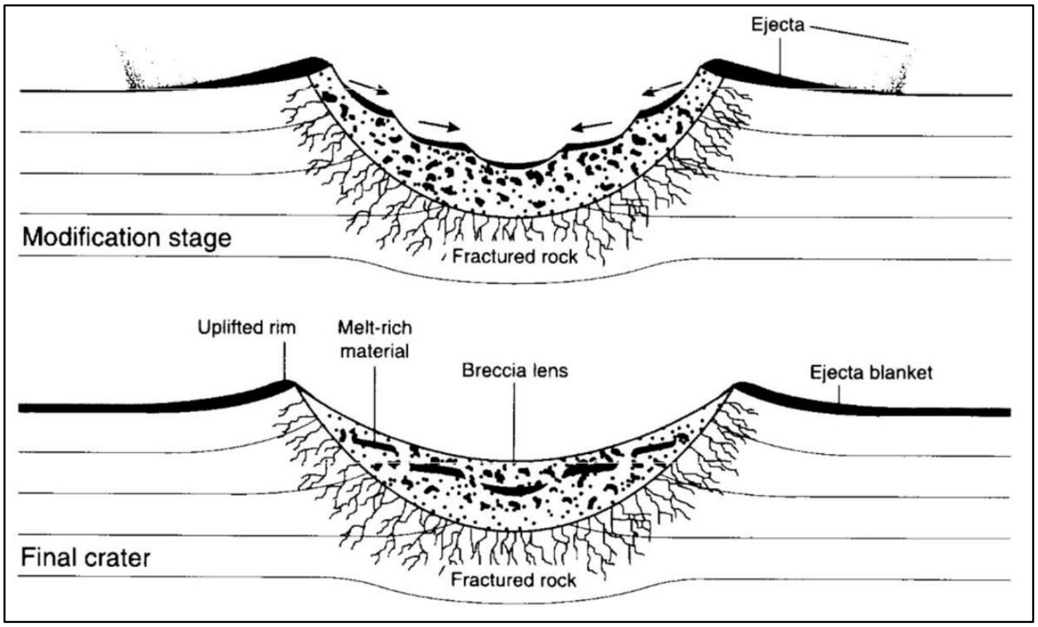

Figure 4 – Modification impact stage. Top – start of modification stage as modification of transient crater begins. Bottom – end of modification stage as crater reaches its final form. Modified from French (1998)

2.1.2 Simple vs. complex craters

A crater resulting from the impact process can be classified into complex or simple morphology categories. Simple craters refer to the bowl-shaped craters formed by small impactors (Figure 5, *top*). Such craters lack the distinctive features of larger complex craters (Figure 5, *bottom*). Depending on the impacted material properties, simple craters can reach a critical size of 4 km (*Grieve*, 1987). Simple craters can be further refined into two sub-categories. The “Barringer type” crater (Figure 6, *A*) is characterized by overturned or inverted strata within the crater rim resulting from high impact velocities and deep penetration of the impactor (*E. M. Shoemaker and Eggleton*, 1961). The “Odessa type” crater (Figure 6, *B*) is formed by slower velocity impacts that push back the existing strata, typically causing thrust faults and small folds in the crater rim (*E. M. Shoemaker and Eggleton*, 1961). Unfortunately, the small size of simple craters makes them susceptible to environmentally dependent erosional forces and relatively few are still exposed or reserved in the rock record.

Complex craters are larger craters marked by slump terraces, central peaks of uplifted basement rock, and multiple peak rings especially in the largest craters. Complex craters are geological evidence of devastating impacts in Earth’s past that caused widespread environmental effects. The processes of gravitational collapse and basement rebound determine the transition from simple to complex morphologies. The size at which this transition occurs has been found to scale inversely with the strength of gravity on the impacted planetary body (i.e. 4 km on earth) (*Melosh*, 1989). The shape of complex craters departs from the smooth, bowl shape of simple craters. The steep crater walls slump inward, enlarge the crater size, and flatten the floor of the crater. Large complex craters are often preserved in the rock record and can be studied long after erosion would have claimed smaller simple craters. Hildebrand (1998) studied the well-known and long-buried, complex Chicxulub Crater on the Yucatan Peninsula and inferred characteristics about the impactor ~65 Myr post-impact.

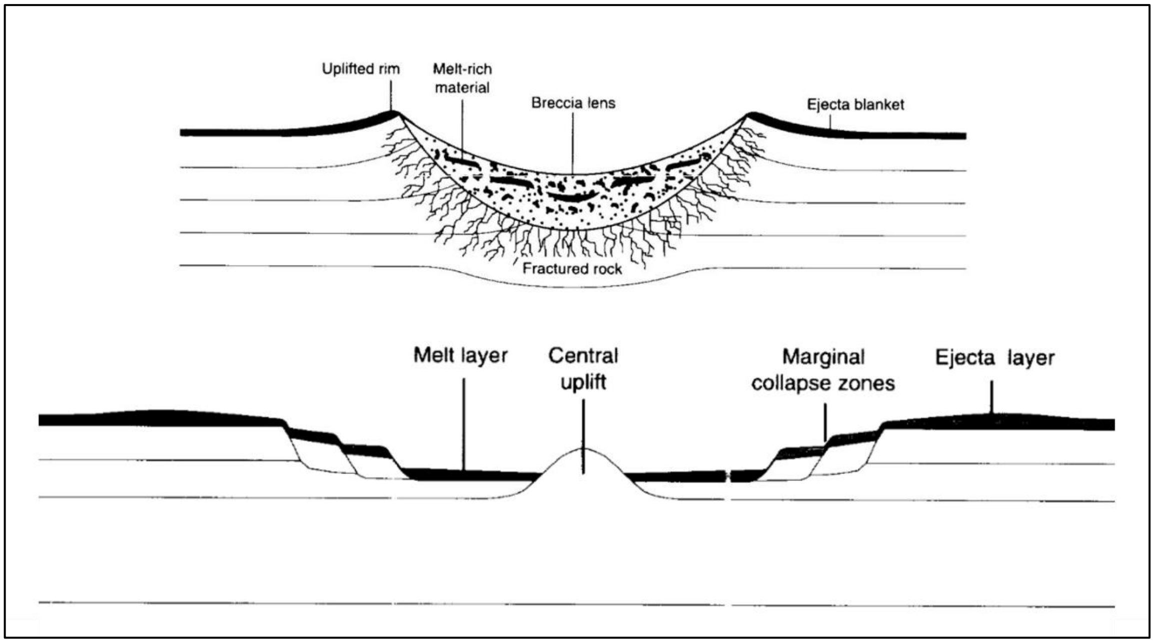

Figure 5 – Comparison of simple and complex crater morphologies. Top – general simple crater bowl shape. Bottom – general complex crater morphology. Notice central uplift and marginal collapse zones that typify complex craters. Figure not to scale. Modified from French (1998).

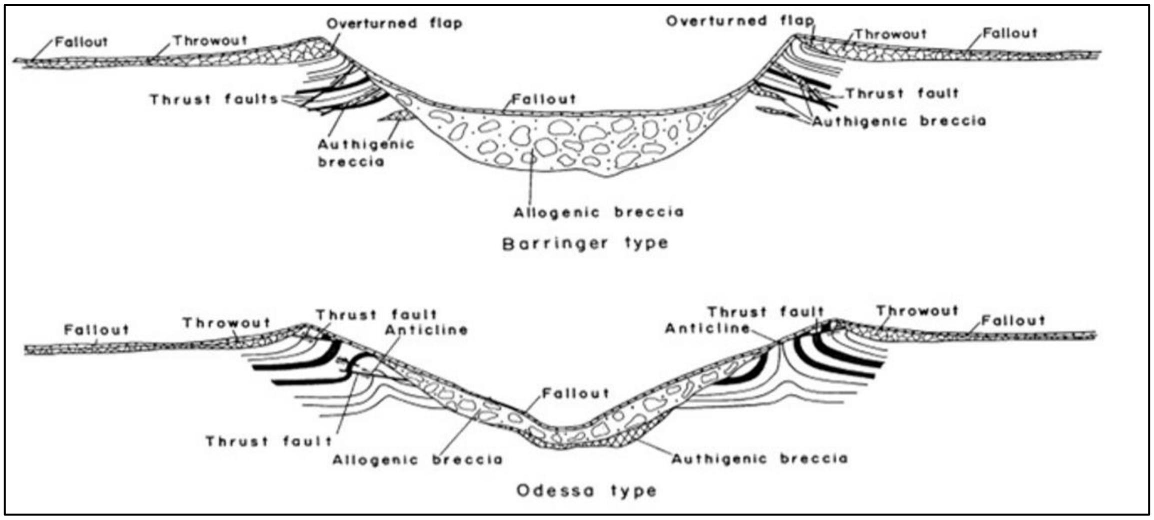

Figure 6 – Comparison of "Barringer" and "Odessa" simple crater subtypes. Top – Barringer crater subtype depicting overturned bedding. Bottom – Odessa crater subtype depicting thrust back bedding and associated anticlines. Modified from E. M. Shoemaker and Eggleton (1961)

2.1.3 Shock metamorphism

While geological and geophysical observations of disturbed strata and meteorite fragments often leads to a tentative conclusion that a crater was formed by a meteor impact, only evidence of shock metamorphism confirms that an impact has actually taken place. Shock metamorphism occurs from the high pressures, and especially the extreme pressure change rates, that are unique to meteorite impacts (*Chao*, 1966; *Stöffler*, 1971). Different forms of shock metamorphism can occur at different maximum pressures and can help estimate the maximum force of the impact. Shatter cones have a distinctive conical deformation shape and are formed as shockwaves radiate outward from the point of impact with pressures of 2-30 GPa (*French*, 1998). Microscopic planar deformation features can be found in quartz grains subjected to pressures of 8-25 GPa (*French*, 1998). Coesite, a high-pressure polymorph of quartz, forms at pressures exceeding 30 GPa

(*French*, 1998). “Rock flour” is quartz in sandstones in which the grains have been pulverized into microscopic particles. While not a product of shock metamorphism in the strict definition, rock flour is commonly associated with the shock of the impact process (*Evans and Mear*, 2000).

2.2 The Odessa Meteorite Crater

The Odessa Meteorite Crater was discovered in 1921 when an Odessa rancher handed a small piece of iron ore to Dr. A. B. Bibbins of Baltimore for preliminary investigation. A detailed analysis conducted by Mr. E V. Shannon of the U.S. national museum showed that the chunk of iron ore was actually a fragment of an iron octahedrite meteorite (*Merrill*, 1922). This discovery, occurring shortly after the discovery in Arizona of the world’s first confirmed meteor crater (*Barringer*, 1906) immediately drew the interest of researchers; but it took several years to rule out other possible explanations and confirm that the geologic feature at Odessa from which the small piece of iron was extracted was indeed formed by a meteorite impact (*Barringer Jr*, 1928; *Bibbins*, 1926; *Sellards*, 1927).

The earliest field investigations showed that the Odessa Meteorite Crater is a complicated structure, with the diameter estimated at 161.5 m (530 ft) by *Barringer Jr* (1928) and 182.8 m (600 ft) by *Sellards* (1927); and 176.8 by 213.3 m (580 by 700 ft) by *Nininger* (1933), who recognized the non-circular shape. *Monnig and Brown* (1935) made the first attempt to definitively measure the crater diameter by making topographic measurements and they arrived at an approximately circular diameter of 167.6 m (550 ft).

However, they noted that “it is impossible to measure a diameter across the crater in many directions because of the broken down rim” (*Monnig and Brown*, 1935).

2.2.1 The Evans study of the Odessa Meteorite Crater

The geologic and economic interest in the Odessa Meteorite Crater motivated federal, state of Texas, and Ector County agencies to fund a $250,000 geologic expedition from 1939-1941 with the purpose of examining the crater and locating the meteorite (*Evans and Mear*, 2000). Geologist Glen L. Evans of The Bureau of Economic Geology headed the project with significant help from geologist Dr. E. H. Sellards, the director of the Bureau, at the time. There have been multiple written accounts of the investigations (*Evans*, 1961; *Sellards and Evans*, 1941), but the most detailed description was published almost 60 years after the completion of the investigation by *Evans and Mear* (2000). While the investigation was not successful in finding a massive meteorite body, the extensive bore holes, excavation trenches, and central mine shaft (Figure 7) allowed for a thorough geologic description of the meteorite crater and its associated deformation. The basic results of the Evans study are summarized below.

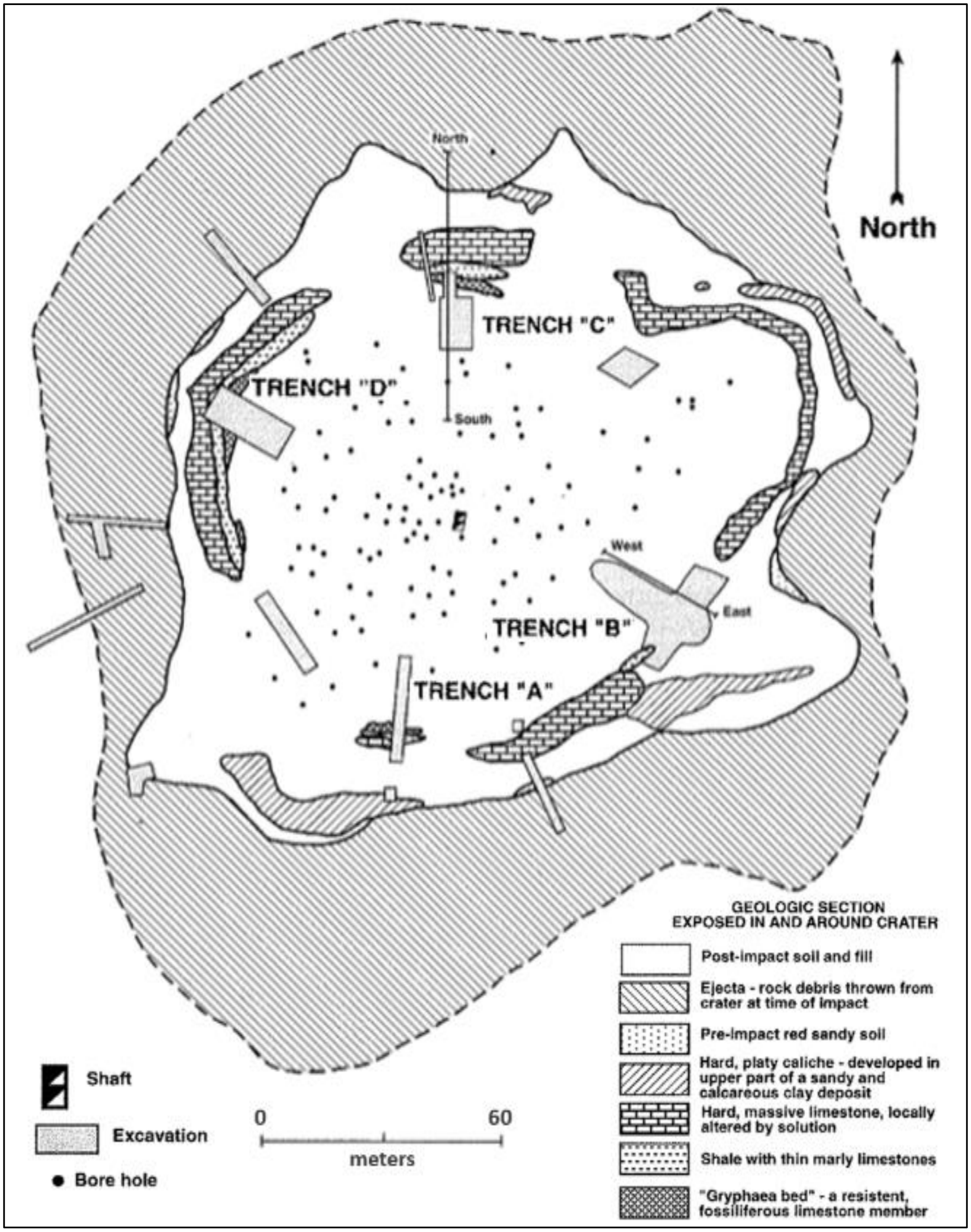

Figure 7 – Summary of excavations during the 1940 geologic study of the crater. Note locations of trenches B and C, and the extensive borehole locations within the crater. Modified from Evans and Mear (2000)

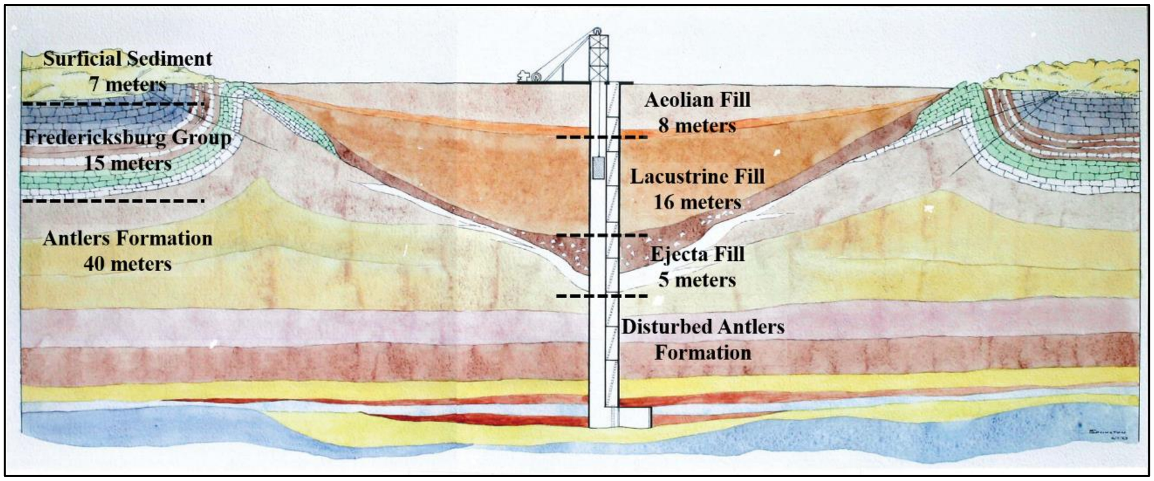

Figure 8 – Artistic cross section of the Odessa Meteorite Crater based on the Evan's geologic study. Dashed lines represent approximate boundaries between rock units. Artistic cross section not to scale.

The typical undisturbed strata (Figure 8) in the vicinity of the crater consists of 7 m of surface soil and caliche of the Cenozoic, 15 m of massive limestone and interbedded shale of the Cretaceous Fredericksburg Group, and 40 m of massive sandstone of the Cretaceous Antlers Formation, all underlain by Triassic and Permian formations (*Evans and Mear*, 2000). The crater rim is comprised of uplifted limestone of the Fredericksburg group. The rim lies ~1 m above the surrounding plain and ~2 m above the level of the crater basin fill. Within the crater, ~29 m of post-impact fill is divided into three distinct stratigraphic zones. The lowest zone of the post-impact fill consists of ~5 m of brecciated sandstone, limestone, and rock flour comprising the ejecta fill. The second zone consists of ~16 m of silty clay sediments in which the occurrence of invertebrate pond snail fossils indicate a lacustrine environment. The upper zone consists of ~8 m of aeolian silt, fine-grained colluvium, and several types vertebrate fossils from the late Pleistocene representing the shift to the arid environment of the present day (*Evans and Mear*, 2000).

Beneath the post impact crater fill, the ~21 m of the Antlers formation is exposed by the central mine shaft. The exposed section shows clear signs of the impact in many small offset (< 1m) fractures and block faults that are not found in boreholes drilled outside the crater. Shock metamorphism evidence is present at the Odessa Meteorite Crater in the form of rock flour and shatter cones. Boreholes within the crater (locations shown Figure 7) have detected rock flour in a ~75 m disc lining the base of the post-impact fill with a maximum thickness of 2 m in the center of the crater. Shatter cones have been found exposed on the surface of ejected boulders, but they are not abundant, as many of the exposed shatter cones would have been eroded since their formation. Coesite, a high pressure polymorph of quartz, has not been found at the Odessa Meteorite Crater which suggests that the maximum pressure of the impact was below 30 GPa (*Evans and Mear*, 2000).

Trenches excavated by *Evans and Mear* (2000) near, and sometimes transecting, the exposed rim of the crater have revealed a complex deformation structure caused by the impact. The erosional-resistant limestones of the Fredericksburg group were uplifted, folded, and thrusted from the point of impact. “Trench C” (Figure 9) displays deformed beds that are folded into an asymmetrical anticline and detached as thrust faults from the relatively intact strata beneath. “Trench B” (Figure 10) shows only uplift and folding of the Fredericksburg group formation without detachment. An anticline, or thrusting, is not found at this location and such deformed rocks must have been either ejected from the crater or have been completely eroded (*Evans and Mear*, 2000). Overall, the style of deformation found at Odessa is suggestive of a shallow-penetrating impactor that did not generate enough upward force to completely overturn the strata, unlike the projectile responsible for the formation of Meteor Crater, AZ (*E. M. Shoemaker and Eggleton*, 1961).

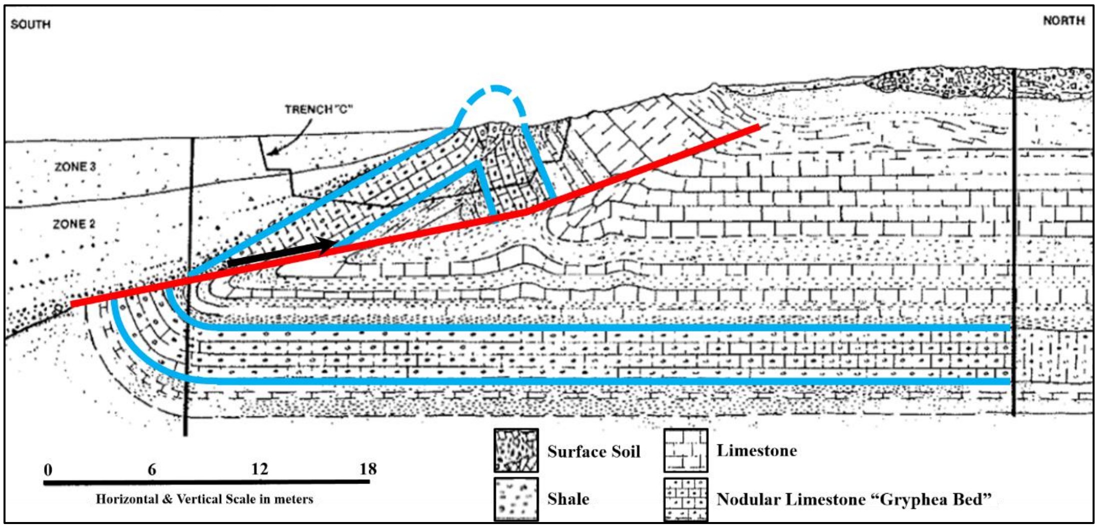

Figure 9 – Geologic cross section of trench C. Blue lines hilight folded and thrusted limestone bed. Red line shows location of thrust fault with direction of motion shown by black arrow. Black vertical lines show constraining borehole locations. Horizontal and vertical scale in lower left. Modified from Evans and Mear (2000).

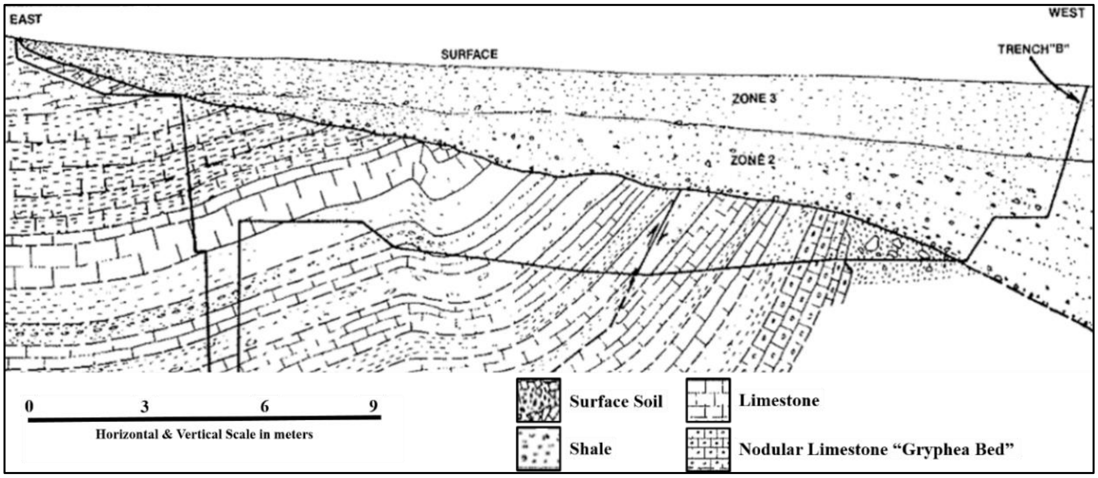

Figure 10 - Geologic cross section of trench B. Anticline and thrust fault absent in trench B. Horizontal and vertical scale in lower left. Modified from Evans and Mear (2000).

2.2.2 Recent studies of the Odessa Meteorite Crater

Holliday et al. (2005) dated the crater formation to 63.5 ± 4.5 ka via the optically stimulated luminescence (OSL) technique and estimated the size and environmental effects of the impact. These authors suggested that the symmetry of the ejecta blanket pointed to an impact inclination of ~45° and the low depth to diameter ratio of the crater pointed to a relatively slow impact hypervelocity (*Holliday et al.*, 2005). Using *Schmidt and Housen* (1987) pi-scaling techniques, *Holliday et al.* (2005) estimated the crater was formed by a 3-4 m meteorite striking at 7 km/s, which is equivalent to .5-5 kt of TNT. The maximum environmental effects of an impact this size (the 5 kt case) would have been limited to 2300 km/hr winds extending 180 m from the point of impact, 60 km/hr winds at 2 km distance, small mammal fatalities within 600 m, and a possible fireball up to 480 m from the point of impact (*Holliday et al.*, 2005).

Littlefield et al. (2007) simulated the Odessa Meteorite Crater impact from a numerical standpoint using the three-dimensional multi-material Eulerian hydrocode CTH described by *McGlaun et al.* (1990). *Littlefield et al.* (2007) was able to develop an advanced simulation of the impact process because of the extraordinary geologic constraints provided by the original geologic study. *Littlefield et al.* (2007) presented the results from four simulations with varying impactor attributes. The simulation parameters and resulting crater dimensions are summarized in Table 1. *Littlefield et al.* (2007) noted that the craters generated by simulations 1 and 2 do not predict uplift of the lower Fredericksburg units, unlike those of simulations 3 and 4. They concluded that the Odessa Meteorite Crater was formed by a highly oblique impact of 83.8° from vertical and that the meteorite was 9-15 m in size, much larger than previously thought (*Baldwin*, 1963; *Holliday et al.*, 2005).

It is clear that a more accurate description of the original crater dimensions is needed as estimates of the impact parameters vary substantially between *Holliday et al.* (2005) and *Littlefield et al.* (2007). The inconsistency can be attributed to the current eroded state of the crater and the lack of certainty regarding the original size of the crater.

Table 1 – Summary of simulations of impact at the Odessa Meteorite Crater by Littlefield (2007).

Simulation #	**Meteorite Diameter (m)**	**Meteorite Velocity (km/s)**	**Angle of Impact (° from vertical)**	**Crater Depth (m)**	**Crater Diameter (m)**
1	6.87	12	77	28	78
2	4.0	27	77	22	62
3	15.0	12	83.8	27	125
4	9.06	25.6	83.8	27	98

2.3 Limestone Weathering Rates

To assess the long-term effects of weathering and erosion on the crater rim, it is important to explore expected weathering rates. *Stephenson and Finlayson* (2009) compiled the results of various microerosion meter (MEM) studies from a wide range of environments, arriving at an average erosional rate of 0.752 mm/yr. However, the studies examined by Stephenson and coworkers can be split into studies that measured erosion on limestone bedrock averaging 0.0623 mm/yr (*Allred*, 2004; *Cucchi et al.*, 1994; *Cucchi et al.*, 1987; *Cucchi et al.*, 1996; *Forti*, 1984; *Furlani et al.*, 2009; *Kunaver*, 1979; *Smith et* *al.*, 1995; *Trudgill*, 1986) and studies using blocks of limestone exposed to various environments which averaged 6.132 mm/yr (*Liu et al.*, 2006; *Muhammad and Beng*, 2002). The variability in erosional rates found by *Stephenson and Finlayson* (2009) indicates that erosion is heavily dependent on environmental conditions. *Smith et al.* (1995) measured weathering rates on various limestones in eastern Australia, an environment that is similar to present-day Odessa. They found that limestone exposed in rivers weathered at rates of 0.2, 0.051, and 0.074 mm/yr depending on the measurement site (*Smith et al.*, 1995). They also found that limestone bedrock that was not directly exposed to a river system weathered more slowly, at average rates of 0.013 mm/yr (*Smith et al.*, 1995).

The magnitudes of these weathering rates are not entirely representative of the expected erosion rate of the limestone rim rocks at the Odessa Meteorite Crater. The environment of the Odessa region has not always been semi-arid, possibly higher precipitation occurred in the past throughout the late Pleistocene and Holocene (*Holliday*, 1991). The crater also contains substantial accumulations of lacustrine sediment (*Evans and Mear*, 2000) indicating that the crater contained standing water for an extended time period. Average weathering rates at Odessa are expected to exceed those of the exposed limestone bedrocks in Australia, but the rates should be lower than those of the bedrock in flowing rivers measured by (*Smith et al.*, 1995). It is important to note that the original uplifted crater rim would have been fractured and jointed, rather than the intact bedrock that was measured in the aforementioned studies. *Briaud* (2008), while investigating scour by flowing water, found that the erodibility of jointed bedrock can change several orders of magnitude depending on the spacing (and density) of joints or fractures. Thus, it is important to identify the fracture density of the uplifted crater rim in order to reasonably estimate the long-term average erosional rate.

3. METHODS

3.1 Electrical Resistivity Tomography

Electrical Resistivity Tomography (ERT), is a near-surface applied geophysical method that measures the electrical resistivity of the subsurface via the injection and withdrawal of DC electrical current. ERT systems essentially operate as a sensitive voltmeter to measure the electric potential that is generated by the injected current (*Everett*, 2013). ERT systems have the ability to make measurements that are sensitive to the electrical resistivity at different depths in the subsurface and have gained popularity over the various inductive electromagnetic methods which are more susceptible to non-uniqueness and signal-generated noise issues (*Commer and Newman*, 2009; *Ellis*, 1998; *Goldman et al.*, 1994; *Roy*, 1962). For a thorough description of ERT fundamentals and survey design see *Loke* (1999) or *Everett* (2013)

3.1.1 ERT general overview

Four electrode ERT systems operate by measuring the apparent resistivity (ρ_a) of the subsurface. In a four electrode configuration, a known current (I) is injected and withdrawn through two electrodes and the resulting voltage (V) is measured across two other electrodes. The apparent resistivity is calculated using equation (1), where κ is a geometric factor and Z, defined by equation (2) is the earth impedance. The geometric factor κ depends on the electrode array configuration including the electrode separation. Earth impedance Z depends on the electrical resistivity of the sub-surface being probed and dependent on the physical properties of the material (*Everett*, 2013).

$$\rho_a = \kappa Z \tag{1}$$

$$Z = \frac{V}{I} \tag{2}$$

Measurements that are sensitive to different sub-surface locations are made by varying the electrode injection and withdrawal points. The different measurements can then be combined to produce a “pseudosection” of apparent resistivity values (Figure 11) (*Everett*, 2013). In the pseudosection, apparent resistivity values are plotted at a point that lies spatially between the current electrode pair at a depth of half the electrode spacing. This point represents the approximate location of maximum sensitivity of the measurement (*Everett*, 2013). Surveys at the Odessa Meteorite Crater were conducted with the AGI R8/IP SuperSting earth resistivity meter with 112 electrodes arrayed in the dipole-dipole acquisition mode (Figure 12).

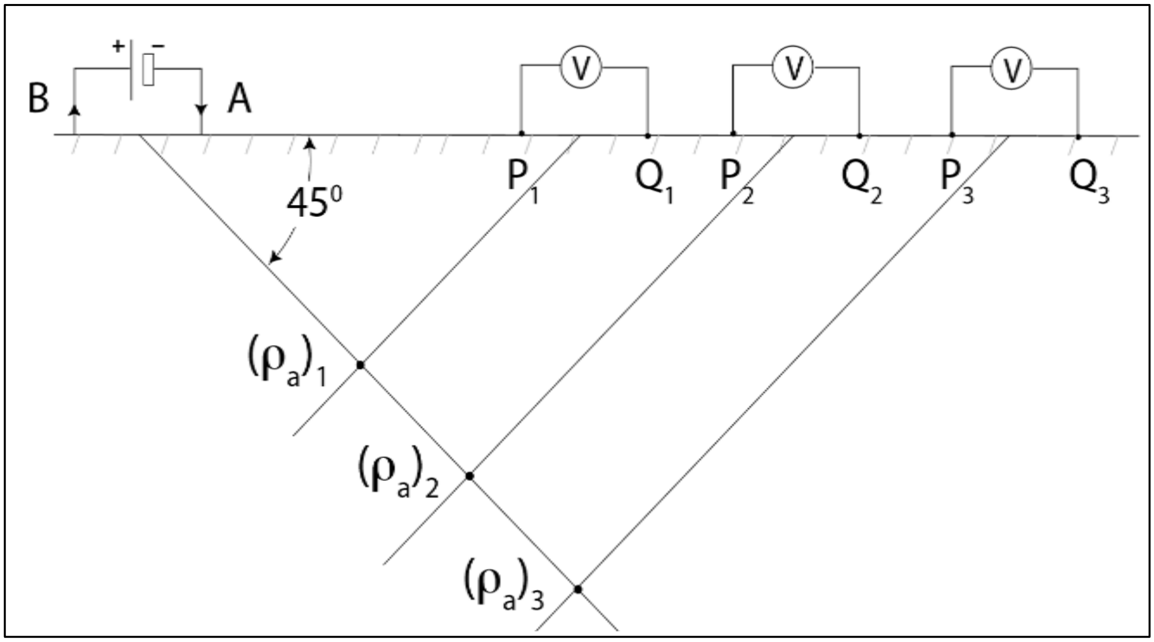

Figure 11 – Example of ERT pseudosection creation. Measured apparent resistivity values placed at the midpoint of current injection/withdraw electrodes and electrodes measuring voltage. From Everett (2013)

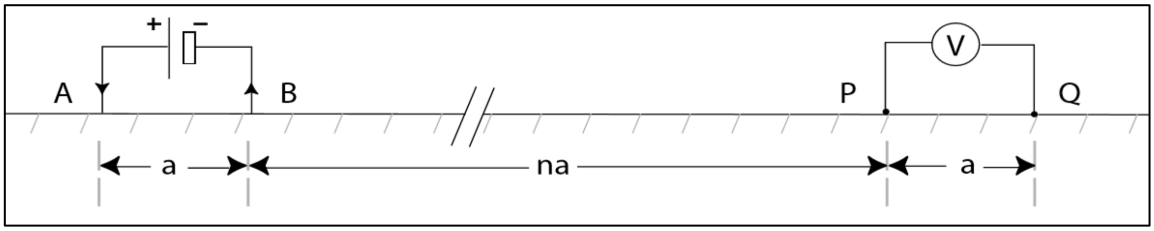

Figure 12 – Example of dipole-dipole ERT acquisition mode. Spacing variables "a" and "n" are varied throughout survey to change measurement depth and location. From Everett (2013)

3.1.2 ERT inversion and noise removal

The apparent resistivity pseudosection acquired in the field must be inverted to visualize the resistivity structure of the subsurface. The governing Laplace forward equations of DC resistivity are used to perform the inversion (*Inc.*, 2007). The ERT inverse problem is formulated as an underdetermined one, comprising more model parameters than measurements, and therefore some additional model constraint or a-priori information should be used to find an optimal solution for the given geologic environment under study. Damped least squares inversion attempt to minimize the data misfit in an iterative approach. “Smooth” or “Occam’s razor” inversion methods attempt to find the smoothest resistivity structure possible that fits the data to some pre-defined tolerance. “Robust” or “blocky” inversion methods attempt to minimize the L1-norm (as opposed to the L-2 norm in the smooth method) resulting in a rougher, blocky model that also fits the data to a pre-defined tolerance.

The highly resistive limestone rim rocks present at the Odessa Meteorite Crater creates electrode ground coupling issues that cause extraneous noise during the ERT data collection. Measurements contaminated by such coupling noise were removed carefully in order to obtain accurate images of the sub-surface resistivity structure that could not be obtained without noise removal. Additionally, a-priori knowledge, derived from the Evans geologic study of the crater, was supplied as a starting model to the *EarthImager 2D* tomographic inversion software (*Inc.*, 2007). The a-priori knowledge helped provide a more realistic resistivity distributions than would be obtained without such knowledge, therefore increasing confidence in the inversion results.

3.2 Ground Penetrating Radar

Ground-penetrating radar (GPR) is a near-surface applied geophysical method that records the response of transmitted electromagnetic waves to dielectric permeability contrasts in the non-magnetic sub-surface (*Davis and Annan*, 1989). GPR typically operates at frequencies of 10-1000 MHz providing high vertical resolution of the near-surface to ~1-30 m depths. GPR has become a popular geophysical method because of its similarity to seismic in the data processing workflow and the resulting time and depth sections (*Everett*, 2013).

3.2.1 GPR overview

GPR operates on the principle that transmitted electromagnetic waves reflect at material boundaries that represent dielectric contrasts in the sub-surface. The amplitude and arrival time of reflected waves are recorded and displayed as the GPR trace. Unlike seismic waves, GPR involves the transmission and reflection of electromagnetic instead of elastic waves. The former attenuate rapidly if the subsurface is electrically conductive. The amplitude of the returned waves is much lower than that of the transmitted waves due to spherical spreading of the outgoing signal, attenuation of the propagating wave, and a non-zero transmission coefficient at material boundaries. The low amplitude of signal returns necessitates careful processing to ensure that the returned signal level is higher than the noise level. This study will focus on the application of wavelet filtering and topographic migration to GPR data collected at the Odessa Meteorite Crater. Other than these techniques, a standard data processing workflow (de-wow, background subtraction, and amplitude gain) will be used. For discussion of other commonly-used processing methods see *Cassidy* (2009)

3.2.2 Fourier domain and wavelet filtering

In any GPR trace there will be a wanted signal component and an unwanted signal component. The unwanted signal component may be termed “noise”. The general goal of filtering is to remove the bulk of the noise while altering signal minimally. The transition between signal and noise is largely defined by the individual performing the filtering

(*Cassidy*, 2009). GPR data collected at the Odessa Meteorite Crater has been contaminated by electromagnetic interference from the nearby oilfield activities. This large noise power must be reduced in order to effectively interpret the GPR data.

The Fourier (frequency) domain representation of a transient signal is the set of amplitudes of sine and cosine functions at systematically varying frequencies, that when additively combined would reproduce the transient signal (*Bracewell and Bracewell*, 1986). It is common practice to remove noise from a GPR trace by Fourier domain filtering. Signal power at frequencies that are interpreted to be dominated by noise may be reduced in the Fourier domain via the application of various filters. The resulting GPR trace, reconstructed in the temporal domain, will contain greatly reduced noise power. However, there are several well-known issues with the application of Fourier domain filtering to GPR traces. For example, a transmitted electromagnetic pulse has "broadband" or wide frequency content in the Fourier domain (*Everett*, 2013). If noise occurs within this broad band of frequencies, it is not possible for the noise to be completely removed without somewhat altering the signal. Additionally, Fourier-domain signals contain only frequency and phase information; temporal localization is not retained upon transformation of a transient signal into the Fourier domain (*Boggess and Narcowich*, 2015).

GPR data at the Odessa Meteorite Crater is contaminated by broadband electromagnetic interference within the frequency content of the transmitted GPR pulse. Attempting to remove this noise via Fourier domain filtering could significantly alter the GPR signal, thus a more advanced filtering method is needed for the GPR data at the

Odessa Meteorite Crater. The wavelet transform has similar noise-reduction objectives as the Fourier transform, but involves the approximation of a transient signal by a series of compact, or locally defined wavelets instead of globally-defined trigonometric functions (*Boggess and Narcowich*, 2015). *Mallat* (1989) used wavelets of different time scales to decompose a transient signal into varying levels of detail. The decomposition process enables the visualization of the details of a signal separately at each of the various time-scales. Wavelet decomposition beneficial for GPR filtering because the wavelet transform preserves both frequency and temporal localization, and wavelet shapes can be tailored to analyze different types of transient signals, unlike sine and cosine basis functions.

3.2.3 Kirchoff and Topographic migration

Both seismic and GPR data are generally collected at finite offset, an acquisition protocol in which the transmitter (Tx) and receiver (Rx) are not placed at the same location. The Tx-Rx geometry creates artifacts in the data that would not be present at zero offset. Diffractions, for example, occur when a spatially compact scatterer reflects energy to the Rx from a subsurface location that is not directly beneath the midpoint of the Tx and Rx (Figure 13). Also, dipping reflectors are improperly imaged, both in their location and dip angle, as the ray path with the shortest travel time is not symmetric about the Tx and Rx midpoint as it is in the case of signal returns from a horizontal reflector (Figure 14). Migration can be used to correct these artifacts in both GPR and seismic data, thus removing the effects of acquisition Tx-Rx offset and more accurately representing the actual geometry of sub-surface surface reflectors in the displayed time or depth section (*Yilmaz*, 2001). Commonly-used seismic migration algorithms have been applied to GPR data (*Cassidy*, 2009), while GPR specific algorithms accounting for the exact antennae radiation pattern have been proposed (*Leuschen and Plumb*, 2001; *Streich and Van der Kruk*, 2007). Kirchoff migration is a summation migration technique in which energy distributed along a hyperbola based on the possible travel time between Tx-Rx is summed and the summed energy is shifted, or migrated, upward to the apex of the hyperbola (Figure 15, *left*) (*Yilmaz*, 2001). Kirchoff migration is used in both seismic and GPR data processing workflows because of its simplicity and dependence on travel time equations, therefore it can be adapted for topographic effects.

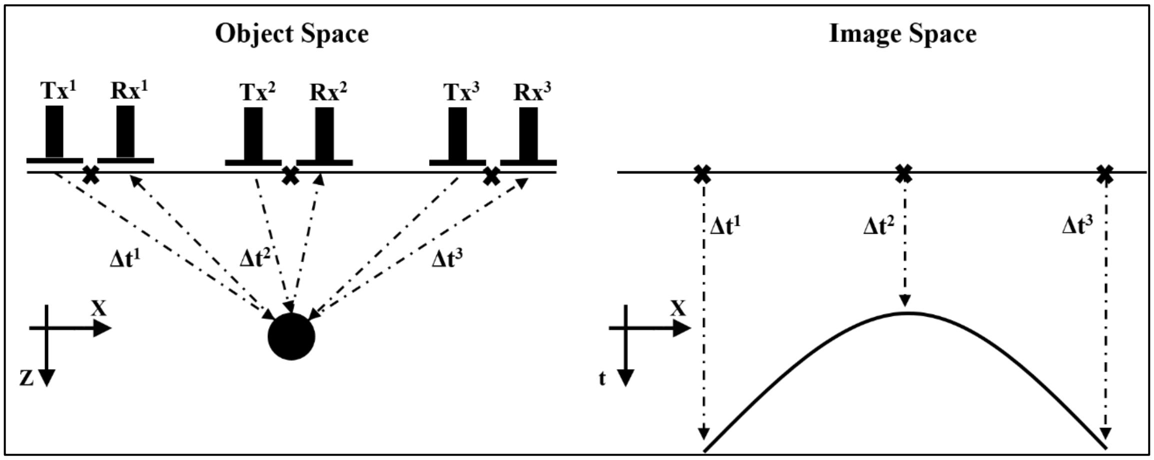

Figure 13 – Example of point scatterer and resulting diffraction. Left - transmitted energy is returned to receiver even though not located directly above the point scatterer. Right – the point scatter appears as a "diffraction hyperbola" in image space as the arrival time of the reflected energy is located directly beneath the measurement location.

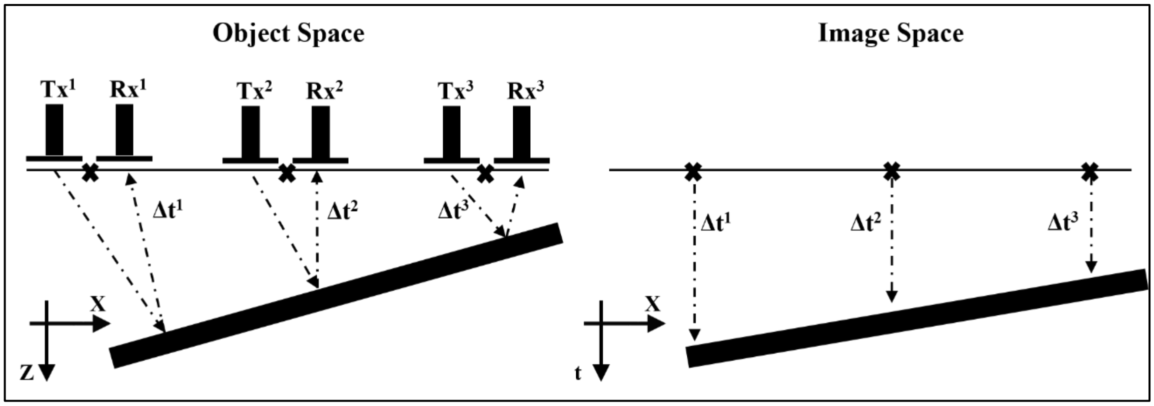

Figure 14 – Example of dipping reflector and improper imaging. Left – Reflections of a dipping surface do not occur directly beneath measurement locations. Right – in image space, the reflected energy is placed directly beneath the measurement location causing dipping reflectors to be improperly imaged in dip and location.

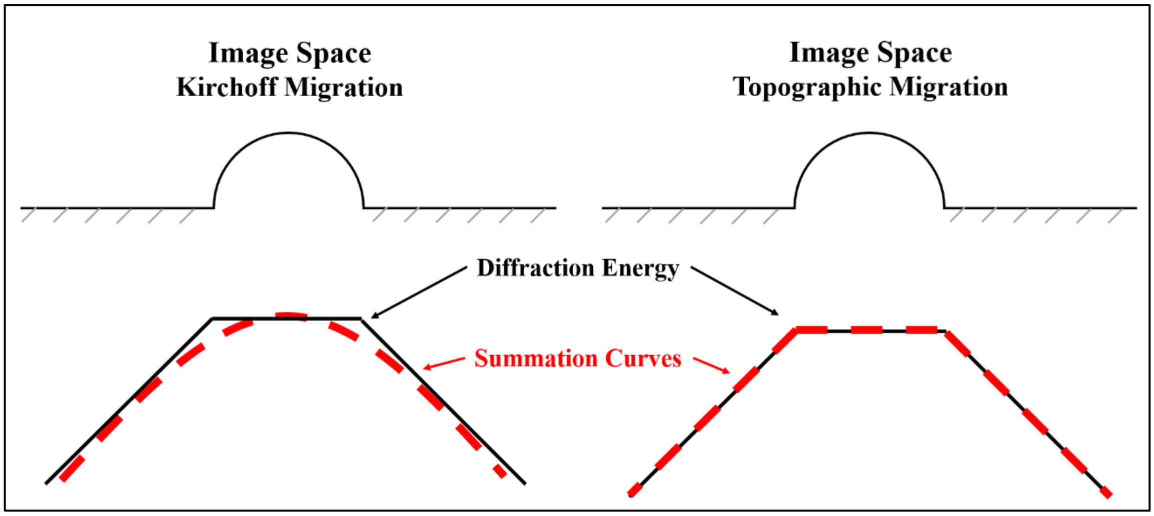

Figure 15 – Example of Kirchoff and topographic migration principles. Left – a point scatter under the topographic surface will create diffraction energy in a trapezoidal shape, while the Kirchoff summation curve is hyperbolic. Right – The topographic summation curve resembles the diffraction energy shape to accurately migrate the data.

Topography is commonly ignored during seismic migration since the magnitude of topographic changes, i.e. the relief, is generally much less than the depth of investigation of seismic methods. Hence, the use of topographic migrations in seismology is limited to mountainous and other areas of rugged terrain (*Wiggins*, 1984). However, the depth of investigation of GPR surveys is much less than that of seismic surveys and is of the same order of magnitude as typical topographic relief, necessitating the use of a topographic migration algorithm (*Lehmann and Green*, 2000). To account for topography, a typical Kirchoff migration algorithm must modified to account for the travel time difference caused by local elevation or depression of the Tx and Rx. In effect, diffracted energy is no longer summed along a hyperbolic curve, but rather a curve that depends on the local terrain variation (Figure 15, *right*). *Dujardin and Bano* (2013) recently showed the effectiveness of using topographic migration over standard migration schemes. The algorithm outlined by *Dujardin and Bano* (2013) has been vectorized for faster processing speeds and this was used to migrate the GPR data acquired at the Odessa Meteorite Crater.

4. DATA ACQUISITION AND PROCESSING

4.1 Geophysical Field Setup at the Odessa Meteorite Crater

Four principal azimuths (lines 1, 7, 10, and 13) were constructed approximately north, east, south, and west (Table 4). Three accessory lines (4, 5, and 6) were constructed in the eastern, non-circular, area of the crater (Table 4). An azimuthal survey grid was constructed at the Odessa Meteorite Crater to facilitate effective and efficient data acquisition. The seven lines at different “azimuths” extend outward from the approximate center of the crater, traversing over the exposed crater rim, and are numbered as shown (Figure 16). The center of the crater and the end of each line has been marked with semi-permanent orange plastic survey spikes. The center point and the line endpoints were referenced to UTM coordinates via GPS (Table 2) to maintain the repeatability of future surveys. Additionally, the center point of the lines was referenced to both the metal fence surrounding the central mineshaft with metric tape measures and to permanent features near the crater with a total station (Figure 17, Table 3).

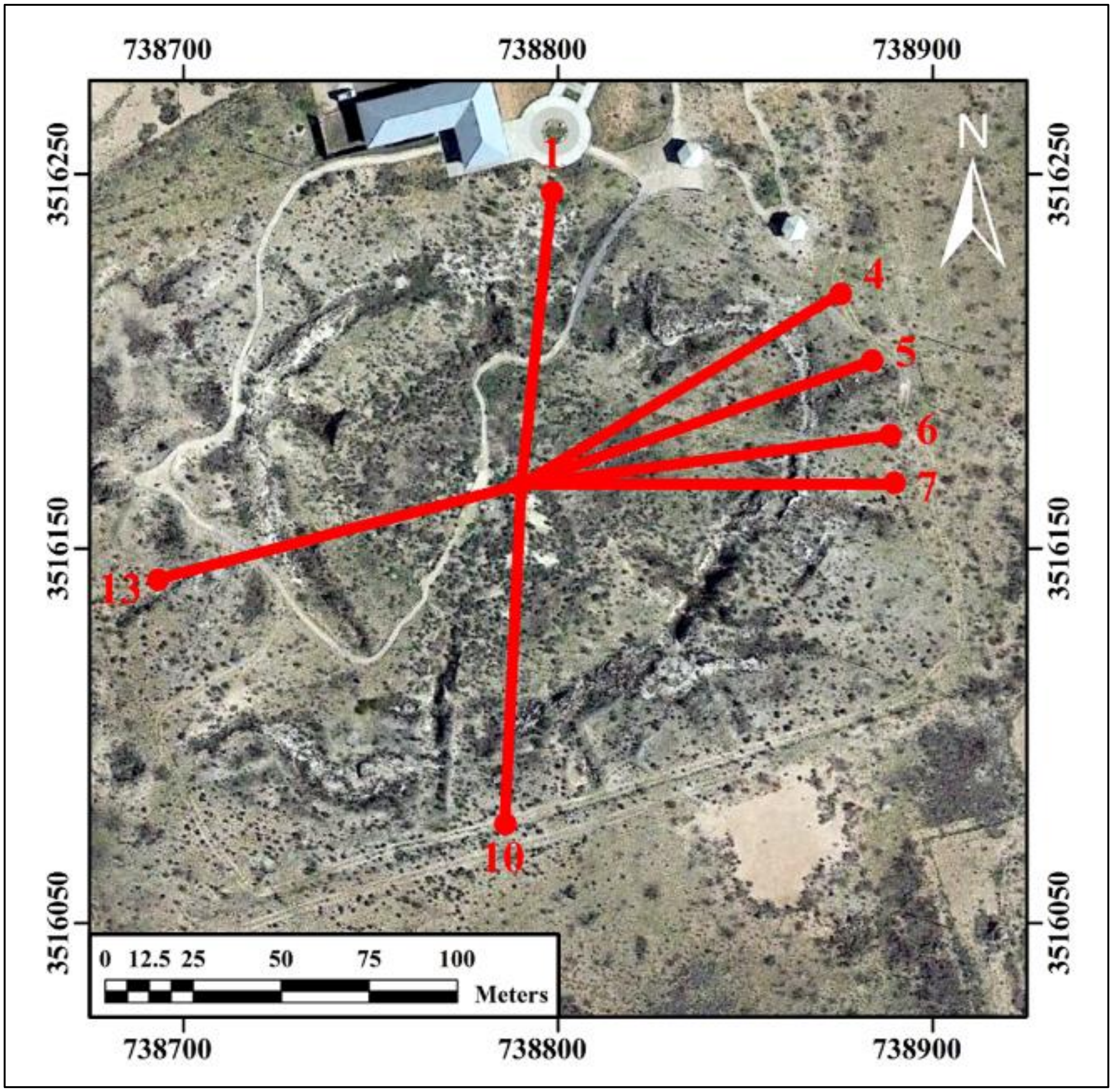

Figure 16 – Locations of survey lines showing the azimuths. Coordinates of center and end points in Table 2. Scale bar in lower left and north arrow in top right. Easting and Northing UTM coordinates from zone 13N.

Table 2 – GPS coordinates of selected azimuth endpoints. UTM coordinates in Zone 13N.

Location	Latitude (N)	Longitude (W)	UTM Easting (m)	UTM Northing (m)
Center	31° 45” 21.928’	102° 28” 44.202’	738789.96	3516166.79
End Az 1	31° 45” 24.458’	102° 28” 43.814’	738798.37	3516245.05
End Az 4	31° 45” 23.522’	102° 28” 40.912’	738875.40	3516217.97
End Az 5	31° 45” 22.939’	102° 28” 40.609’	738883.81	3516200.13
End Az 6	31° 45” 22.291’	102° 28” 40.443’	738888.64	3516180.29
End Az 7	31° 45” 21.874’	102° 28” 40.412’	738889.76	3516167.49
End Az 10	31° 45” 18.997’	102° 28” 44.433’	738785.98	3516076.42
End Az 13	31° 45” 21.182’	102° 28” 47.897’	738693.26	3516141.61

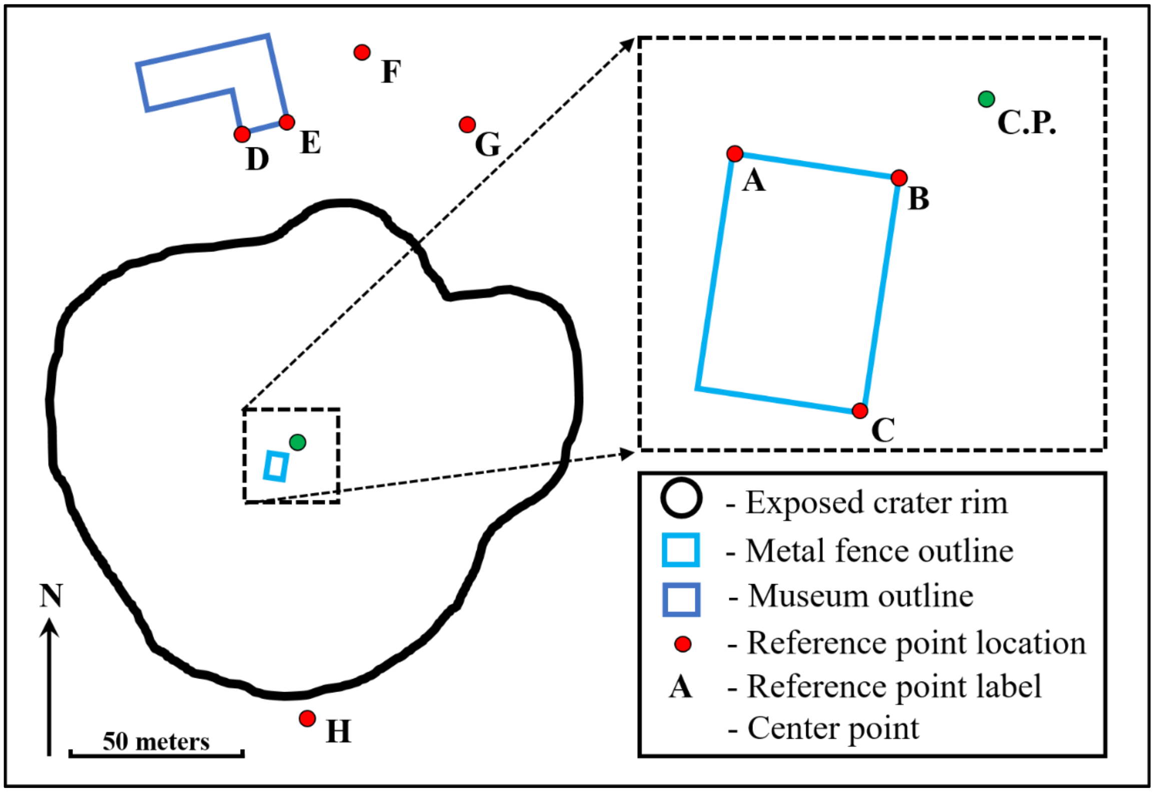

Figure 17 – Center point reference schematic. Red dots show approximate location of center point references. Distances from center point to reference location in Table 3.

Table 3 – Center point reference measurements. Location of points shown in Figure 17.

Point	Description	Distance to Center Point (m)	Method
A	North-west corner of metal fence	10.00	Metric tape measure
B	North-east corner of metal fence	7.00	Metric tape measure
C	South-east corner of metal fence	12.60	Metric tape measure
D	West corner of museum patio	83.77	Total Station
E	East corner of museum patio	85.52	Total Station
F	Flag pole closet to crater	105.59	Total Station
G	Center of north gazebo	97.54	Total Station
H	Power pole near south fence	79.31	Total Station

Table 4 – Azimuth line length, heading, and direction summaries.

Line	Length (m)	Approximate Heading (° from N)	Approx. Location of Rim Crest (m)
1	83	5.8	73
4	100	59.1	86
5	100	70.4	86
6	100	82.2	83
7	100	89.1	79
10	90	181.9	82
13	100	254.9	87

4.2 Topography of the Odessa Meteorite Crater

Topographic data were collected with a total station at Odessa Meteorite Crater to assist with corrections to the near-surface geophysical datasets and to visualize the large-scale irregular terrain of the crater. Large-scale terrain variations of meteorite craters is fundamentally important to understanding the impactor characteristics (i.e. size, velocity, and impact angle) as well as how the crater's morphology has evolved through time. A portion of the topographic data were collected at a fine scale (1 m spacing) along each of the 7 lines to enable topographic correction of both ERT and GPR data. Coarser topographic measurements with ~5-10 m irregular spacing were made throughout the crater and surrounding area. These coarser spaced data were interpolated onto a regular grid, providing a general representation of the crater's topography (Figure 18). While the coarse topographic data show the large-scale heterogeneity of the crater, the large and irregular spacing of measurements and the lack of measurements in certain areas (within trenches and along vertical slopes) induces errors and does not capture the true topographic state of the crater. Additional surveying with more time-effective methods (i.e. LIDAR or photogrammetry) should be used to more accurately analyze the detailed topography of the entire crater.

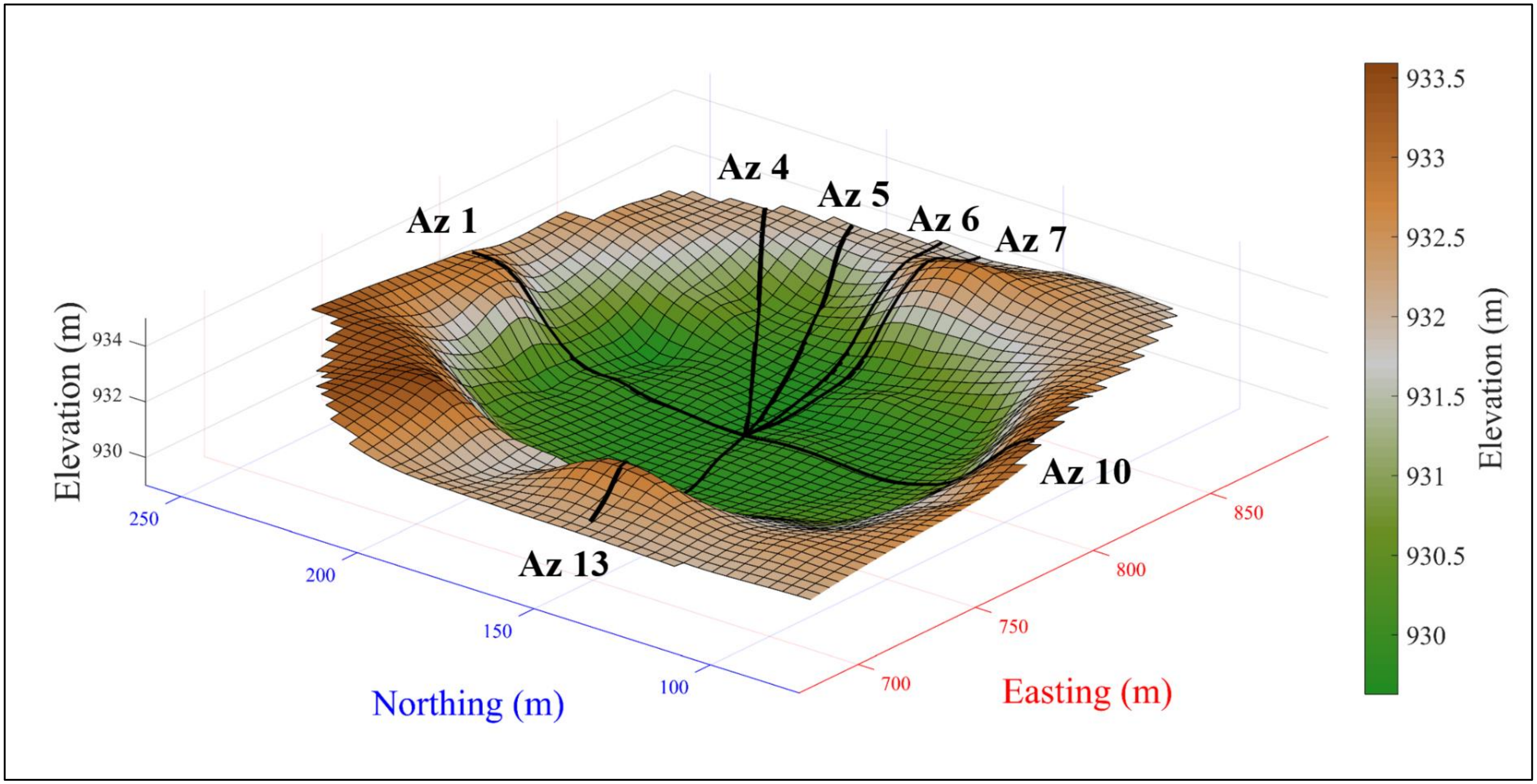

Figure 18 – 3D representation of crater topography. Survey lines shown by black lines, color bar to right, view from south west of crater. Local northing and easting referenced from UTM zone 13N 738000E and 3516000N

4.3 ERT

4.3.1 ERT data acquisition

ERT data were collected with the AGI R8/IP SuperSting earth resistivity meter with 112 electrodes. A total of seven ERT lines were collected in dipole-dipole acquisition mode (*Everett*, 2013). One ERT transect was collected on line 1 with 0.75 m electrode spacing, four ERT transects were collected on azimuth lines 4, 5, 6, and 7 with 1 m electrode spacing, and two other ERT transects were collected across multiple azimuth lines, 1-10 and 6-13 with 1.5 and 1.75 m electrode spacing, respectively. The single line transects, that began in the center of the crater and extended along a line across the rim, aimed to image the crater rim and any associated features in detail. The multiple line transects, that extended from rim to rim across the center of the crater, aimed to image the entirety of the crater width and depth. While electrodes within the crater easily established electrical contact with the soft sediment of the subsurface, electrodes on the exposed limestone rim did not easily establish electrical contact. Poor electrical contact led to large contact resistance between electrode pairs, low injected current and received voltage, and higher noise levels in the data.

4.3.2 ERT data processing and inversion

In conditions that that reduce the current injection ability of the ERT system, like poor electrical contact, measured apparent resistivity values must be "conditioned" before the inversion process. Thresholds for "data quality" values (minimum voltage, max repeat error, minimum apparent resistivity, and max apparent resistivity) are set and the outlying measured apparent resistivity values are discarded (Table 5). Inversions run on unconditioned data can depended heavily on the noise, have large misfit values, and do not necessarily reveal the underlying geologic features (Figure 19, *top*). Inversions run with thresholding typically produce results that better fit the measured data and reveal geologic features more realistically (Figure 19, *middle*). Additionally, data points with high misfit between the measured and calculated apparent resistivity should be removed after an initial inversion to further improve results (Figure 19, *bottom*) by removing unrealistic resistivity distributions dictated by only a few data points, such as the anomalous (3000+ Ohm-m) resistivity zone on the far left of Figure 19 . A histogram of misfits is used to identify a cut off misfit percentage, above which data are removed for refined inversions (Figure 20).

The inversion of ERT data begins with a starting subsurface resistivity model that is updated iteratively aiming to reduce misfit and accurately represent the subsurface. The average apparent resistivity, i.e. the average of all apparent resistivity values, of a dataset is often used as the starting model. Because the starting model is homogeneous, the resulting inversion often has large-scale (> 10 m), smooth features that do not reveal significant smaller scale (< 10 m) geologic structure that may be present (Figure 21, *top*). Using a-priori knowledge from the Evan's geologic study that the crater contained exposed limestone rim and substantial ejecta deposits at the base, the apparent resistivity pseudosection was determined to be a more appropriate as a starting model. This starting model resembles subsurface geologic variability more accurately than the average resistivity and inversion results based on the pseudosection resolve smaller, more heterogeneous, geologic features (Figure 21, *bottom*). Smooth (Figure 22, *top*), robust

(Figure 22, *middle*), and damped least squares (Figure 22, *bottom*) inversion methods as described earlier were tested and all led to similar results. While each resulting model exhibits slight differences, they are essentially the same in the sense that they would lead to the same geologic interpretation. All ERT data were conditioned with the same thresholds (Table 5), all data with misfits greater than 60% were removed, and only smooth model inversions are henceforth considered.

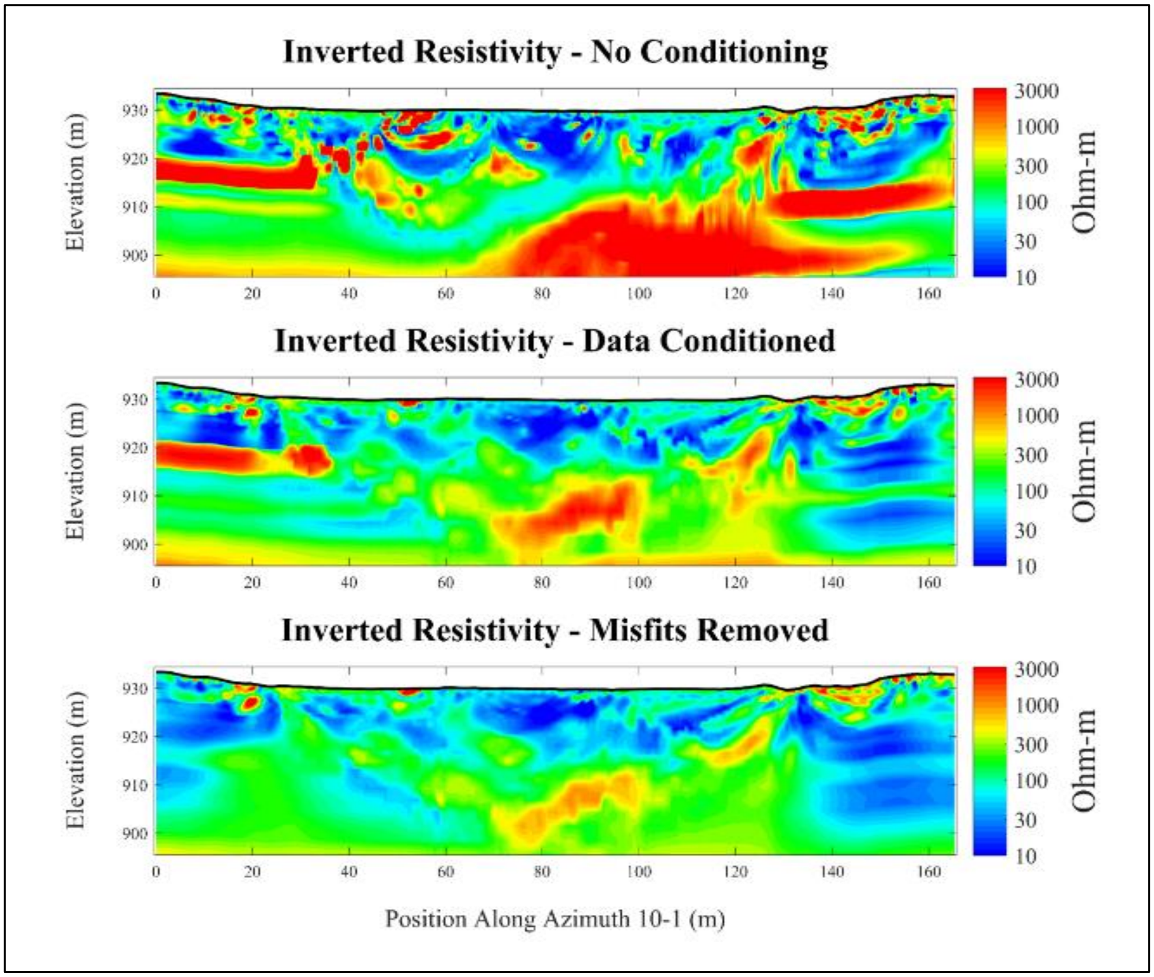

Figure 19 – Effect of ERT data processing on inversion results. Top – inversion results with no data removed. Middle – inversion results with data thresholds applied. Bottom – inversion results with misfit greater than 60% removed. ERT azimuth line 10-1 used for example purposes.

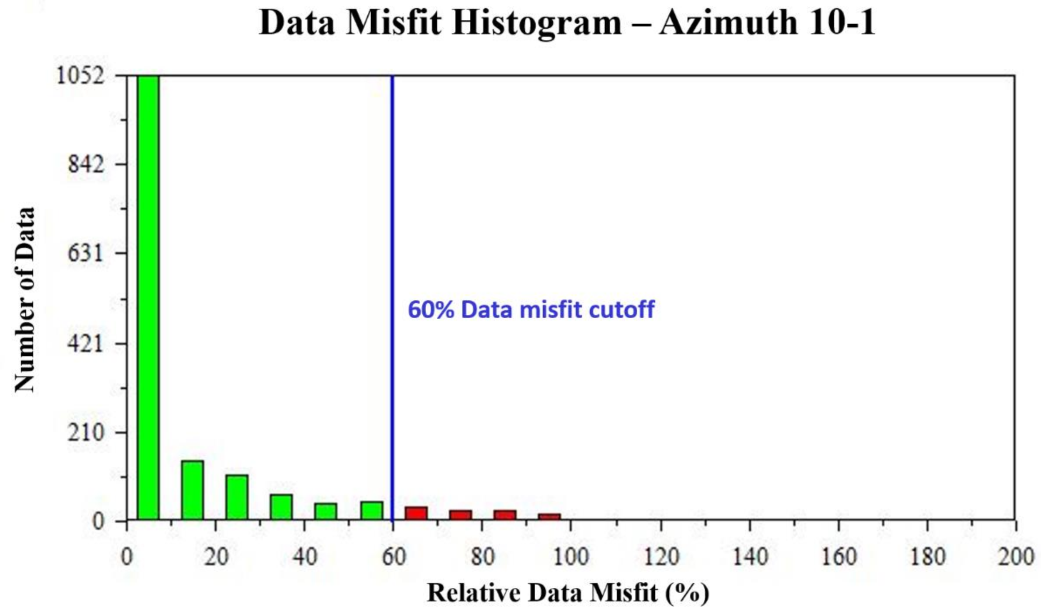

Figure 20 – Example misfit histogram. X-axis: percentage of relative misfit from the calculated and measured pseudosection. Y-axis: number of data at % of misfit. Blue line indicating 60% misfit cutoff.

Table 5 - Thresholding properties of ERT data conditioning. Note that a data point can violate multiple thresholds.

Condition	**Threshold**	**Number of Data Points Removed**	**Percentage of Total**
Minimum Voltage	0.05 mV	56	2.7 %
Max Repeat Error	5 %	32	1.5 %
Minimum Apparent Resistivity	.01 Ohm*m	212	10.2 %
Maximum Apparent Resistivity	10000 Ohm*m	39	1.9 %
Apparent Resistivity Spike	N/A	417	20.1 %
Total	N/A	503	24.3 %

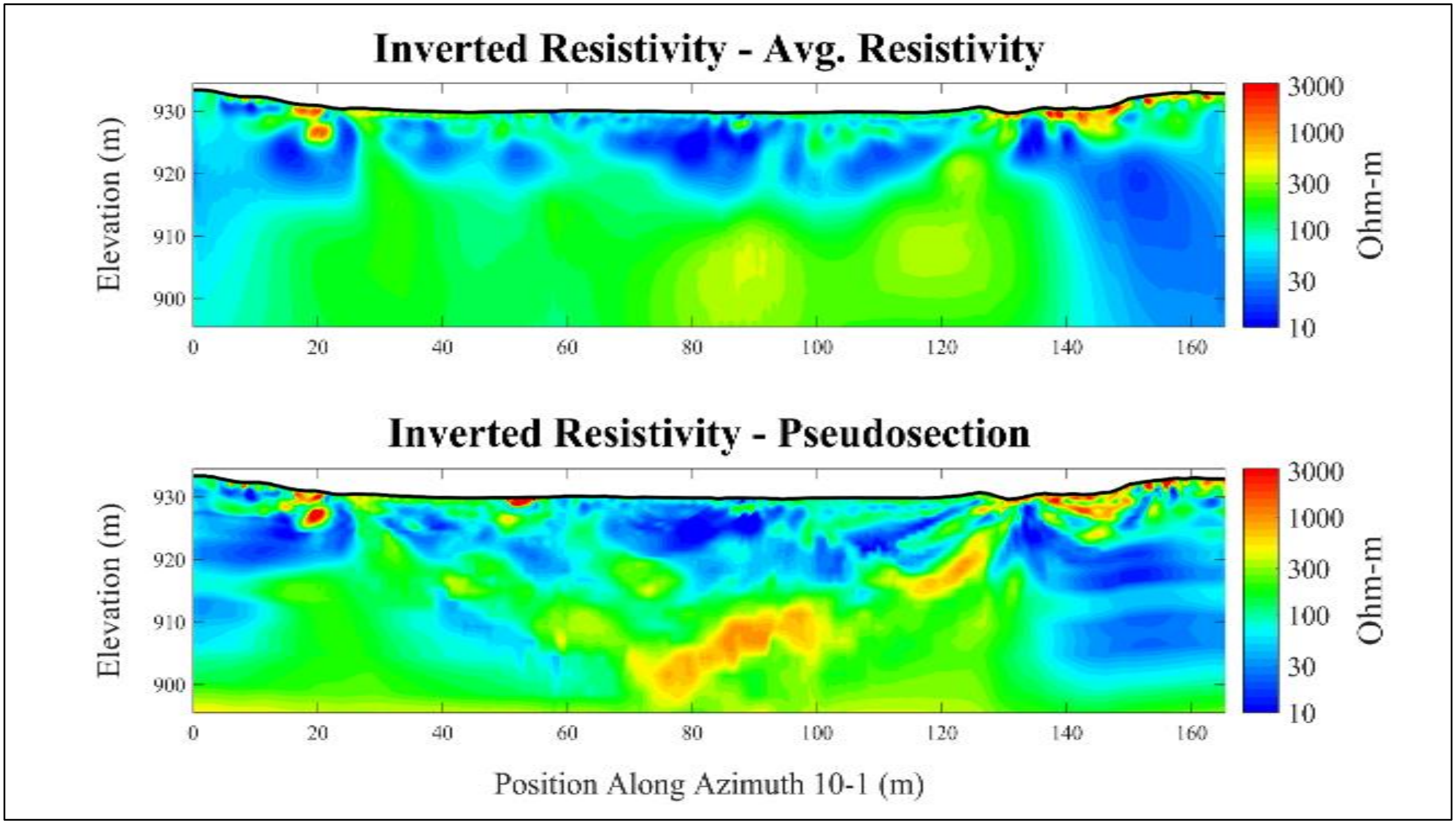

Figure 21 – Effect of starting model on inversion results. Top – inversion results with average apparent resistivity starting model. Bottom – inversion results with Pseudosection starting model. ERT azimuth line 10-1 used for example purposes.

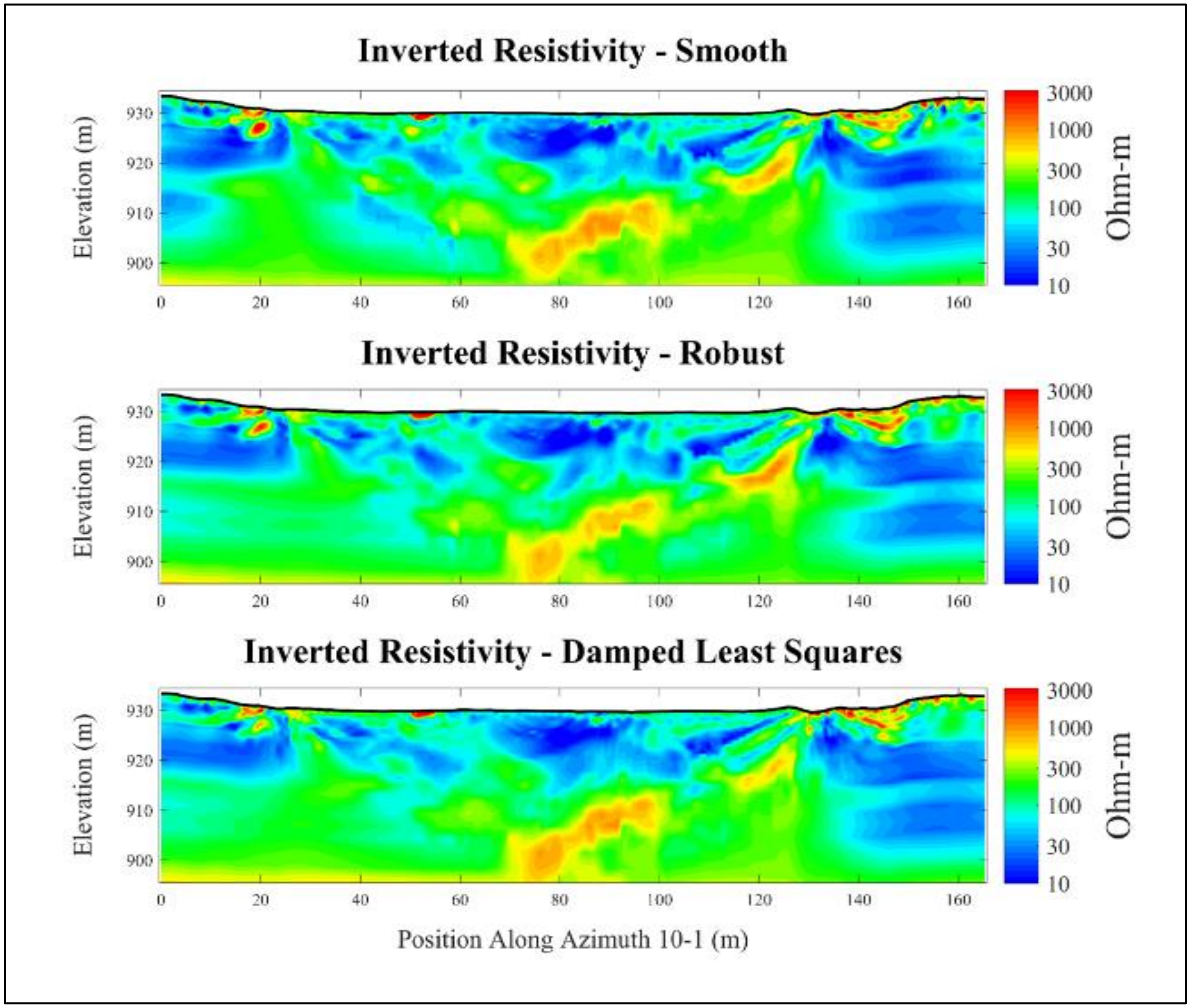

Figure 22 – Effect of inversion method on results. Top – inversion results with smooth method. Middle – inversion results with robust method. Bottom – inversion results with damped least squares method. ERT azimuth line 10-1 used for example purposes.

4.4 GPR

4.4.1 GPR data acquisition

GPR data were collected with the Sensors and Software pulseEKKO PRO system at frequencies of 100, 200, and 500 MHz. GPR has depth of investigation on the scale of several meters as opposed to ~25 meters for the ERT system, therefore the GPR data were collected with the intention of investigating fracture density in the exposed and shallow-buried unexposed rim. The GPR data were collected at 200 and 500 MHz frequencies on portions of azimuth lines 4, 5, 6, and 7 using a station spacing of 0.1 m to resolve features on that order of magnitude. Because the interior of the crater is covered by large accumulations of sediment that buried interesting features beneath the maximum depth of investigation, GPR data were collected only along portions of these lines near the exposed crater rim. GPR data were collected at 100 MHz frequency along the entirety of azimuth lines 1, 4, 5, 6, 7, 10, and 13 with station spacing of 0.2 m because the 100 MHz frequency is unable to resolve features smaller than 0.2 m. The 100-MHz GPR data shows evidence of a larger signal to noise ratio (i.e. the ratio of the maximum signal amplitude to the maximum amplitude of noise beneath signal penetration) than either the 500- or 200-MHz GPR lines (Figure 23). The increased noise levels are hypothesized to be caused by equipment issues (poor data transmission on fiber optic cables, weak signal generation by the transmitter) or infrastructure associated with pumpjacks near the crater (Figure 24) that was installed between collection of the 200/500 MHz data (1/1/2016) and the 100 MHz GPR data (10/22/2016).

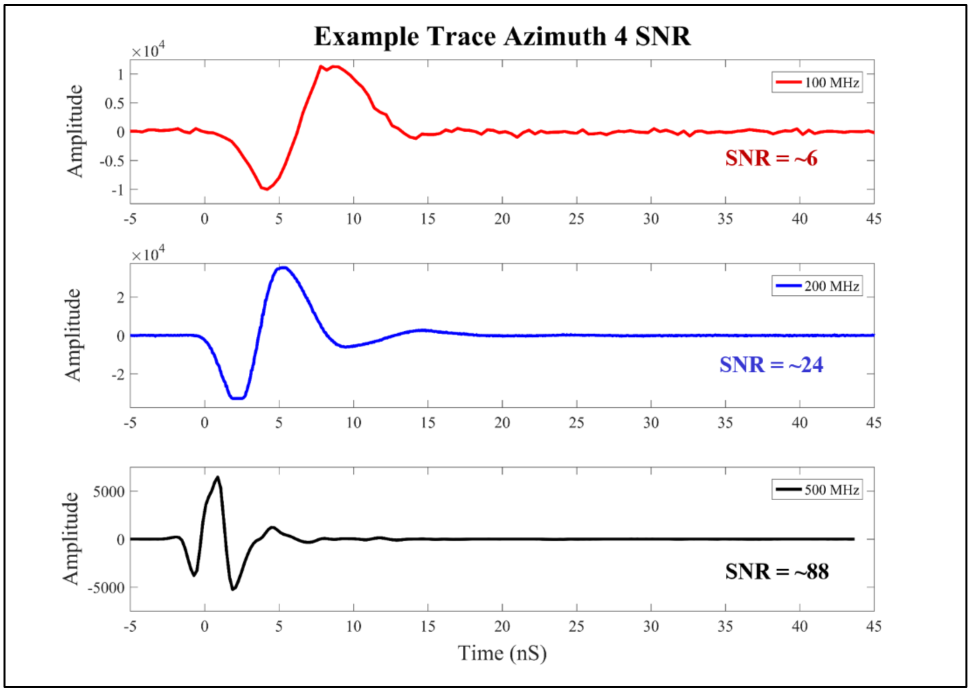

Figure 23 – Approximate signal to noise ratios of the three GPR frequencies. Top – 100 MHz, middle – 200 MHz, bottom – 500 MHz. Larger signal to noise ratios are better than low ratios. 100 MHz data approximately an order of magnitude lower than either the 500 or 200 MHz data. Signal to noise ratio approximated by the ratio of the maximum amplitude of the signal (early time) and the maximum amplitude of the noise (late time).

Figure 24 – Infrastructure near crater. A – Pumpjack infrastructure located approximately 100 yards from the crater. B – Communications antennae approximately 2 miles from the crater.

4.4.2 GPR data processing

Data from all lines and frequencies were processed with a de-wow and background subtraction filter to remove “wow” and the “ground clutter” that are characteristics of the Tx and Rx, and not indicative of subsurface geologic structure. “Wow” in a GPR trace is the tendency of a recorded signal to deviate from zero-mean as time progresses. The “ground clutter” is the large-amplitude wave that is transmitted directly from the Tx to Rx on the ground surface. These filter make data more easily interpretable than the unfiltered data (Figure 25). The average frequency spectra shows that the 100-MHz data (Figure 26, *A*) contains large-amplitude noise throughout the spectrum. Evaluating the spectrum at later arrival times, at which signal has attenuated completely, shows that the noise is still present (Figure 26, *B*) indicating that noise is generated by the environment. In the 200 (Figure 26, *C and D*) and 500 (Figure 26, *E and F*) MHz data, the amplitude of the noise is reduced at these times indicating that the noise is a characteristic of the transmitted signal.

As discussed earlier, the broadband noise present in the 100 MHz data is possibly the product of faulty equipment, or communications antennae associated with pumpjacks in the vicinity and is effectively reduced with wavelet filtering as opposed to Fourier filtering. Using a bandpass Fourier filter on the 100 MHz (Figure 27, *C and D*) data does not completely suppress the noise content that is present within the known transmitted signal bandwidth. Using a wavelet filter (Figure 27, *E and F*) removes the noise content present in the signal bandwidth more effectively. Comparing the effect of the Fourier and wavelet filter on a time section of azimuth line 4 (Figure 28), the noise that is not removed with the Fourier filter (Figure 28, *A*) results in large artifacts during migration of the data (Figure 28, *B*). The wavelet filter removes more of the broadband noise (Figure 28, *C*) and artifacts in the migration are minimized (Figure 28, *D*). While the wavelet filter does not completely remove all of the broadband noise and associated migration artifacts, the final migrated results are more interpretable because of the additional noise reduction capabilities of the wavelet filter. The 200 and 500 MHz data were processed with de-wow, background, bandpass Fourier filter and were then topographically migrated and gained with an automatic gain control function. The 100 MHz data were processed with de-wow, background subtraction, and wavelet filtered and were then topographically migrated and gained with an automatic gain control function.

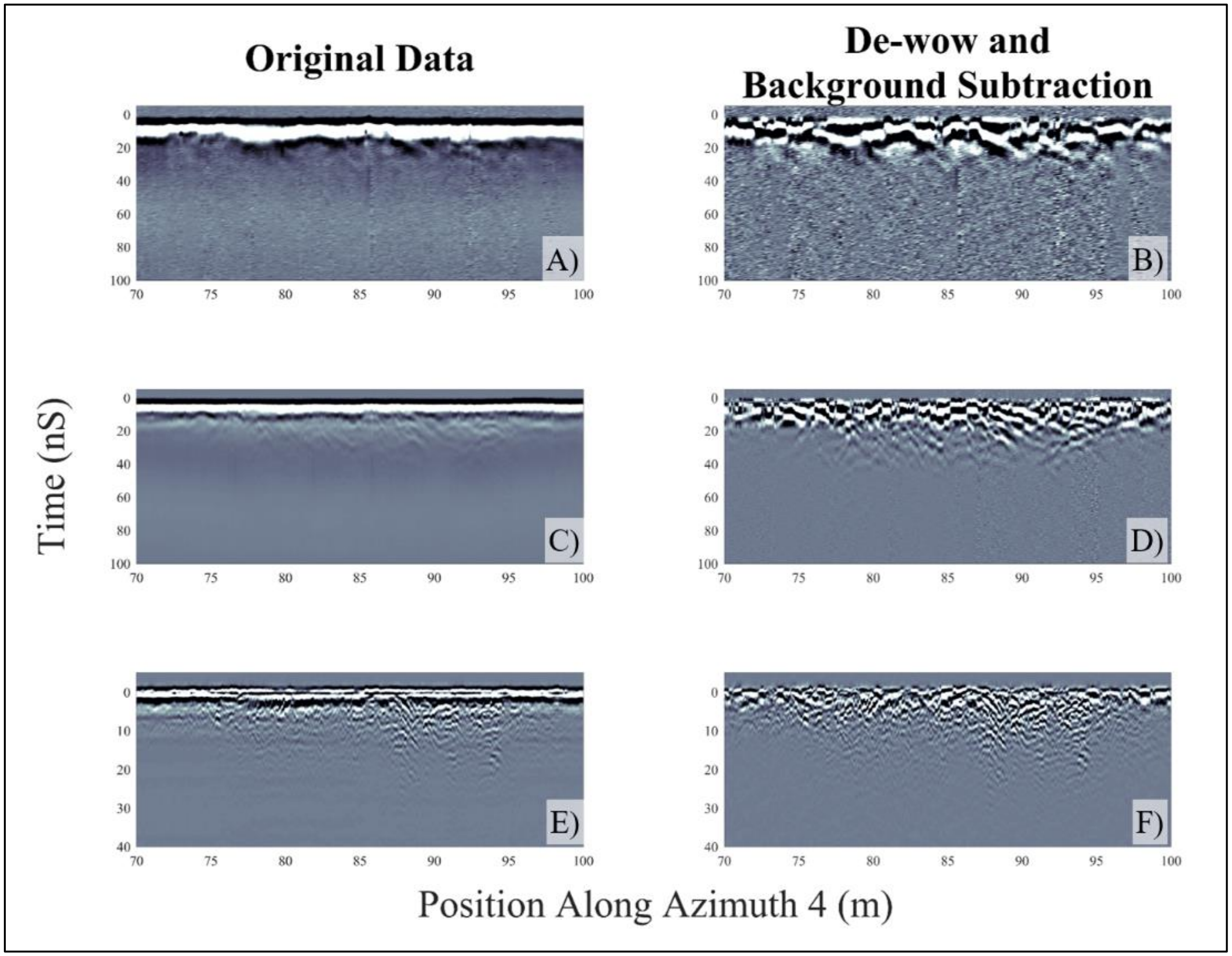

Figure 25 – Example of de-wow and background subtraction filters. X-axis – position along azimuth line 4, Y-axis – time in nanoseconds, and color scales scaled by two standard deviations of each data set. A – Original 100 MHz data, B – filtered 100 MHz data, C – Original 200 MHz data, D – filtered 200 MHz data, E – Original 500 MHz data, F – filtered 500 MHz data.

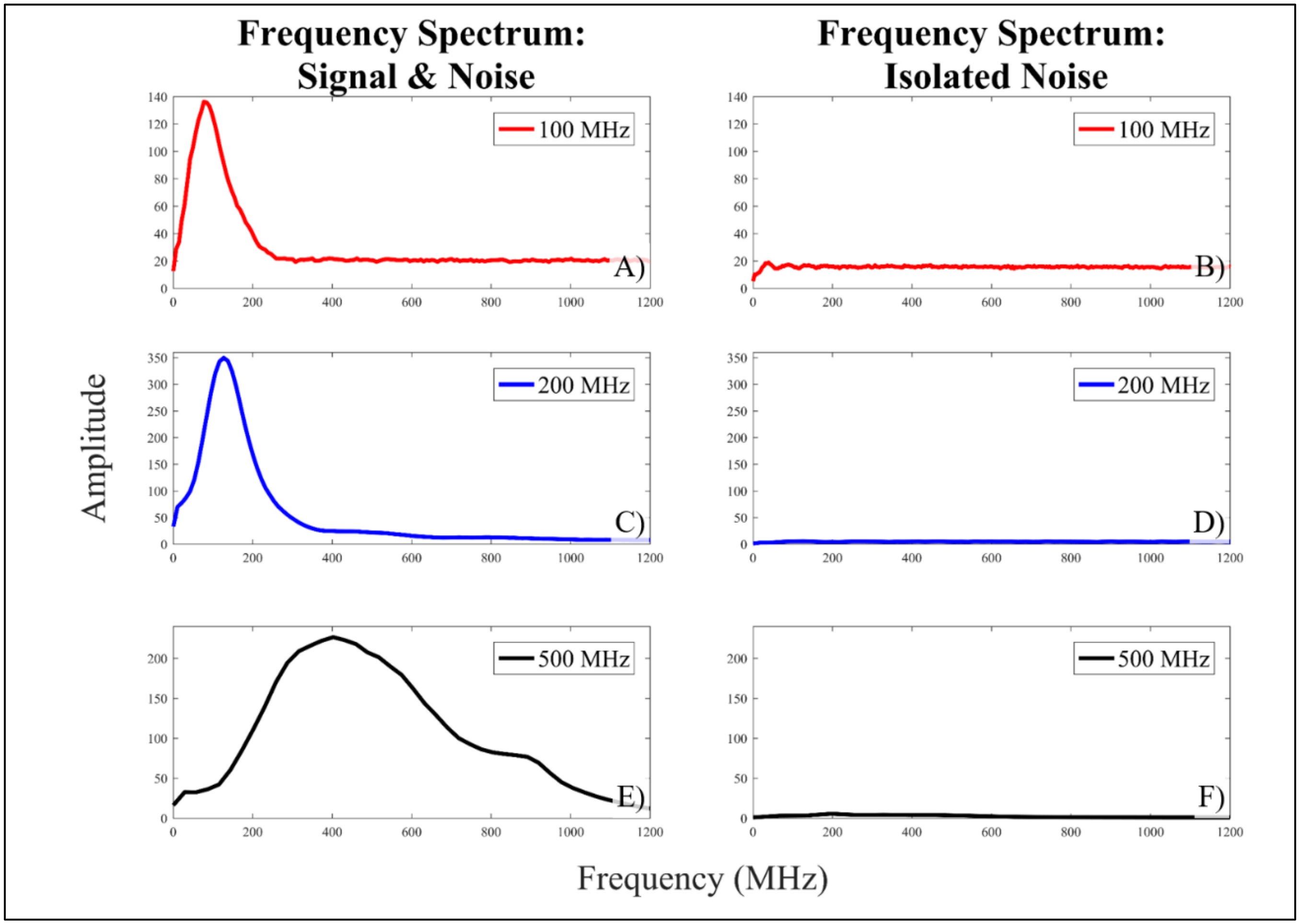

Figure 26 – Average frequency spectrum of 100, 200, and 500 MHz data. X-axis – Average frequency spectrum of azimuth line 4, Y-axis – relative amplitude of spectrum. A – Signal and noise spectrum of 100 MHz data, B – isolated noise spectrum of 100 MHz data, C – signal and noise spectrum of 200 MHz data, D – isolated noise spectrum of 200 MHz data, E – signal and noise spectrum of 500 MHz data, F – isolated noise spectrum of 500 MHz data. Noise spectra defined as the frequency content of late arrival times, at which all transmitted signals would have attenuated.

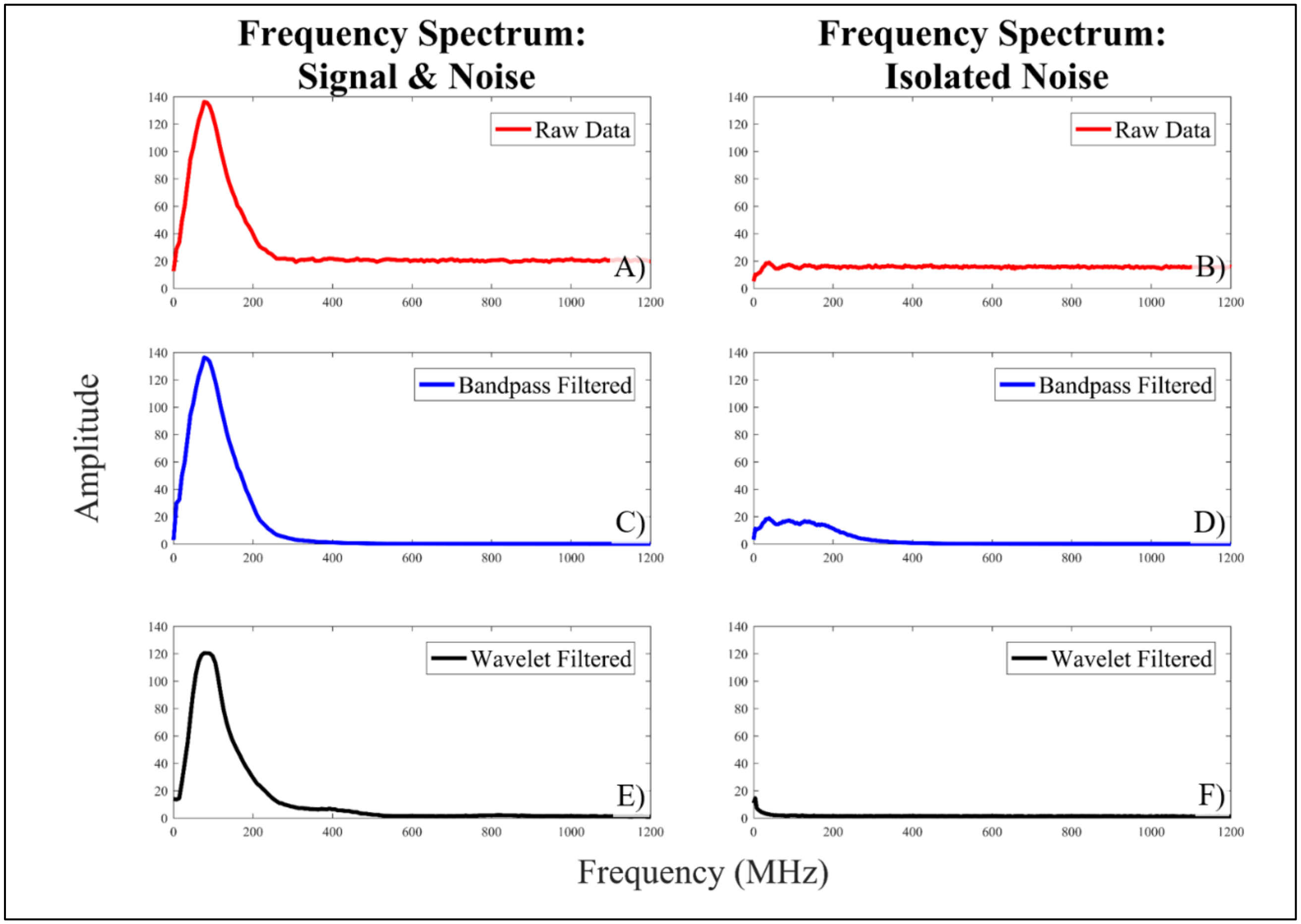

Figure 27 – comparison of the Fourier bandpass filter and wavelet filtering. X-axis – Average frequency spectrum of azimuth line 4, Y-axis – relative amplitude of spectrum. A – Signal and noise spectrum of 100 MHz raw data, B – isolated noise spectrum of 100 MHz raw data, C – signal and noise spectrum of 100 MHz Fourier filtered data, D – isolated noise spectrum of 100 MHz Fourier filtered data, E – signal and noise spectrum of 100 MHz wavelet filtered data, F – isolated noise spectrum of 100 MHz wavelet filtered data. Noise spectra defined as the frequency content of late arrival times, at which all transmitted signals would have attenuated.

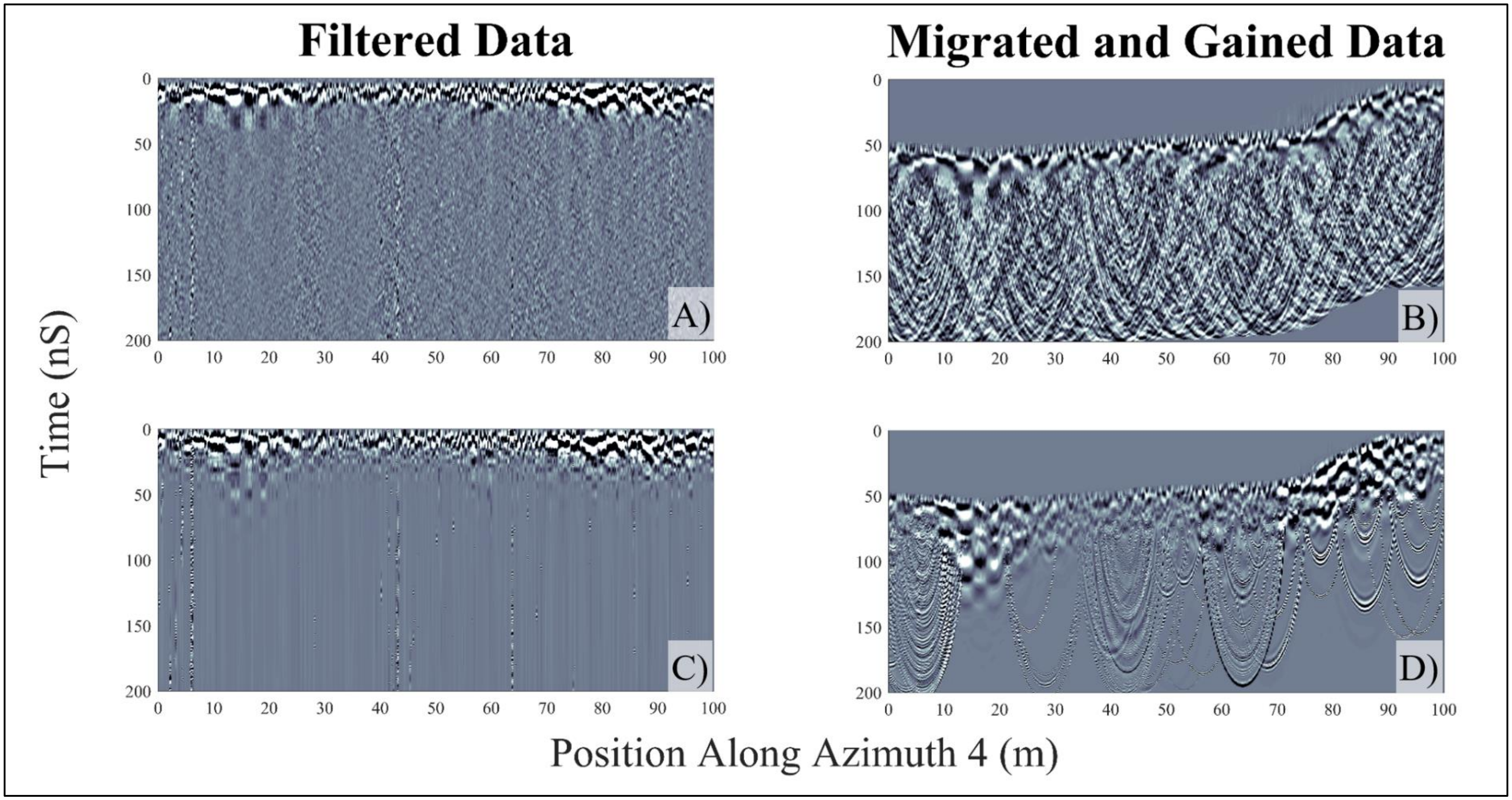

Figure 28 – Comparison of the Fourier bandpass filter and wavelet filtering in time section. X-axis – position along azimuth line 4 in meters, Y-axis – time in nanoseconds. A – Fourier filtered data, B – migration or Fourier filtered data, C – wavelet filtered data, D – migration of wavelet filtered data.

5. GEOPHYSICAL RESULTS

5.1 Topographic Results

The topographic data of the principal azimuth lines (1, 7, 10, and 13) differs greatly from the 3 accessory azimuth lines (4, 5, and 6). Typical topography of an impact crater traversing from the center outward can be summarized as follows: a gentle to moderate slope from the center of the crater towards the rim, a steep slope near the crater rim, a distinct crest of the uplifted rim, and a down-slope continuing past the crater rim (*Melosh*, 1989). Azimuth lines 7 and 13 both follow this pattern well (Figure 29) even though the distance from the center of the rim crest, and total topographic relief differ between the two. Azimuths lines 4 and 5 do not follow this pattern (Figure 29) well. The rim crest and associated down-slope are absent and a general leveling off at the elevation of the surrounding plain is observed. The topographic data of the azimuthal survey lines suggest that either the uplifted crater rim has been eroded away or was not formed as expected in the eastern area of the Odessa Meteorite Crater.

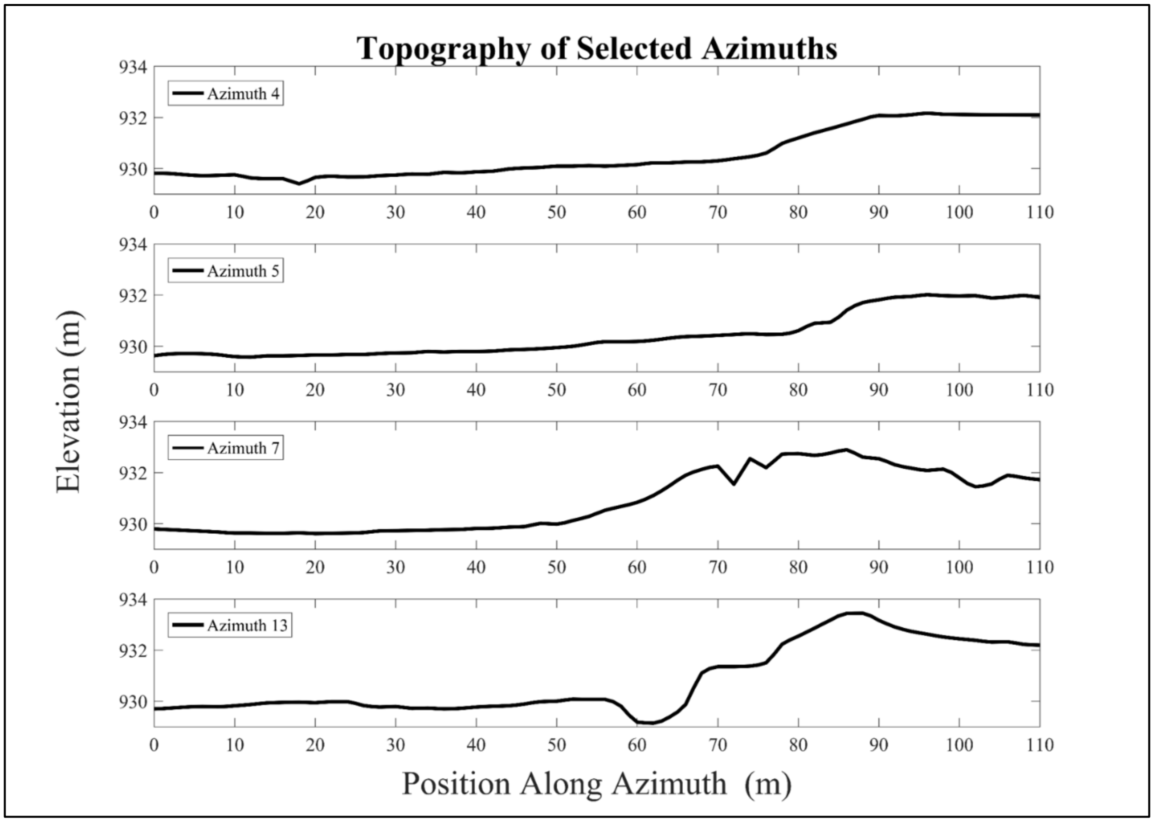

Figure 29 – Topography of selected Azimuths. X-axis in position along azimuth in meters. Y-axis in elevation in meters. Rim crest absent on azimuth lines 4 and 5. Rimes crest located at ~80 and ~90 m on azimuth lines 7 and 13 respectively.

5.2 GPR Results

GPR data from azimuth line 4 at 100, 200, and 500 MHz (Figure 30) shows three characteristic zones of reflectors. The first (outlined in green), is comprised of horizontal to sub-horizontal reflectors that are continuous in the 200 and 500 MHz data. This is interpreted as the crater fill. In the 100 MHz data, this zone is characterized by discontinuous but low amplitude reflectors caused by the lack of contrasts that can be imaged by the lower resolution of the 100 MHz signal. The second zone (outlined in yellow), is comprised of steeper dipping discontinuous reflectors interpreted as the fractured limestone rim. While some reflectors in this zone can be traced for several meters and may represent intact strata of limestone, the majority of the reflectors are not laterally continuous. The third zone (outlined in red), is comprised of reflectors that dip away from the rim at moderate angles and have moderate continuity. This zone is interpreted to be the ejecta blanket formed by sediment that was deposited after crater formation. In the 100 MHz data, there is a moderate loss in amplitude with distance from the limestone rim. Azimuth line 5 (Figure 31) and azimuth line 6 (Figure 32) both show similar results as azimuth line 4 (Figure 30). The crater fill zone (green) corresponds to the flat topography expected within the crater, the fractured limestone rim zone (yellow) is located on the rim slope, and the ejecta blanket zone (red) is present where the topography levels out on top of the crater. Azimuth line 7 (Figure 33) shows some slight differences from azimuth lines 4, 5, and 6. On azimuth line 7, the crater fill zone, characterized by horizontal continuous reflectors, continues up the slope or the rim and transitions to the limestone rim zone (yellow) approximately halfway up the slope. Additionally, the limestone rime zone appears to be less fractured than it does on the other azimuth lines.

Three distinct zones were identified in the GPR data: a zone of continuous reflectors interpreted as the crater fill, a zone of extremely discontinuous reflectors interpreted as the fractured limestone rim, and a zone of shallow dipping reflectors interpreted as the ejecta blanket. Azimuth line 7 appears to have significantly less fractures than azimuth lines 4, 5, and 6 on the rim slope. The exposed limestone rim on azimuth line 7 is also closer to the center of the crater and has greater topographic relief than the rims of azimuth lines 4, 5, and 6 as discussed earlier. These results suggest that the high amount of fractures on azimuth lines 4, 5, and 6 could have increased erosional rates in the eastern portion of the crater. However, additional surveying with high resolution GPR frequencies (i.e. 200 and 500 MHz) is needed in other areas of the crater to confirm that only the eastern portion of the crater rim is highly fractured. Micro-topographic measurement, with less than 10 cm spacing should be made on such lines to improve the accuracy of topographic migration for future studies.

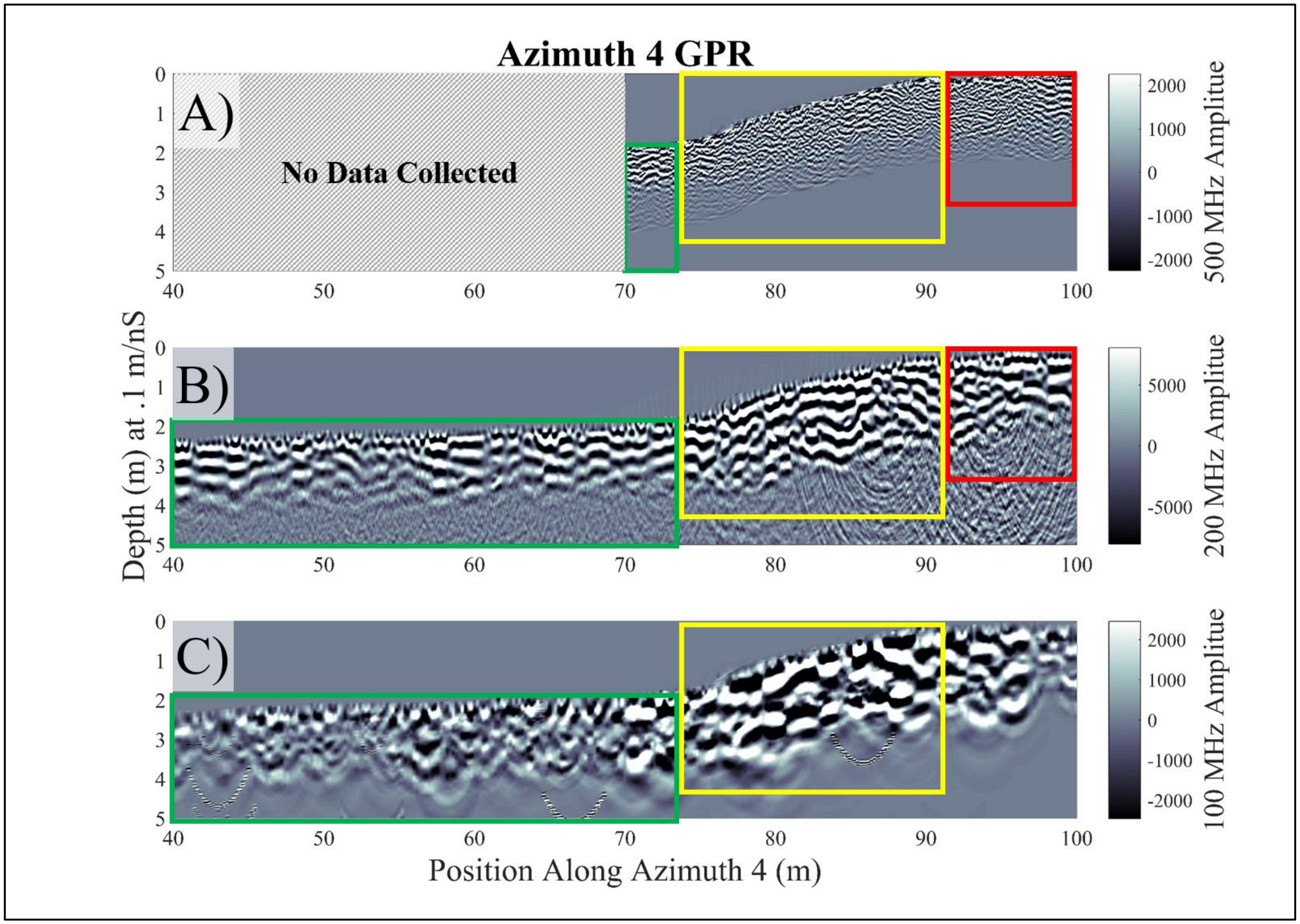

Figure 30 – GPR azimuth line 4. A – 500 MHz GPR data, B – 200 MHz GPR data, C – 100 MHZ GPR data. Color bars on right scaled within two standard deviations of the mean of each dataset. X-axis as position along azimuth line 4 in meters. Y-axis as depth below highest elevation on line in meters. Red box outlining reflectors dipping away from crater. Yellow box outlining high fractured reflectors. Green box outlining approximately horizontal reflectors. For location of azimuth line 4 see Figure 16.

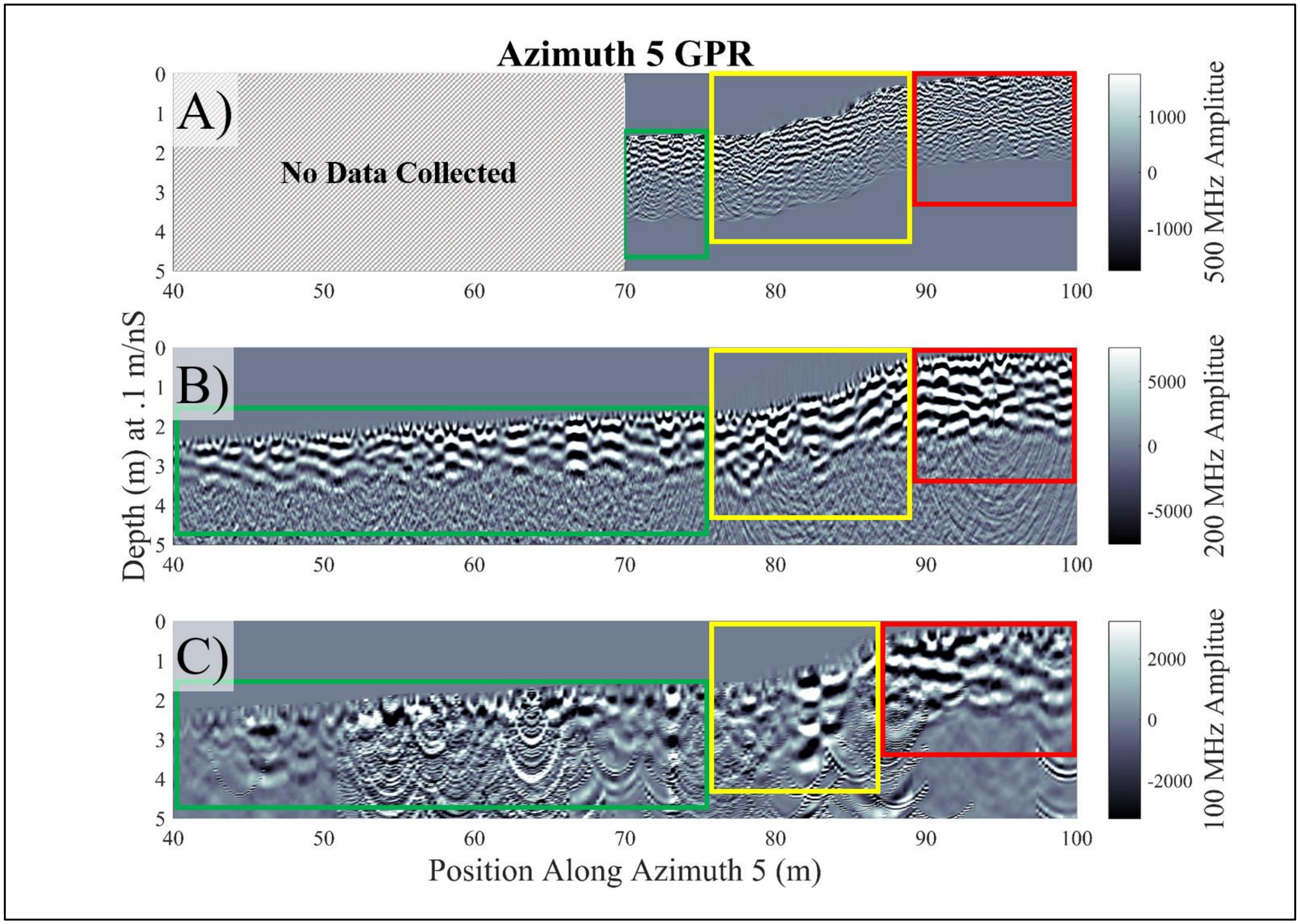

Figure 31 – GPR azimuth line 5. A – 500 MHz GPR data, B – 200 MHz GPR data, C – 100 MHZ GPR data. Color bars on right scaled within two standard deviations of the mean of each dataset. X-axis as position along azimuth line 5 in meters. Y-axis as depth below highest elevation on line in meters. Red box outlining reflectors dipping away from crater. Yellow box outlining high fractured reflectors. Green box outlining approximately horizontal reflectors. For location of azimuth line 5 see Figure 16.

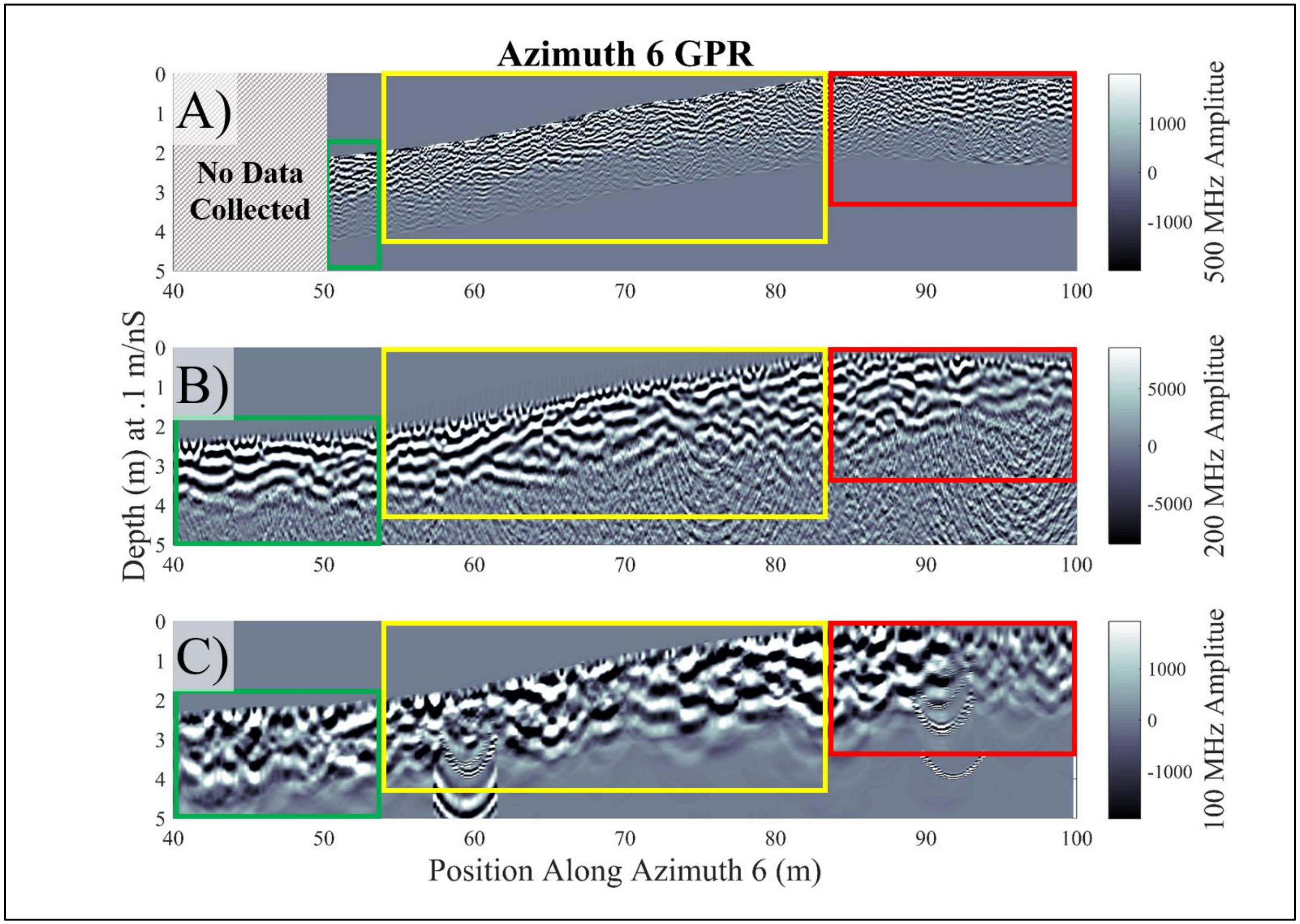

Figure 32 – GPR azimuth line 6. A – 500 MHz GPR data, B – 200 MHz GPR data, C – 100 MHZ GPR data. Color bars on right scaled within two standard deviations of the mean of each dataset. X-axis as position along azimuth line 6 in meters. Y-axis as depth below highest elevation on line in meters. Red box outlining reflectors dipping away from crater. Yellow box outlining high fractured reflectors. Green box outlining approximately horizontal reflectors. For location of azimuth line 6 see Figure 16.

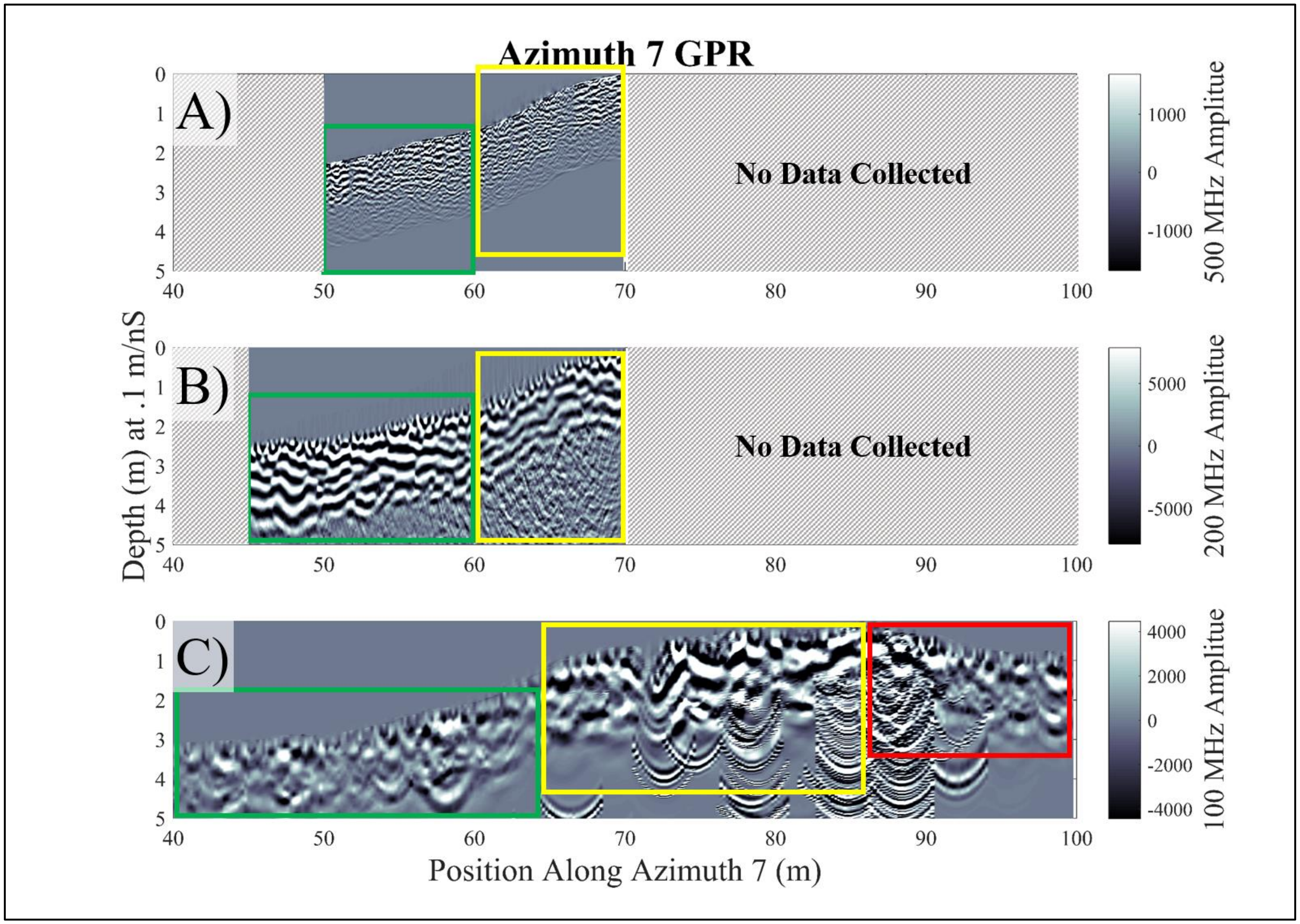

Figure 33 – GPR azimuth line 7. A – 500 MHz GPR data, B – 200 MHz GPR data, C – 100 MHZ GPR data. Color bars on right scaled within two standard deviations of the mean of each dataset. X-axis as position along azimuth line 7 in meters. Y-axis as depth below highest elevation on line in meters. Red box outlining reflectors dipping away from crater. Yellow box outlining high fractured reflectors. Green box outlining approximately horizontal reflectors. For location of azimuth line 7 see Figure 16

5.3 ERT Results

5.3.1 Double-azimuth ERT transects

ERT azimuth line 10-1 is a combination of azimuth lines 10 and 1, transects the full crater diameter approximately north-south, is ~165 meters in length, and is sensitive to depths of ~35 meters (Figure 34). Azimuth line 10-1 starts at 84 m from the center on azimuth line 10 and ends at 82.5 meters on azimuth line 1. The inverted resistivity model can be separated into several distinct zones. Near the exposed north and south rims there is a zone of high resistivity (1000-3000+ Ohm-m) interpreted as the fractured and uplifted limestone rim. Beneath the exposed rims, there are large zones of low resistivity (10-50 Ohm-m) interpreted as the undisturbed or moderately disturbed Fredericksburg group and Antlers formation. Within the crater, there is a large zone of low resistivity (10-100 Ohm-m) with several small high resistive inclusions (100-500 Ohm-m) interpreted as the fine grained aeolian and lacustrine crater fill. There are also areas of moderate to high resistivity areas dipping inward from the crater rim (300-2000 Ohm-m) interpreted as the ejecta fill that lined the original crater shortly after formation. Additionally, the ejecta fill zone has a sub-zone of high resistivity near the center that is likely caused by the rock flour formed during impact. On this transect, the exposed rim has a diameter of ~145 m, while the ejecta fill has a diameter of ~110 m and depth of 30 m below the present crater fill elevation.

ERT azimuth line 13-6 is a combination of azimuths lines 13 and 6, transects the full crater diameter approximately east-west, is ~190 m in length, and is sensitive to depths of ~35 meters (Figure 35). Azimuth line 13-6 starts at 98 m from the center on azimuth line 13 and ends at 96 m on azimuth line 6. Azimuth line 13-6 contains a similar resistivity distribution as azimuth line 10-1. However, the ejecta and rock flour zone is larger in size and contains higher resistivity values. Additionally, on this transect, the exposed rim has a diameter of ~165 m, while the ejecta fill has a diameter ~110 m and depth of 30 from the present crater fill elevation. On azimuth line 13-6 the ejecta fill and rock flour zone is not centered beneath the exposed rim locations. From the west rim the center is ~70 m and is ~95 m from the east rim.

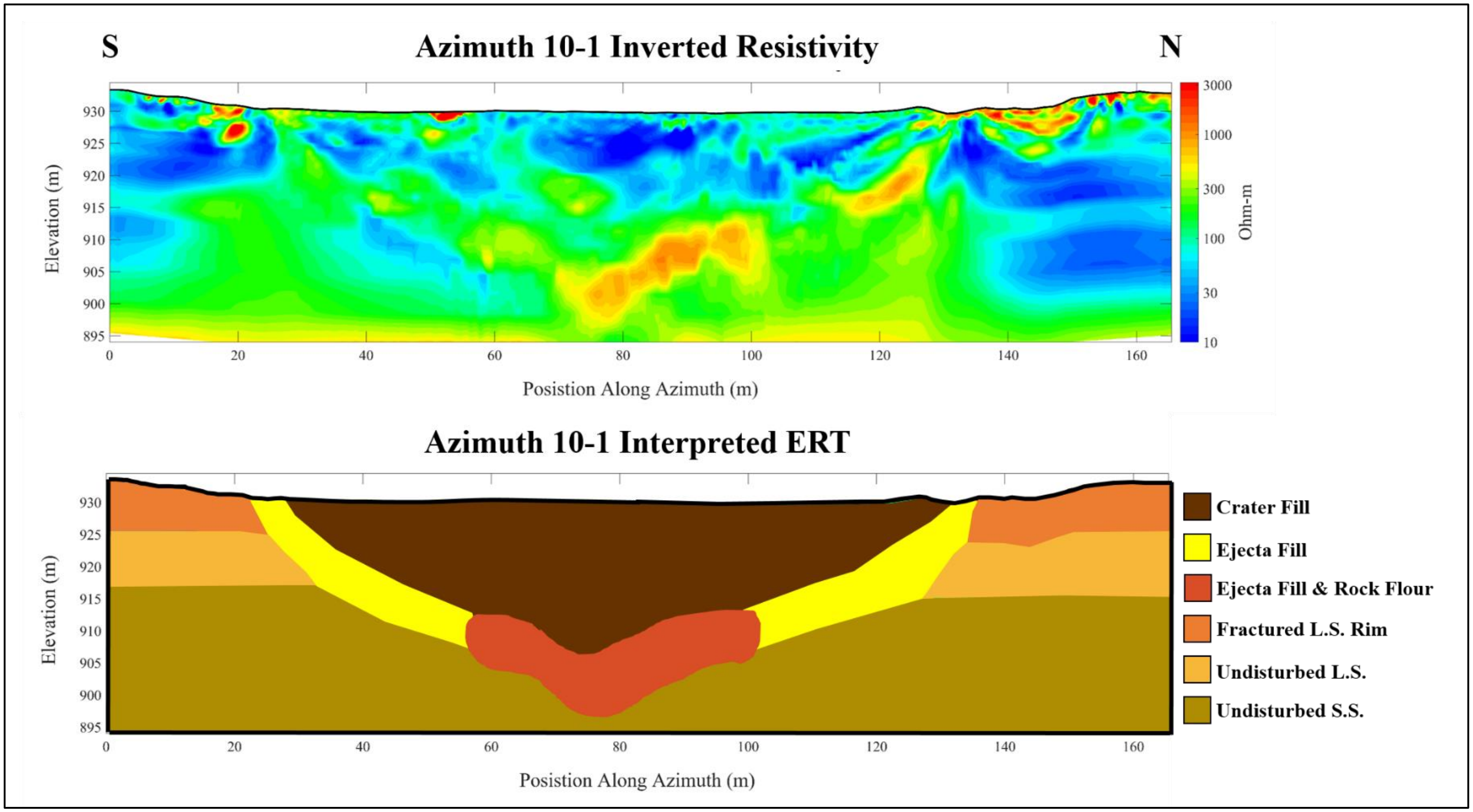

Figure 34 – Azimuth line 10-1 inverted and interpreted resistivity. Top – inverted resistivity, y-axis in elevation, x-axis in position along azimuth line 10-1, color scale to right. Bottom – interpreted ERT resistivity zones with legend to right. Location of azimuth line 10-1 shown on Figure 16

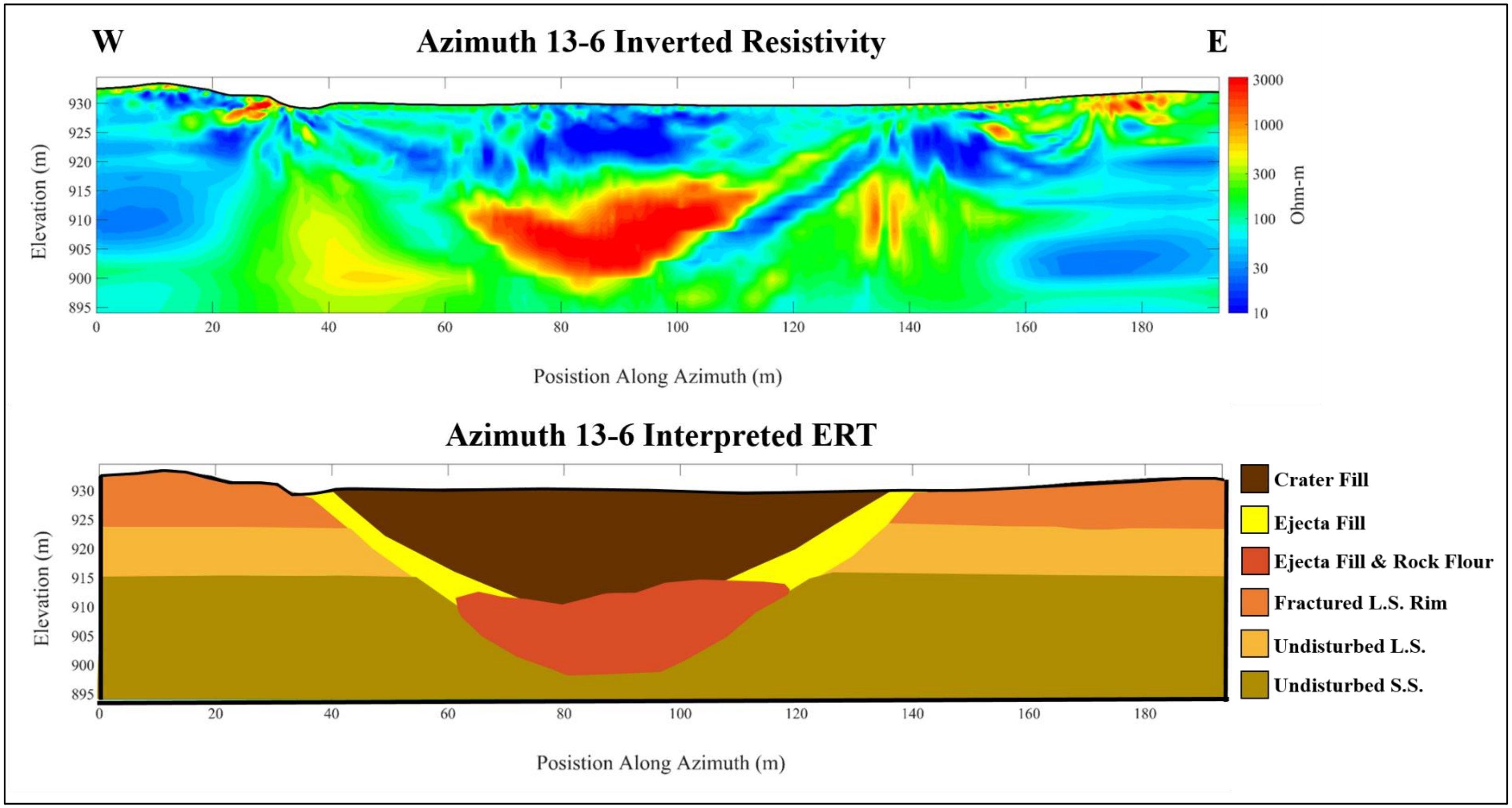

Figure 35 – Azimuth line 13-6 inverted and interpreted resistivity. Top – inverted resistivity, y-axis in elevation, x-axis in position along azimuth line 13-6, color scale to right. Bottom – interpreted ERT resistivity zones with legend to right. Location of azimuth line 13-6 shown on Figure 16

5.3.2 Comparison of multiple and single azimuth ERT transects

In addition to the double-azimuth ERT transects, single azimuth transects were collected to image the crater rim in greater detail. The single azimuth transects were collected with electrode spacing's of 0.75-1.0 m as opposed to 1.5-1.75 m used on the double-azimuth transects. With smaller electrode spacing, the injected electric current does not penetrate as deep and is not as sensitive to deeper features as is the case with larger electrode spacing. Double-azimuth transects that were collected over the same position as single-azimuth transects are used to help interpret features observed in the single-azimuth transects that would not be possible without the deeper-penetrating data. A sub-section of azimuth line 10-1 transect (Figure 36, bottom) and azimuth line 1 transect (Figure 36, top) show consistent representations of the highly resistive rim, low-resistivity undisturbed strata, and low-resistivity crater fill. The different transects exhibit some differences in the resistivity distribution of the ejecta fill, but the interpreted overall shape and location of the zone is the same. A sub-section of azimuth line 13-6 transect (Figure 37, bottom) and azimuth line 6 transect (Figure 37, top) also show consistent representations of the highly resistive rim, low-resistivity undisturbed strata, and low resistivity crater fill. The azimuth line 6 transect does not contain the large ejecta fill and rock flour zone that is present in azimuth 13-6 transect, but this can be attributed to the lack of sensitivity to that depth. However, the azimuth line 6 transect does display a moderate resistivity zone (100-500 Ohm-m) that can be interpreted as the upper portion of the ejecta fill zone close to the surface.

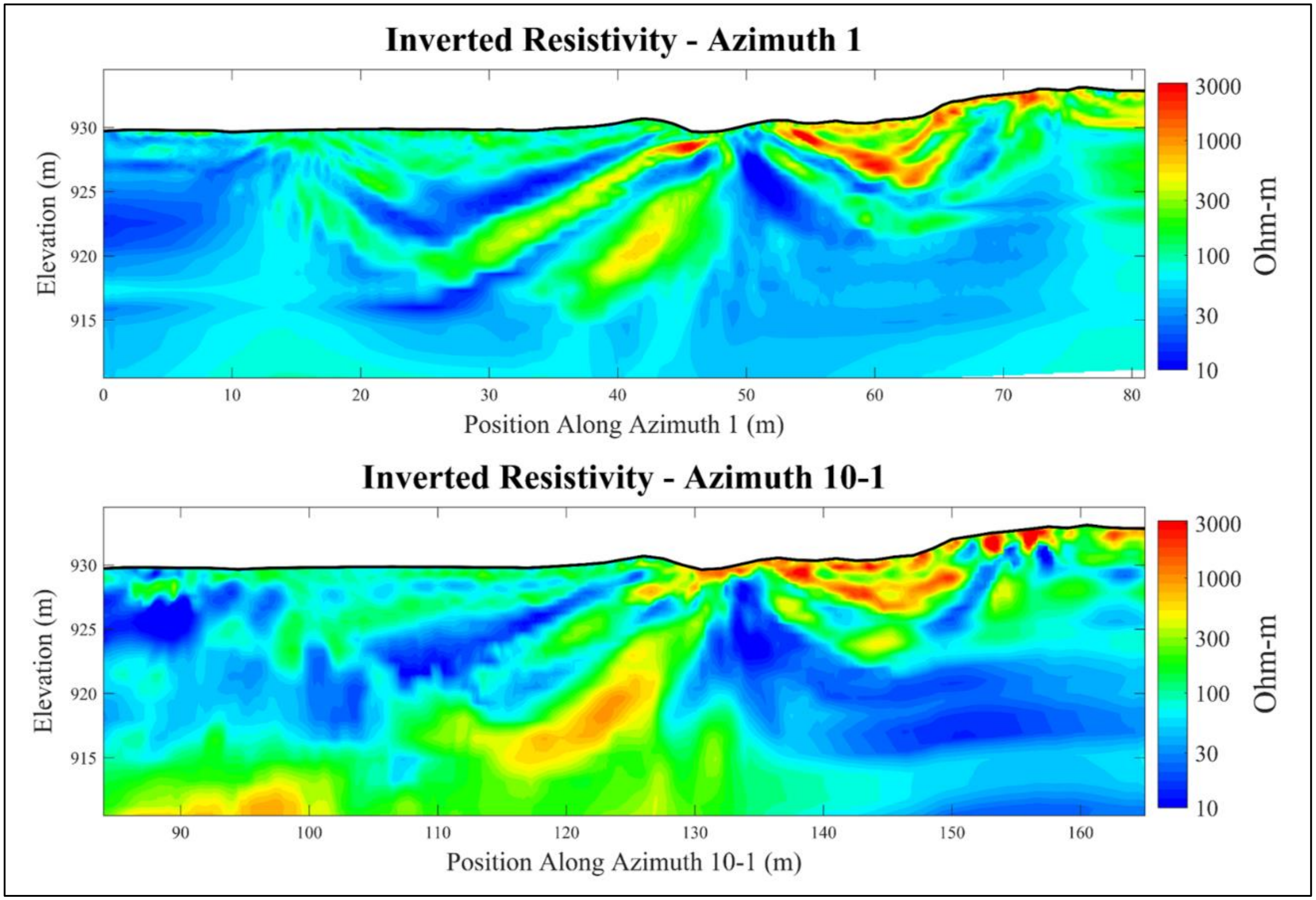
Inverted Resistivity - Azimuth 1

Inverted Resistivity - Azimuth 10-1

Figure 36 – Comparison of multiple (10-1) and single (1) azimuth ERT transects. Top – Inverted resistivity of azimuth line 1, y-axis in elevation, x-axis in position along azimuth line 1, and color scale to right. Bottom - Inverted resistivity sub-section of azimuth line 10-1, y-axis in elevation, x-axis in position along azimuth line 10-1, and color scale to right. Location of azimuth lines shown on Figure 16

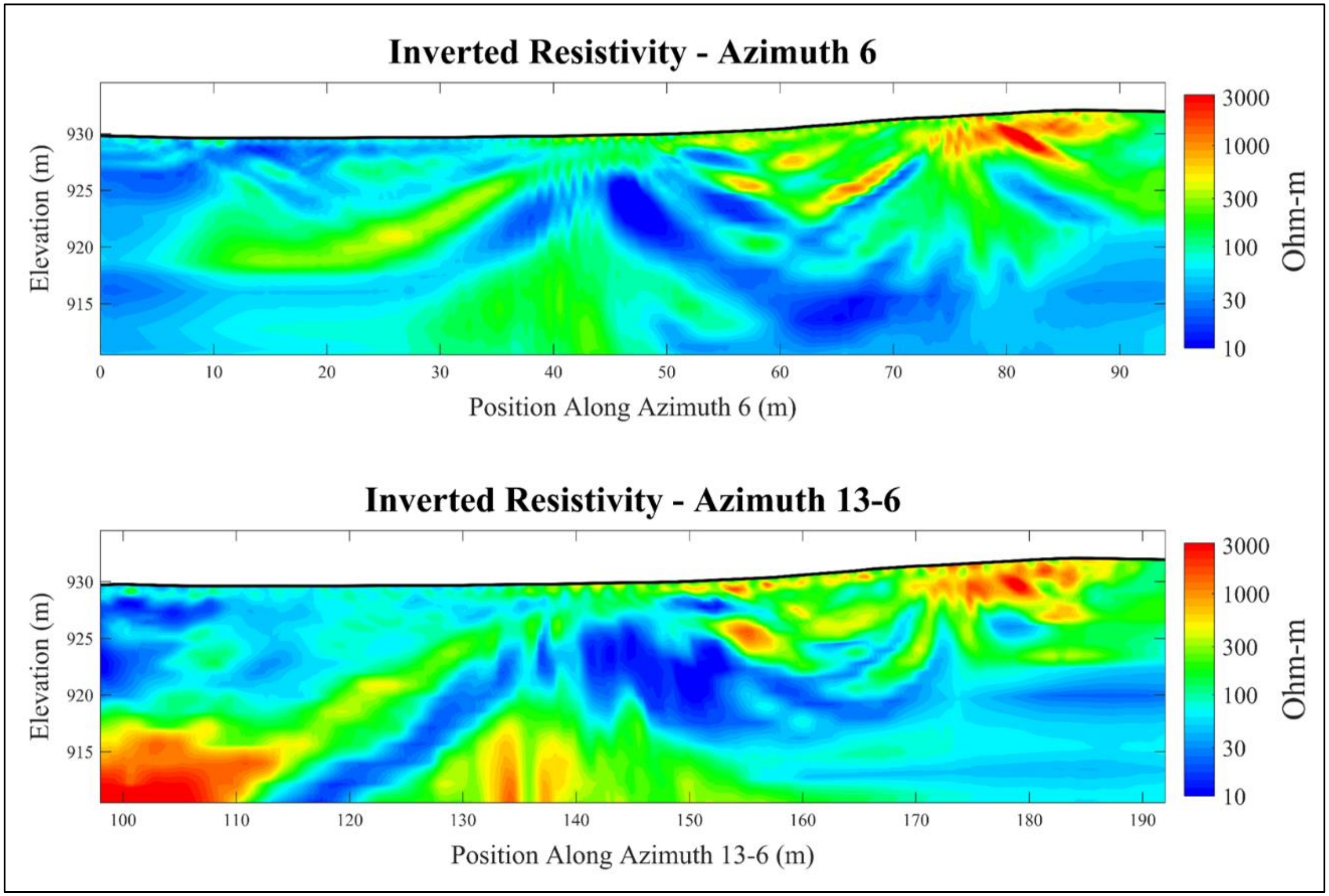

Figure 37 – Comparison of multiple (13-6) and single (6) azimuth ERT transects. Top – Inverted resistivity of azimuth line 6, y-axis in elevation, x-axis in position along azimuth line 6, and color scale to right. Bottom - Inverted resistivity sub-section of azimuth line 13-6, y-axis in elevation, x-axis in position along azimuth line 13-6, and color scale to right. Location of azimuth lines shown on Figure 16

5.3.3 Single azimuth ERT transects

ERT azimuth line 1 transects from the center of the crater to the northern rim, is ~83 meters in length, and is sensitive to depths of ~20 meters (Figure 38). Near the exposed rim there is a zone of high resistivity (1000-3000+ Ohm-m) interpreted as the fractured and uplifted limestone rim. Beneath the exposed rim, there are large zones of low resistivity (10-100 Ohm-m) interpreted as the undisturbed or moderately disturbed Fredericksburg group and Antlers formation. Within the crater, there is a large zone of low resistivity (10-300 Ohm-m) interpreted as the fine grained aeolian and lacustrine crater fill. There is an area of moderate to high resistivity areas dipping inward from the crater rim (100-1000 Ohm-m) interpreted as the ejecta fill that lined the original crater shortly after formation. On this transect, the exposed rim is ~75 m from the center of the azimuths, while the ejecta fill is ~45 m.

The other transects (azimuth lines 4, 5, 6, and 7) are ~100 m in length and are sensitive to ~25 m depth. In general the interpreted resistivity zones of azimuth line 1 are also present in the other azimuths. Azimuth line 7 (Figure 39), is the most similar to azimuth line 1 as it is still within the circular portion of the crater. On this transect, the exposed rim is ~75 m from the center of the azimuths, while the ejecta fill is ~45 m. As the ERT transects move into the eastern portion of the crater, the exposed rim retreats farther from the center of the crater, but the ejecta fill zone remains in an approximately consistent location. On ERT azimuth line 6 (Figure 40), the exposed rim is ~85 m from the center of the azimuths, while the ejecta fill is ~45 m. On ERT azimuth line 5 (Figure 41), the exposed rim is ~90 m from the center of the azimuths, while the ejecta fill is ~40

m. On azimuth line 5 a zone of anomalous resistivity appears between the exposed crater rim and ejecta fill. On ERT azimuth line 4 (Figure 42), the exposed rim is ~85 m from the center of the azimuths, while the ejecta fill is ~45 m. There is also a zone of anomalous resistivity between the exposed crater rim and ejecta fill on azimuth line 4.

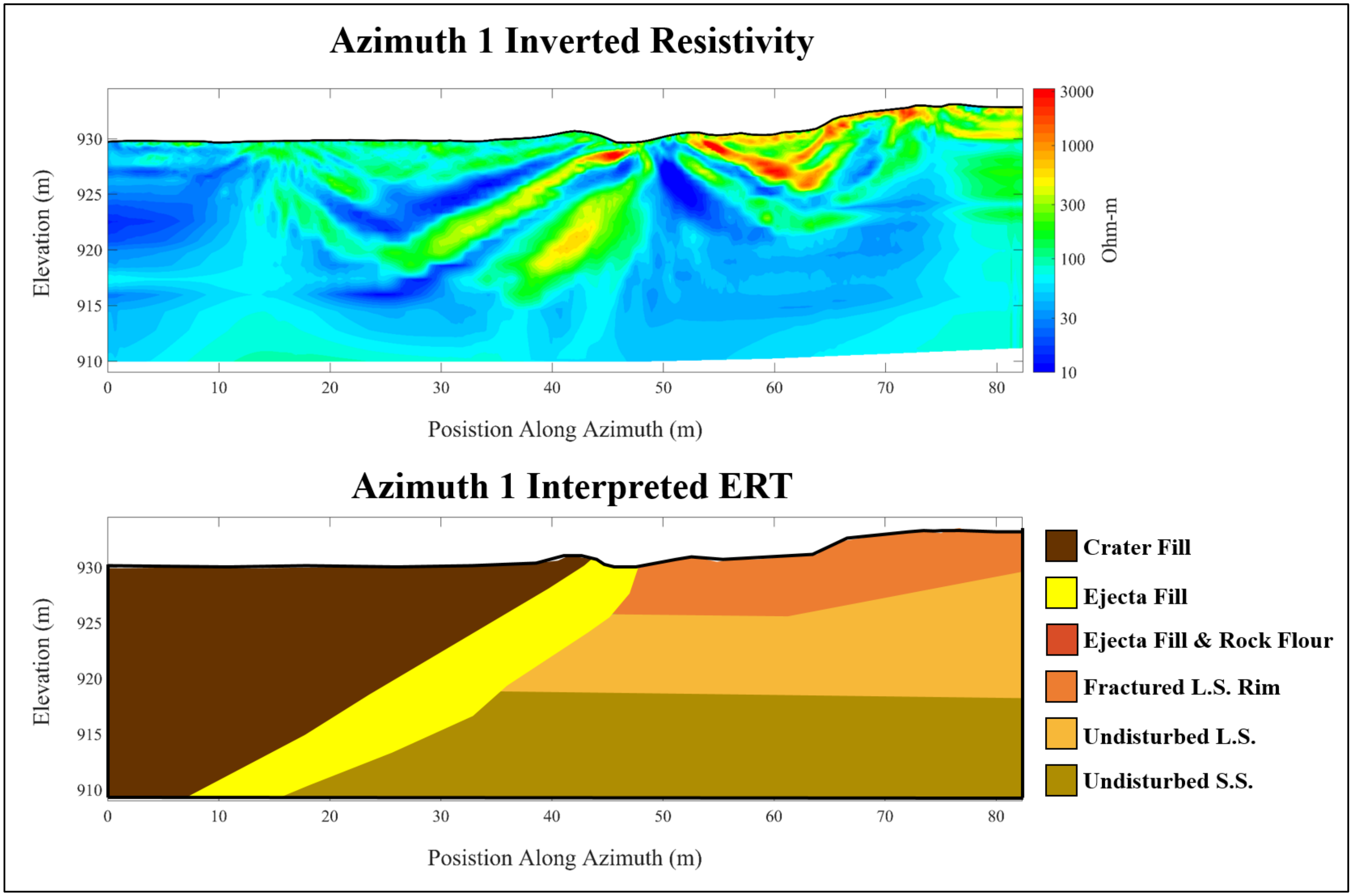

Figure 38 – Azimuth line 1 inverted and interpreted resistivity. Top – inverted resistivity, y-axis in elevation, x-axis in position along azimuth line 1, color scale to right. Bottom – interpreted ERT resistivity zones with legend to right. Location of azimuth line 1 shown on Figure 16

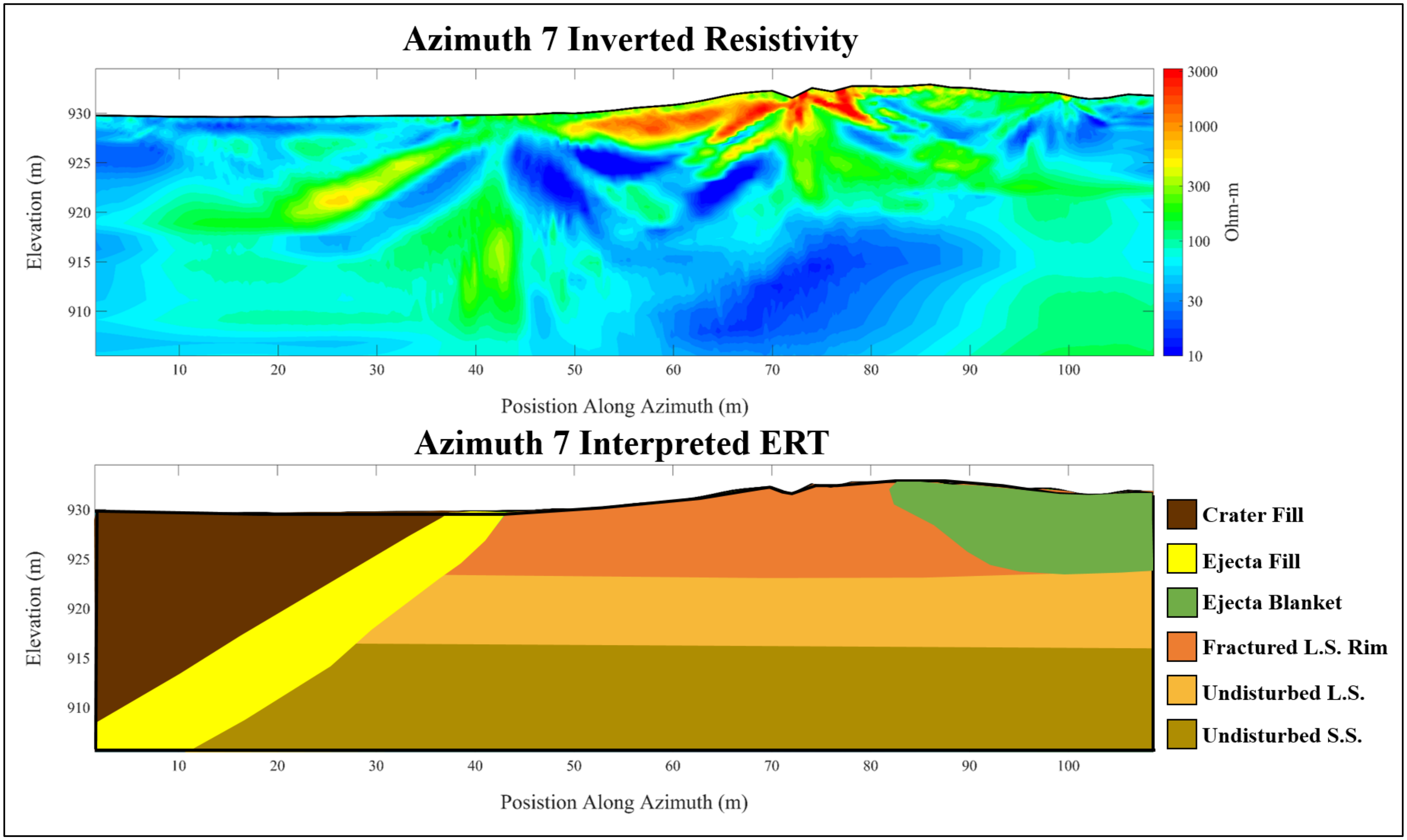

Azimuth 7 Inverted Resistivity

Azimuth 7 Interpreted ERT

Figure 39 – Azimuth line 7 inverted and interpreted resistivity. Top – inverted resistivity, y-axis in elevation, x-axis in position along azimuth line 7, color scale to right. Bottom – interpreted ERT resistivity zones with legend to right. Location of azimuth line 7 shown on Figure 16

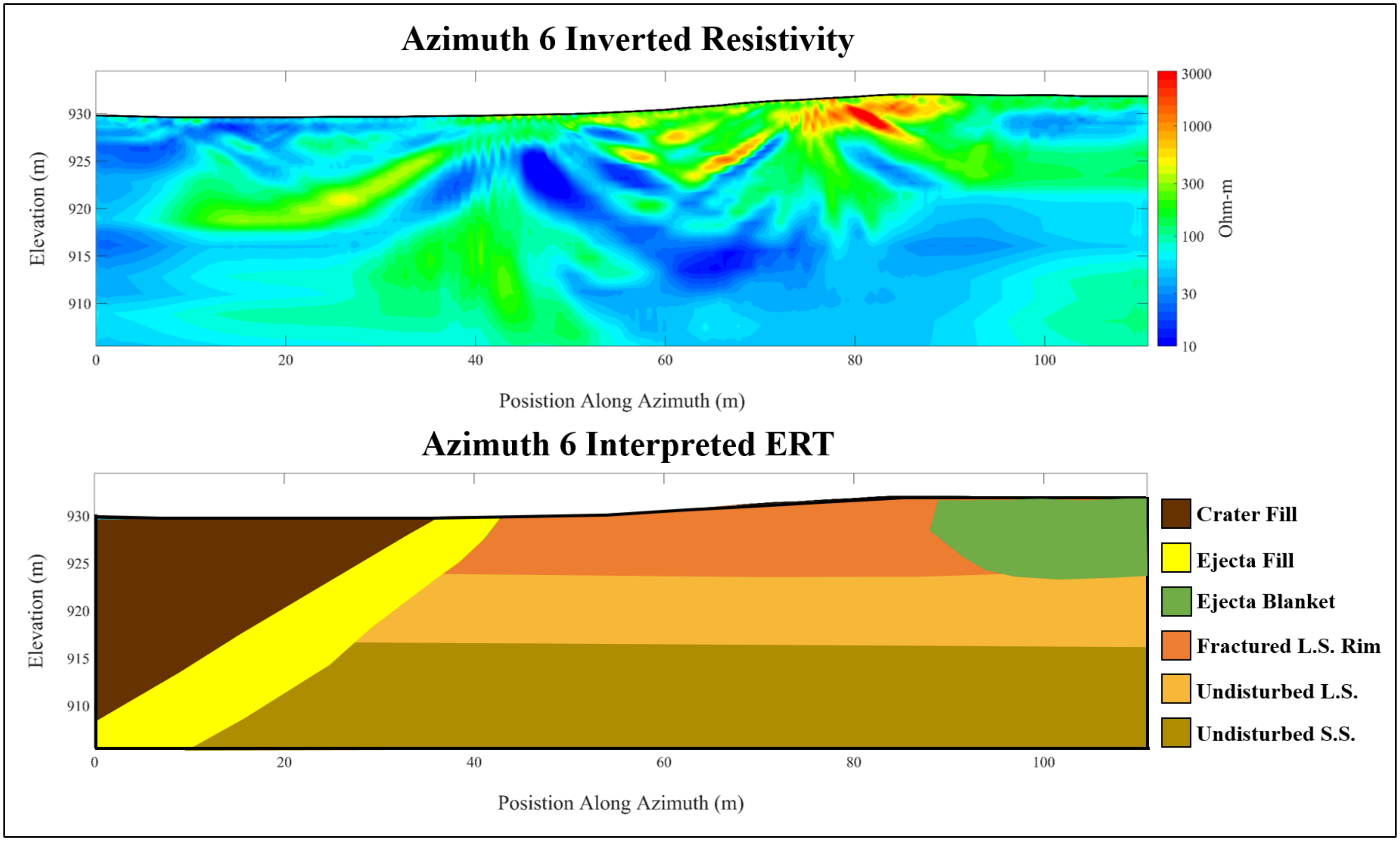
Azimuth 6 Inverted Resistivity

Azimuth 6 Interpreted ERT

Figure 40 – Azimuth line 6 inverted and interpreted resistivity. Top – inverted resistivity, y-axis in elevation, x-axis in position along azimuth line 6, color scale to right. Bottom – interpreted ERT resistivity zones with legend to right. Location of azimuth line 6 shown on Figure 16

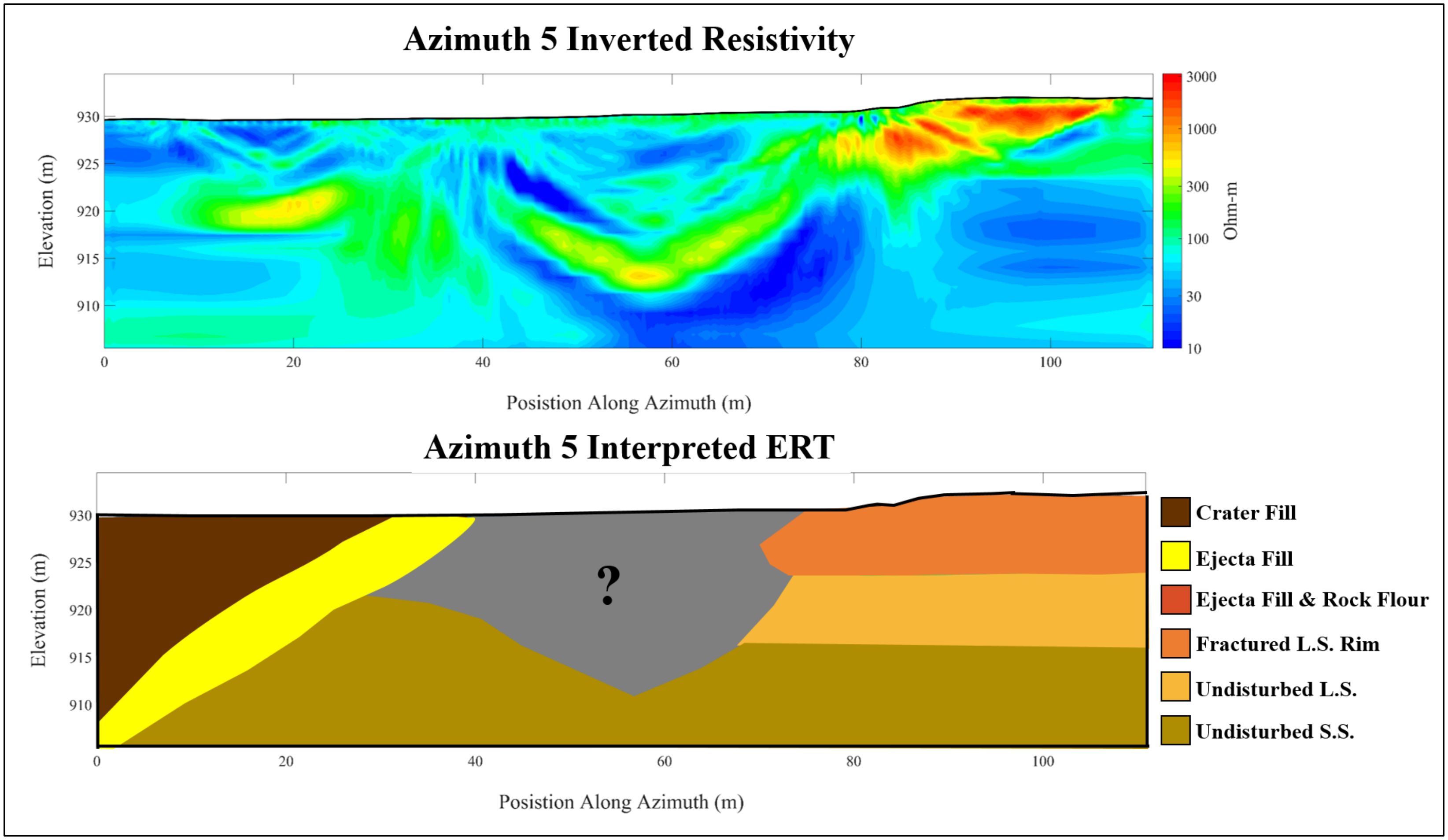

Figure 41 – Azimuth line 5 inverted and interpreted resistivity. Top – inverted resistivity, y-axis in elevation, x-axis in position along azimuth line 5, color scale to right. Bottom – interpreted ERT resistivity zones with legend to right. Location of azimuth line 5 shown on Figure 16

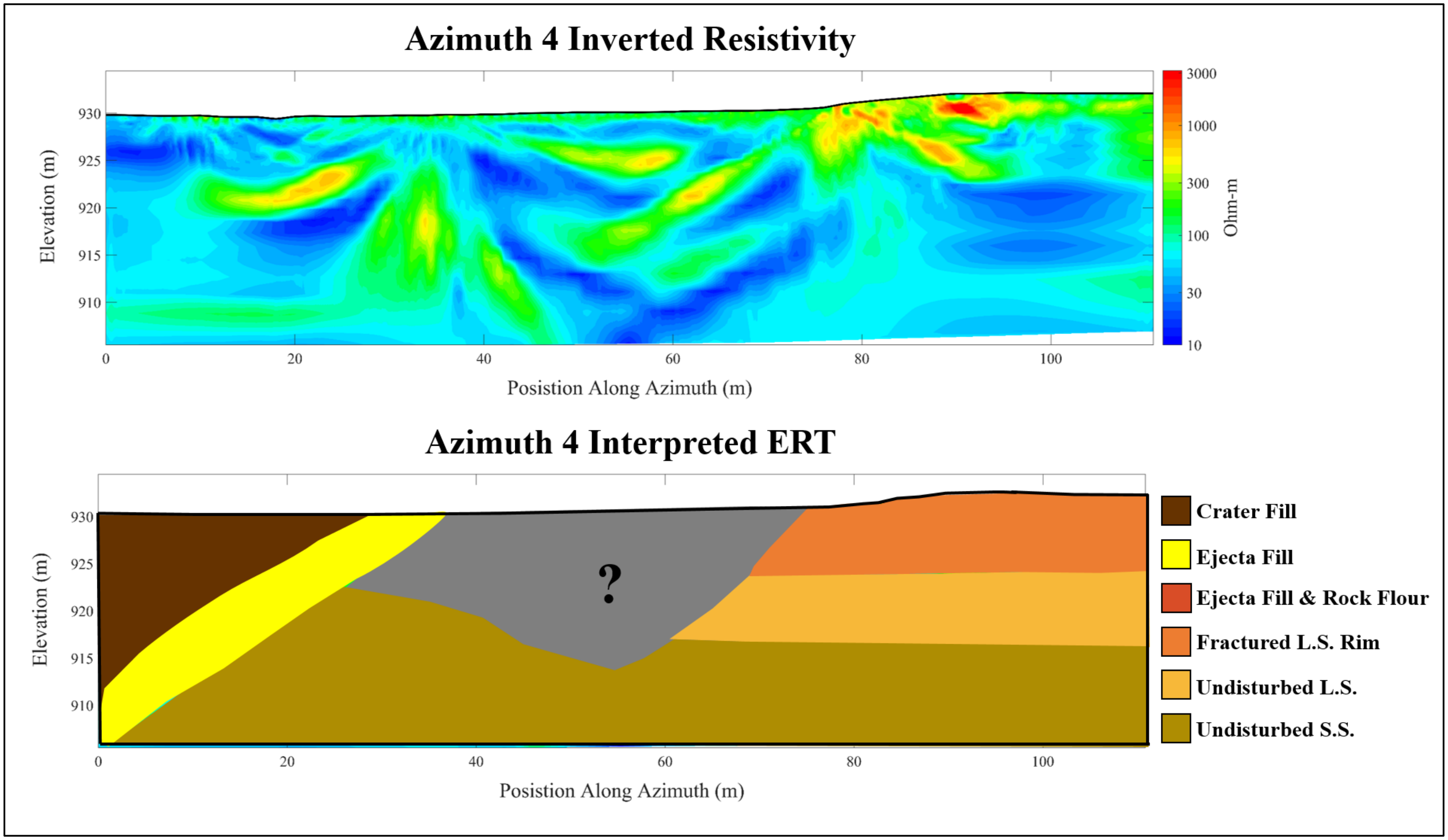

Figure 42 – Azimuth line 4 inverted and interpreted resistivity. Top – inverted resistivity, y-axis in elevation, x-axis in position along azimuth line 4, color scale to right. Bottom – interpreted ERT resistivity zones with legend to right. Location of azimuth line 4 shown on Figure 16

5.3.4 Summary of ERT results

Several distinct zones were identified throughout the ERT azimuth lines: a highly resistive zone near the crater rim interpreted to be fractured limestone rim, a lower resistive zone beneath the rim interpreted to be the undisturbed or moderately disturbed Fredericksburg group and Antlers formation, a zone of low conductivity within the crater interpreted to be the lacustrine and aeolian crater fil, a zone of moderate resistivity dipping inward from the crater rim interpreted to be the ejecta fill that lined the original crater, and a deep zone of high resistivity interpreted to be the base of the ejecta fill and rock flour. Three-dimensionally, the cross crater transects (azimuth lines 10-1 and 13-6) have good agreement on the location of the base of the ejecta and rock flour zone (Figure 43). On azimuth line 13-6 the center of this zone is to the west of the azimuthal center point, and on azimuth line 10-1 the center is to the south of the azimuthal center point. This suggest that the center of the crater lies to the south-west of the azimuthal survey grid center point. The mine shaft dug by the Evan’s geologic society is also to the southwest of the survey grid center and is the best approximation for the true center of the crater. Because azimuth line 13-6 shows that ejecta and rock flour zone is not centered about the eastern rim of the crater, it is suggested that the original crater was circular and that erosion has widened the crater towards the east.

The single azimuth transects show that even as the interpreted crater rim becomes farther from the center of the crater, the interpreted ejecta fill zone is at a consistent distance from the center (Figure 44). However, only a portion of the ejecta fill zone is imaged in azimuth lines 4 and 5 due to the lack of sensitivity at the end of the transects.

Additionally, azimuth lines 4 and 5 have an anomalous resistivity zone not seen in other azimuth lines. This zone is very heterogeneous and might be explained by the weathering of the crater rim, reducing the height and increasing the apparent distance from the center of the crater. To confirm that the zone interpreted as the ejecta fill in azimuth lines 4 and 5 is correct, additional ERT lines should be collected in the eastern portion of the crater. The line(s) should be start ~30 m to the west of the survey grid center point and end at the beginning of the exposed rim near azimuth lines 4 and 5. This survey geometry will center the location of the interpreted ejecta fill zone and maximize sensitivity.

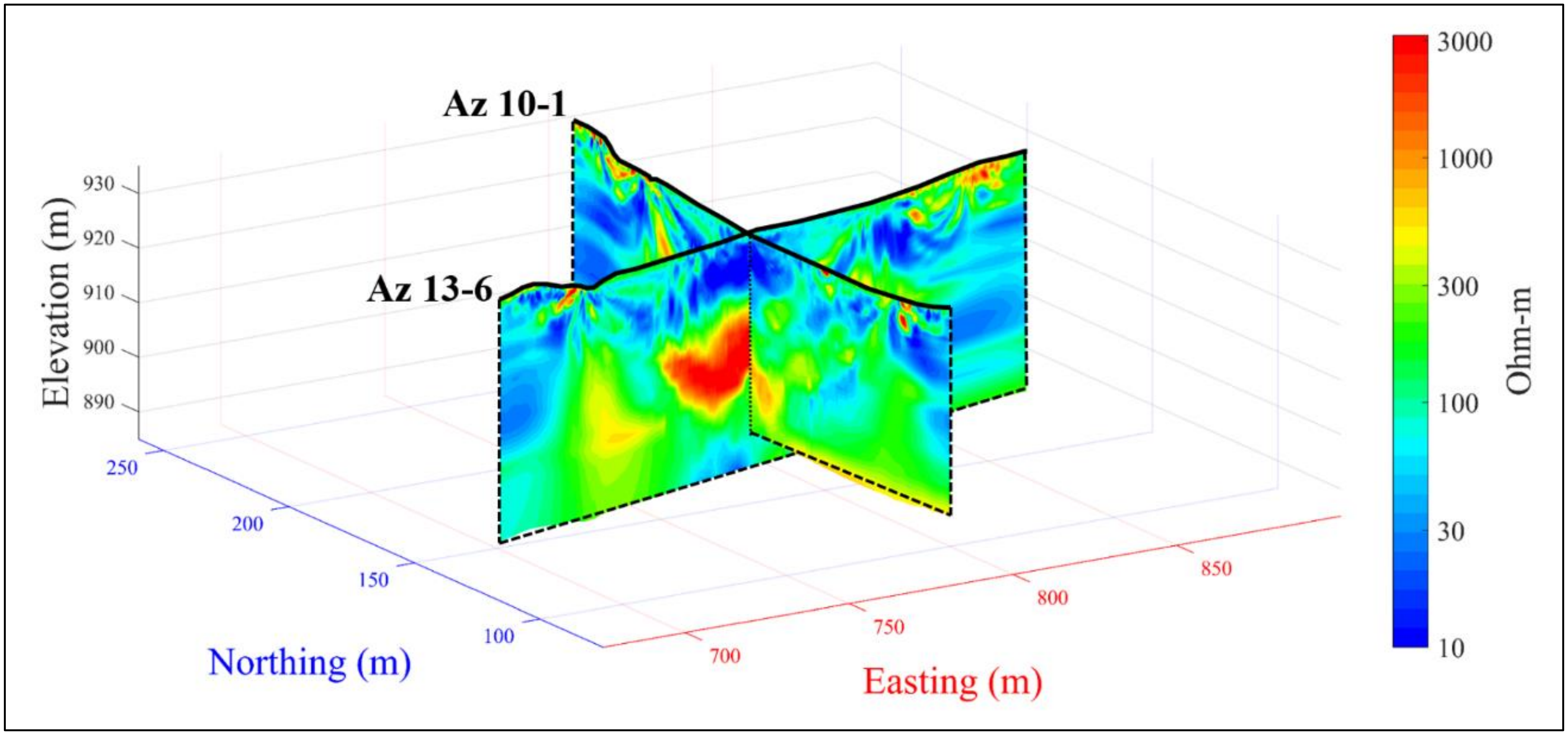

Figure 43 – 3 dimensional view of ERT azimuth lines 13-6 and 10-1. X-axis (red) in local easting, Y-axis (blue) in local northing, Z axis (black) in elevation. Local easting and northing coordinates referenced from UTM zone 13N 738000E and 3516000N. View from southwest of crater. Color Bar to right.

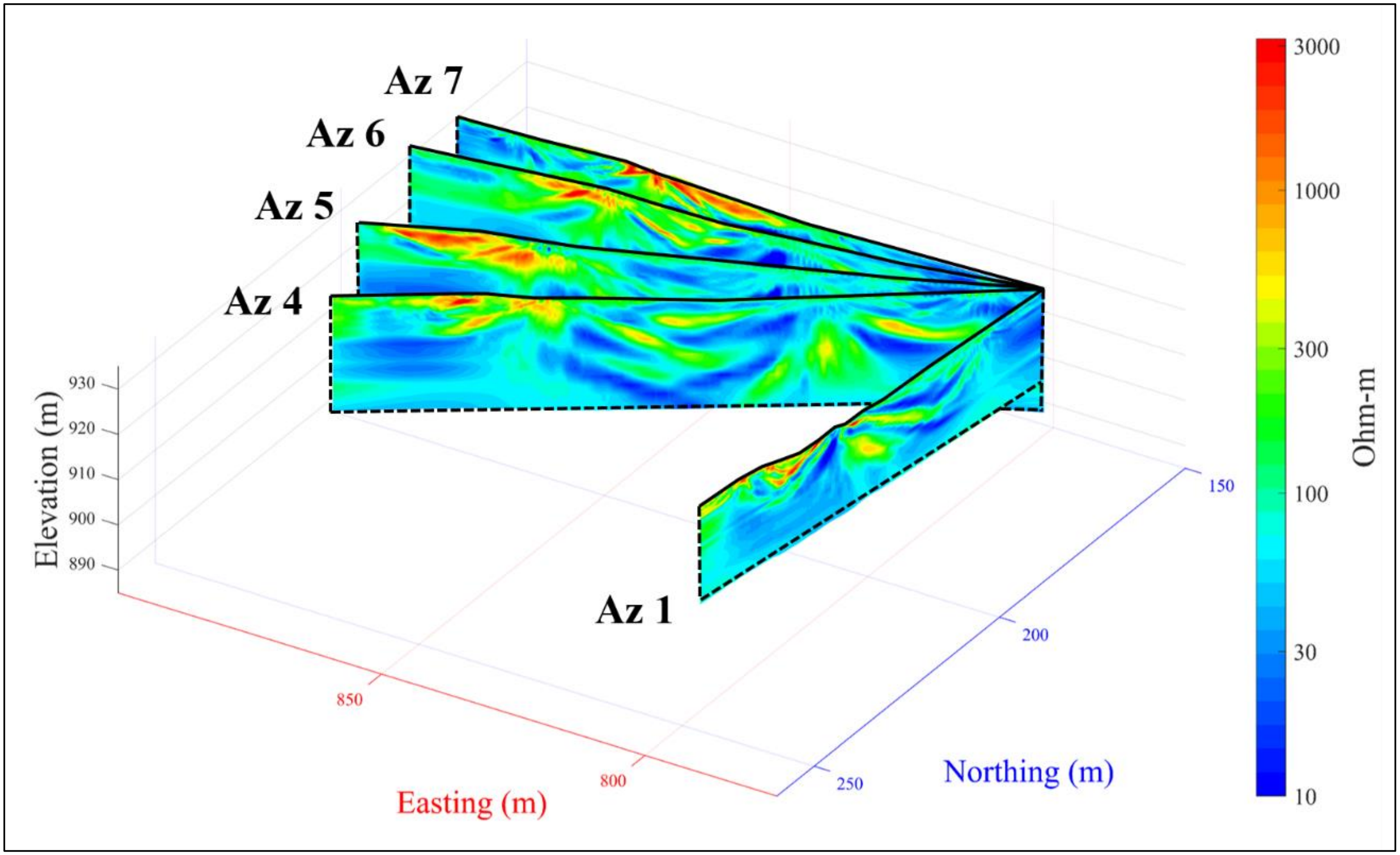

Figure 44 – 3 dimensional view of ERT azimuth lines 1, 4, 5, 6, and 7. X-axis (red) in local easting, Y-axis (blue) in local northing, Z axis (black) in elevation. Local easting and northing coordinates referenced from UTM zone 13N 738000E and 3516000N. View from southwest of crater. Color Bar to right.

6. DISCUSSION AND CONCLUSION

Geophysical evidence suggests that the Odessa Meteorite Crater was indeed circular at the time of formation. Topography of the eastern rim differs significantly from established crater morphology indicating that some process has modified the original crater in the east. Additionally, projection of the interpreted ejecta fill zones from the ERT data (Figure 45) shows that the ejecta fill is approximately circular even though the exposed crater rim is not. The circular pattern is ~110 meters in diameter. Just outside of the projected ejecta fill zone lies the "Gryphaea bed" identified by *Evans and Mear* (2000) as the base of the uplifted limestone Fredericksburg group. This bed is also outlined in blue on the Trench C cross section (Figure 9). The gryphaea bed is part of the folded and thrust anticline that would have formed the original crater rim. The location of the gryphaea bed represents the minimum diameter of the original crater rim and the start of the ejecta fill. Three mechanisms are conceptually analyzed as the possible cause of the unique crater shape present.

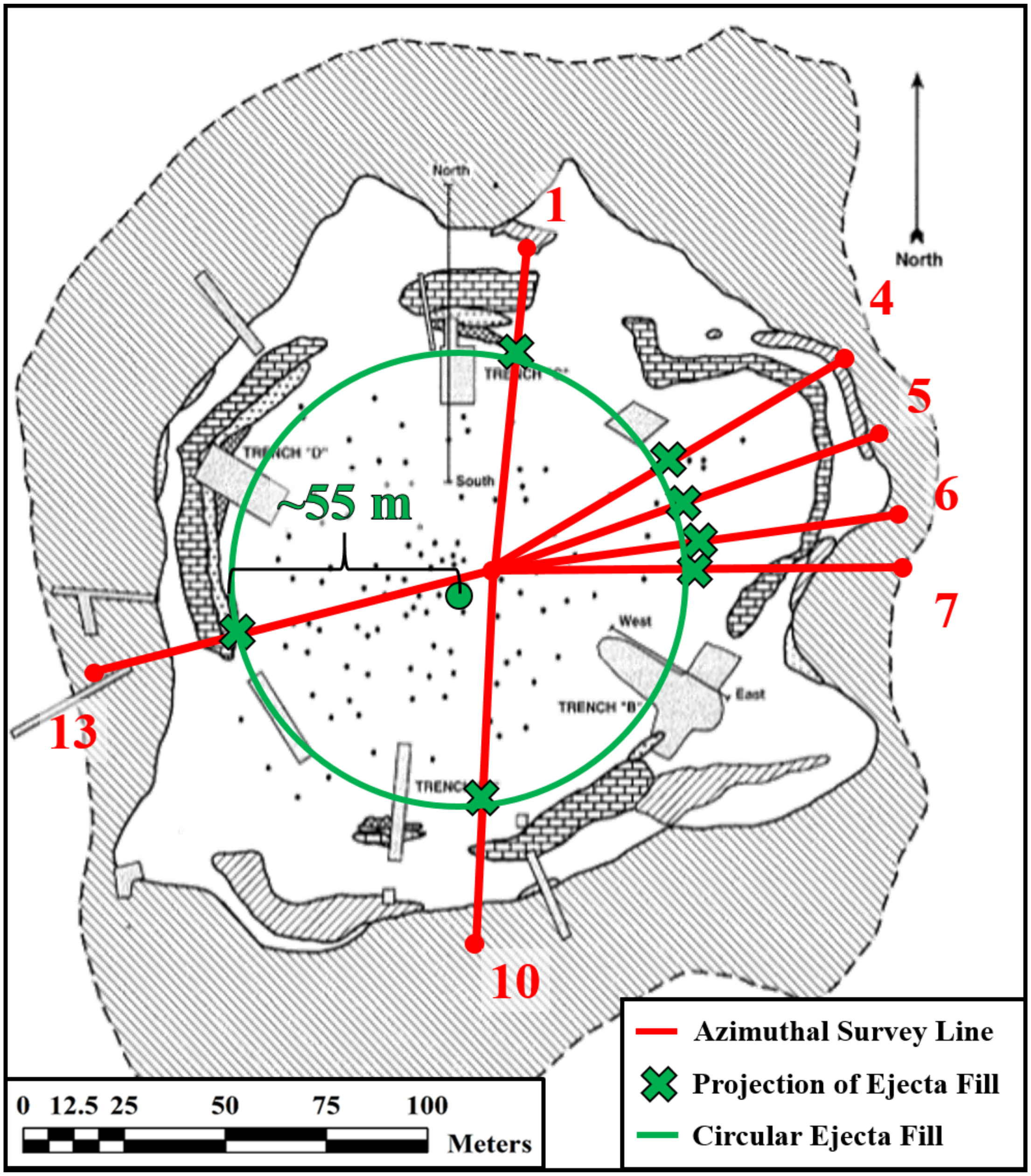

Figure 45 – Projection of ejecta fill zone on to Evan's geologic map. Projection from ERT interpretations as green crosses. Azimuthal survey lines shown in red, exposed crater rim in black, circular approximation of ejecta fill in green. Projection ~55 meters in radius. Scale bar in lower left.

6.1 Preferential Erosion of the Crater Rim

Using an erosional model in which the steeper inner wall of the crater rim erodes faster than the gently sloping outer rim, the crater rim will appear to widen and decrease in height through time. The initial crater rim would have been located between the current rim and projection of the ejecta fill (Figure 46). If erosion was the sole process responsible for the unique crater shape, the diameter of the Odessa Meteorite Crater was ~120 m at the time of formation with a majority of the rim having been eroded back ~10 m, with the eastern portion having been eroded back ~40 m. Given that 63.5 thousand years have elapsed since formation of the crater (*Holliday et al.*, 2005), the rim must have eroded backwards at rates of -0.6 mm/yr in the east and ~.15 mm/yr in the rest of the crater.

These erosional rates are up to three times larger than the largest rates found by *Smith et al.* (1995) (0.2 mm/yr) in flowing water, but are within the ranges complied by *Stephenson and Finlayson* (2009) (0.01 – 13.6 mm/yr). When considering that the uplifted limestone rim would have been heavily fractured, the erosional rates calculated for the crater rim fall within reason. However, only extreme geologic heterogeneity would have allowed the crater to have preferentially weathered to the east so drastically. This behavior cannot be completely explain by the qualitative increase in fracture density identified by the GPR to the east. Additional mechanisms must be at least partially responsible for the non-circularity in the east.

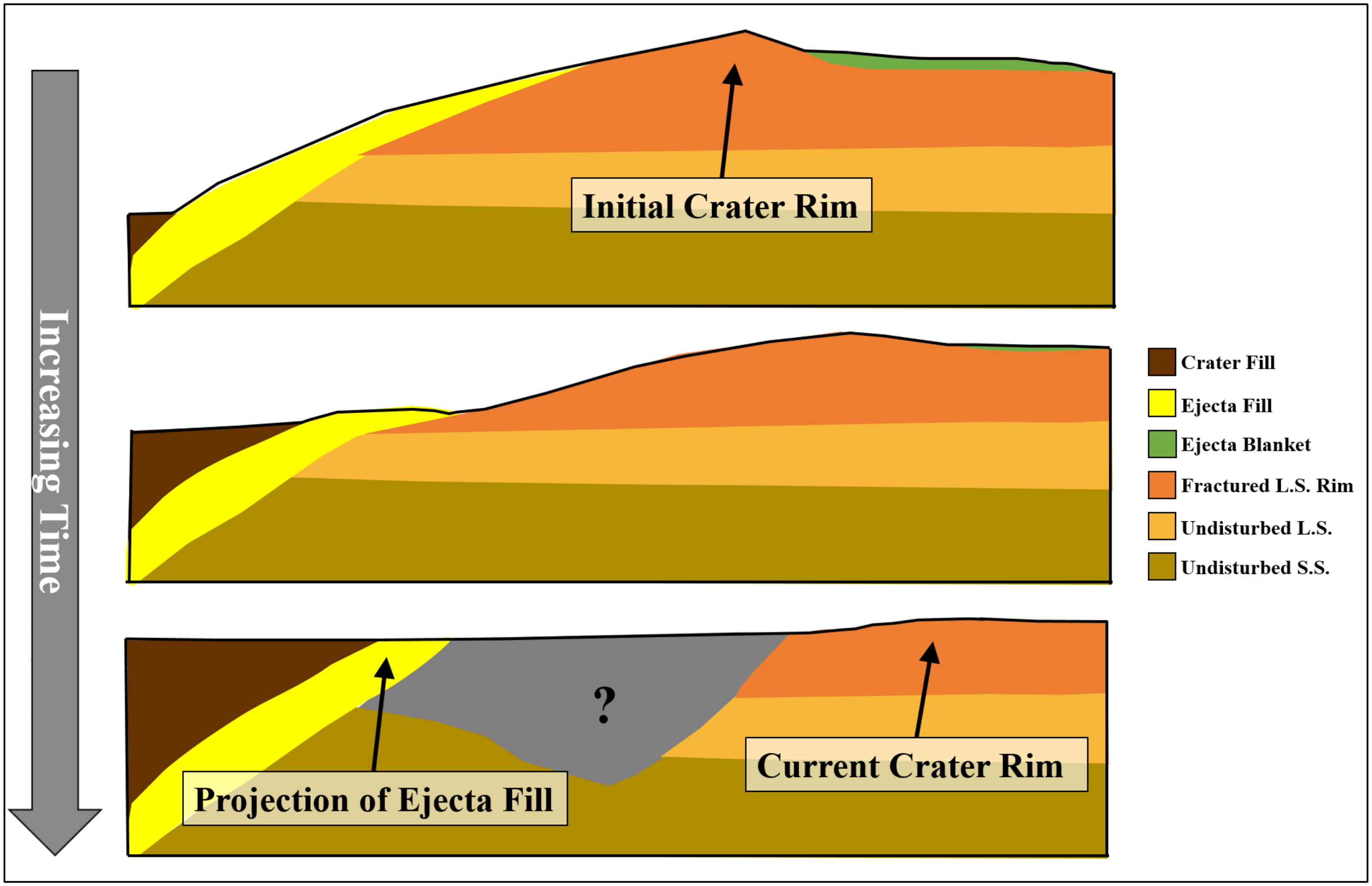

Figure 46 – Conceptual erosional model of the crater rim. Survey line 4 used as example. Crater rim decrease in height and increases in width through time.

6.2 Pre-existing Topography

The circular expansion of the shockwave generated by a meteorite impact in all but extremely oblique cases is well established by both theory and simulations (*Littlefield et al.*, 2007; *Melosh*, 1989; *Pierazzo and Melosh*, 1999). This behavior assumes a homogeneous half-space representation of the earth. If the pre-existing topography were present at the site of impact, the shockwave would not propagate spherically and a non-circular crater could be produced. To produce any noticeable modification from the expected circular shape, the topographic feature would conceptually have to be relatively large compared to the size of the meteorite. Further, the amount of topographic change needed should be simulated in future studies. However, the flat plains of west Odessa do not exhibit any large topographic changes that could have produced this behavior. Such a feature would have been rare and unexpected for this area, and cannot be considered a likely cause of the non-circular crater shape.

6.3 Simultaneous Impact

Several smaller, additional craters were identified by *Evans and Mear* (2000) during the original geologic study of the crater. The largest of which, “Crater No. 2”, was ~20 m in diameter and 5 m in depth and was located 30 m to the west of the main crater (*Evans and Mear*, 2000). This crater and the others were formed as fragments broke from the main meteorite in the atmosphere. Meteorites that travel at high hyper velocities penetrate the atmosphere with ease with only small fragments breaking off of the main meteorite, while meteorites traveling at slower speeds or smaller sizes can break apart in the atmosphere completely, never impacting the surface (*Melosh*, 1989). If the meteorite responsible for the Odessa Meteorite Crater was traveling at moderate velocities, the main meteorite could have broken apart into two significant fragments. It is proposed that the larger of the two was responsible for the main crater, and the smaller for the eastern portion of the current crater (Figure 47). The small crater measures approximately 50 m in diameter, slightly larger than Crater No. 2. This secondary crater also explains the anomalous zone detected in the ERT azimuth lines 4 and 5. The anomalous zone would now be interpreted as ejecta fill and crater fill of the secondary crater (Figure 48).

The near simultaneous impact would have induced complicated stress in the target rock that would certainly have affected the expected crater morphology. This could have manifested itself as the abnormal topography, higher fracture density, and non-circularity of the exposed rim. To confirm the hypothesis that a second, smaller, meteorite broke off from the main meteorite, more ERT lines should be collected in the eastern crater centered on the possible secondary crater.

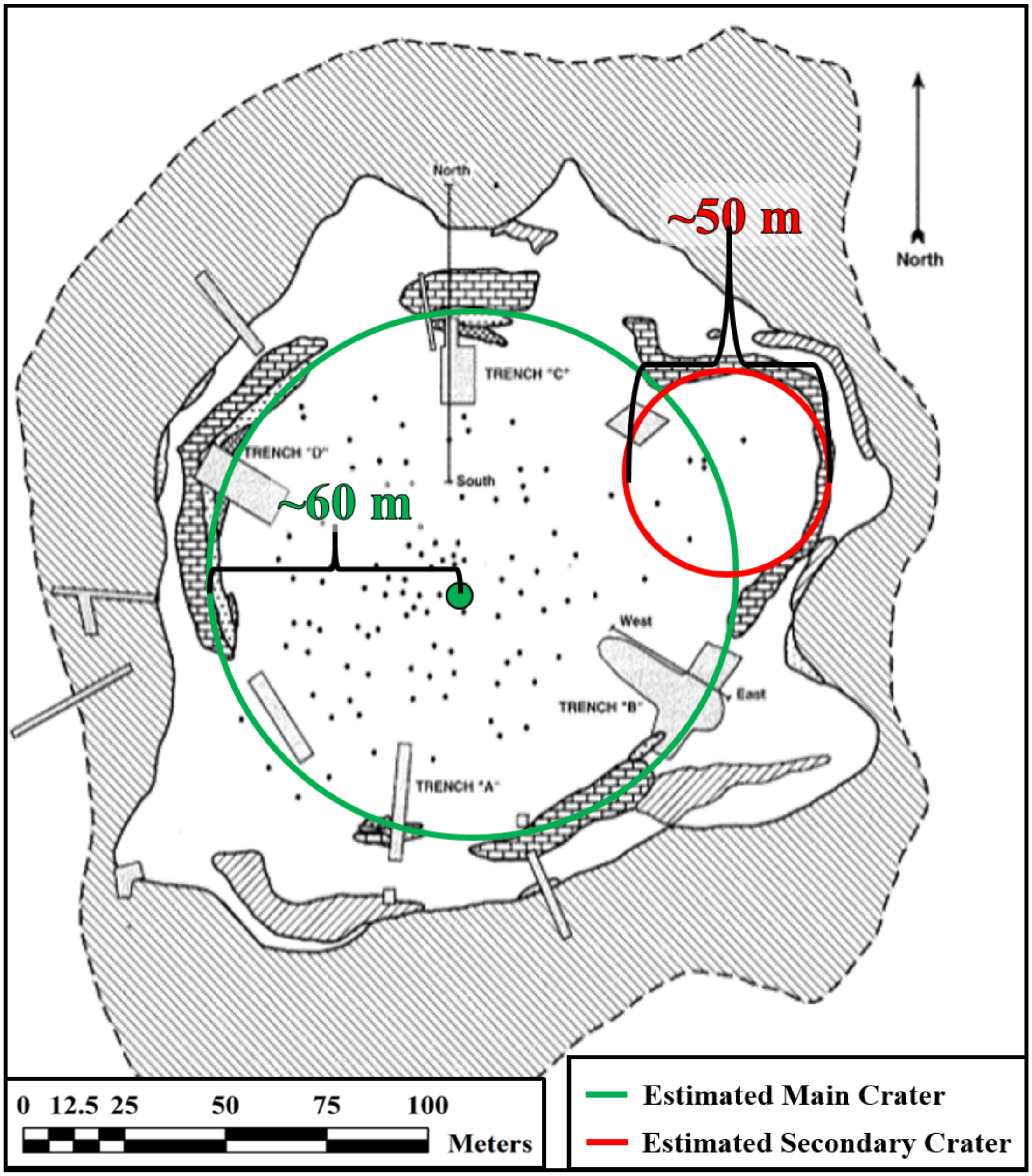

Figure 47- Projection of hypothesized secondary crater. Approximate main crate in green and secondary crater in red. Scale bar in lower left. Modified from Evans and Mear (2000).

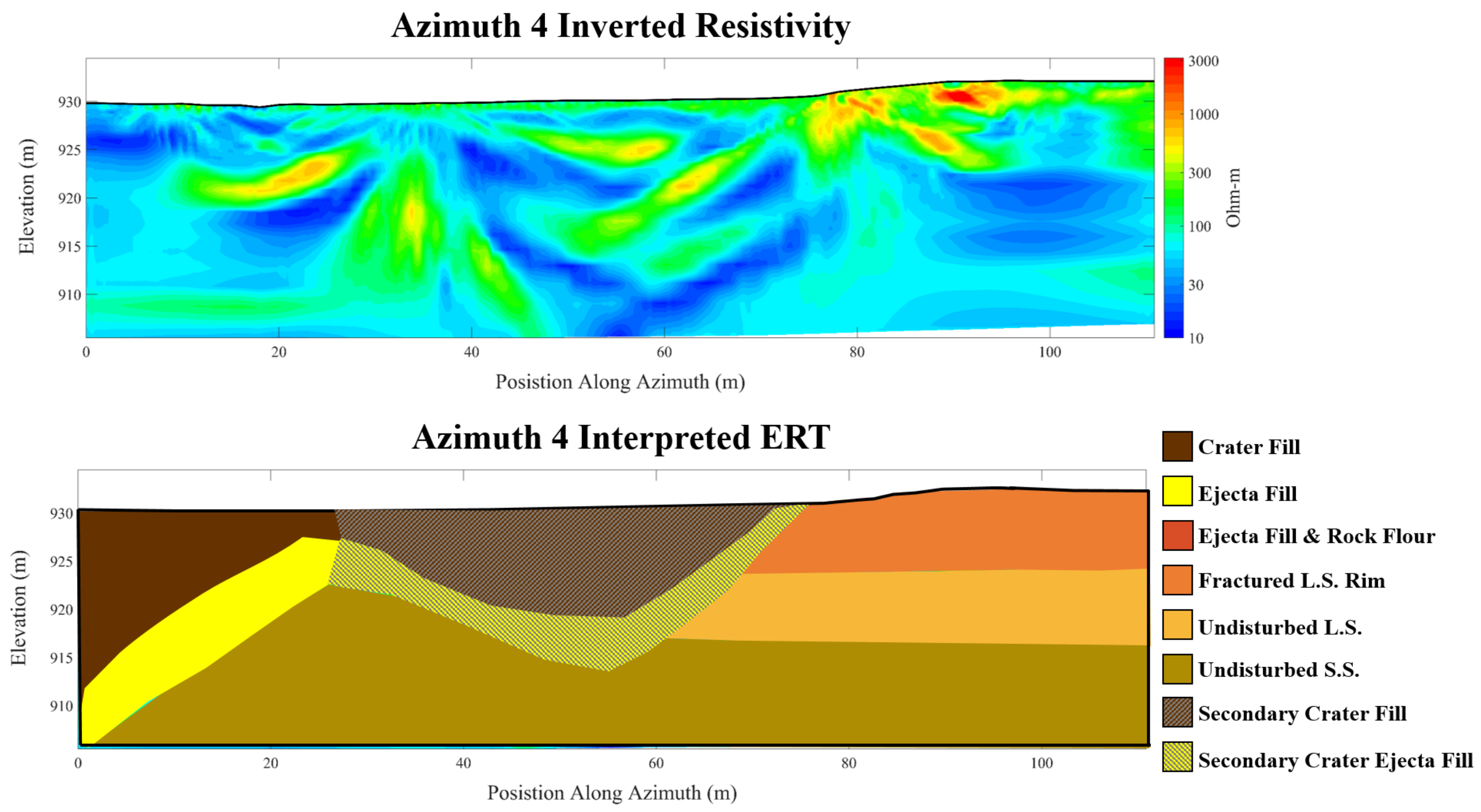

Figure 48 - Azimuth line 4 inverted and updated interpreted resistivity. Top – inverted resistivity, y-axis in elevation, x-axis in position along azimuth line 4, color scale to right. Bottom – interpreted ERT resistivity zones with legend to right. Location of azimuth line 4 shown on Figure 16

6.4 Conclusions

In order to refine the size estimates of the Odessa Meteorite Crater, GPR and ERT near-surface geophysical methods were utilized in the complex environment present at the crater. An azimuthal survey grid was constructed and Topographic, GPR, and ERT data were collected. Anomalous features found in the geophysical data are hypothesized to have formed as a results of the simultaneous impact of a smaller meteorite fragment derived from the main meteorite. Both preferential erosion and the effect of existing topography are not considered likely causes of the unique crater shape due to the extremeness of the required preferential erosion and the lack of topographic features in the area surrounding the crater respectively.

The main crater diameter is suggested to have been ~120 m as evidenced by the projection of the ERT data and the exposed “graphyea bed” identified by *Evans and Mear* (2000). The depth of the base of the ejecta fill layer in the main crater is identified at 900 m elevation by ERT azimuth lines 13-6 and 10-1 and confirmed by *Evans and Mear* (2000) mine shaft measurements. The maximum height of the current rim is located at 933.5 m suggesting that the original crater depth was ~35m. The depth-to-diameter ratio for the main Odessa Meteorite Crater would then be ~0.29 which is within the range described by *Melosh* (1989). The hypothesized secondary crater is suggested to be ~50 m in diameter, however, further testing is needed. The base of ejecta fill of the secondary crater appears at 915 m elevation suggesting a depth of ~20 m, but no available core data confirms this.

More ERT data over the possible secondary crater would benefit further studies and increase confidence in results. Further high-resolution GPR data could be used to more quantitatively analyze facture content in the rest of the crater. However, considering all factors, it can be concluded that the main Odessa Meteorite Crater was indeed circular at the time of formation. Future estimations of the impactor size, velocity, and trajectory should consider an initial crater of 120 m diameter and 35 m depth.

REFERENCES

Allred, K. (2004), Some Carbonate Erosion Rates of Southeast Alaska, *Journal of Cave and Karst Studies*, *66*(3), 89-97.

Baldwin, R. B. (1963), *The Measure of the Moon*, 488 pp., University of Chicago Press Chicago.

Barringer, D. M. (1906), Coon Butte, Arizona, and the Canyon Diablo Meteorites, *American Journal of Science, Series*, *4*(21), 402-403.

Barringer Jr, D. M. (1928), A New Meteor Crater, *Proceedings of the Academy of Natural Sciences of Philadelphia*, *80*, 307-311.

Bibbins, A. B. (1926), A Small Meteor Crater in Texas, *Engineering & Mining*, *121*.

Boggess, A., and F. J. Narcowich (2015), *A First Course in Wavelets with Fourier Analysis*, 400 pp., John Wiley & Sons, New Jersey.

Bracewell, R. N., and R. N. Bracewell (1986), *The Fourier Transform and its Applications*, McGraw-Hill New York.

Briaud, J.-L. (2008), Case Histories in Soil and Rock Erosion: Woodrow Wilson Bridge, Brazos River Meander, Normandy Cliffs, and New Orleans Levees, *Journal of Geotechnical and Geoenvironmental Engineering*, *134*(10), 1425-1447.

Cassidy, N. J. (2009), Ground Penetrating Radar Data Processing, Modelling and Analysis, in *Ground penetrating radar: theory and applications*, edited by H. M. Jol, pp. 141-176, Elsevier, Oxford, UK.

Chao, E. C. T. (1966), Impact Metamorphism, edited by U. S. G. Survey, pp. 135-167, Washington D. C.

Commer, M., and G. Newman (2009), Three-Dimensional Controlled-Source Electromagnetic and Magnetotelluric Joint Inversion, *Geophysical Journal International*, *178*(3), 1305-1316.

Cucchi, F., F. Fabio, and F. Ulcigrai (1994), Degradation by Dissolution of Carbonate Rocks, *Acta Carsol*, *23*, 55-62.

Cucchi, F., F. Forti, and F. Finocchiaro (1987), Carbonate Surface Solution in the Classical Karst, *International journal of speleology*, *16*(3), 125-138.

Cucchi, F., F. Forti, and E. Marinetti (1996), *Surface Degradation of Carbonate Rocks in the Karst of Trieste (Classical Karst, Italy),* Universitat de les Illes Balears.

Davis, J. L., and A. P. Annan (1989), Ground-Penetrating Radar for High-Resolution Mapping of Soil and Rock Stratigraphy *Geophysical prospecting*, *37*(5), 531-551.

Dujardin, J.-R., and M. Bano (2013), Topographic Migration of GPR Data: Examples from Chad and Mongolia, *Comptes Rendus Géoscience*, *345*(2), 73-80.

Ellis, R. G. (1998), Inversion of Airborne Electromagnetic Data, *Exploration Geophysics*, *29*(2), 121-127.

Evans, G. L. (1961), Investigations at the Odessa Meteor Craters, paper presented at Proceedings of the Geophysical Laboratory/Lawrence Radiation Laboratory Cratering Symposium, Washington, DC.

Evans, G. L., and C. E. Mear (2000), *The Odessa Meteor Craters and Their Geological Implications*, 50 pp., Strecker Museum Complex, Baylor University.

Everett, M. E. (2013), *Near-Surface Applied Geophysics*, 403 pp., Cambridge University Press, New York.

Forti, F. (1984), Messungen des kKarsrabtrages in der Region Friul-Julische-Venetien, *Die Hohle*, *35*, 125-139.

French, B. M. (1998), *Traces of Catastrophe: A Handbook of Shock-Metamorphic Effects in Terrestrial Meteorite Impact Structures*, 120 pp., Lunar and Planetary Institute, Houston.

Furlani, S., F. Cucchi, F. Forti, and A. Rossi (2009), Comparison Between Coastal and Inland Karst Limestone Lowering Rates in the Northeastern Adriatic Region (Italy and Croatia), *Geomorphology*, *104*(1), 73-81.

Gault, D. E., W. L. Quaide, V. R. Oberbeck, B. M. French, and N. M. Short (1968), *Shock Metamorphism of Natural Materials*, 99 pp., Mono Book Corp., Baltimore, Md.

Goldman, M., A. Du Plooy, and M. Eckard (1994), On Reducing Ambiguity in the Interpretation of Transient Electromagnetic Sounding Data, *Geophysical prospecting*, *42*(1), 3-25.

Grieve, R. A. F. (1987), Terrestrial Impact Structures, *Annual Review of Earth and Planetary Sciences*, *15*(1), 245-270.

Hildebrand, A. R., M. Pilkington, C. Ortiz-Aleman, R. E. Chavez, J. Urrutia-Fucugauchi, M. Connors, E. Graniel-Castro, A. Camara-Zi, J. F. Halpenny, and D. Niehaus (1998), Mapping Chicxulub crater structure with gravity and seismic reflection data, *Geological Society, London, Special Publications*, *140*(1), 155-176.

Holliday, V. T. (1991), The Geologic Record of Wind Erosion, Eolian Deposition, and Aridity on the Southern High Plains, *Great Plains Research*, *1*(1), 6-25.

Holliday, V. T., D. A. Kring, J. H. Mayer, and R. J. Goble (2005), Age and Effects of the Odessa Meteorite Impact, Western Texas, USA, *Geology*, *33*(12), 945-948.

Inc., A. G. (2007), Earth Imager 2D Resistivity and IP Inversion Software, edited.

Jutzi, M., W. Benz, and P. Michel (2008), Numerical Simulations of Impacts Involving Porous Bodies: I. Implementing Sub-Resolution Porosity in a 3D SPH Hydrocode, *Icarus*, *198*(1), 242-255.

Kunaver, J. (1979), Some Experiences in Measuring the Surface Karst Denudation in High Alpine Environment, *Actes du Symposium international sur l'érosion karstique*, 75-85.

Lehmann, F., and A. G. Green (2000), Topographic Migration of Georadar Data: Implications for Acquisition and Processing, *Geophysics*, *65*(3), 836-848.

Leuschen, C. J., and R. G. Plumb (2001), A Matched-Filter-Based Reverse-Time Migration Algorithm for Ground-Penetrating Radar Data, *IEEE Transactions on Geoscience and Remote Sensing*, *39*(5), 929-936.

Littlefield, D. L., P. T. Bauman, and A. Molineux (2007), Analysis of Formation of the Odessa Crater, *International journal of impact engineering*, *34*(12), 1953-1961.

Liu, Z.-h., K.-y. Wu, L. Q. Wang, H. L. Sun, and J. Han (2006), In Situ Precise Measurement of Erosion Rates of Carbonate Rock Blocks Under Flowing Non-Karst Water Using Micro-Erosion Meter and the Rate-Determining Factors, *Geochimica*, *35*(1), 1-5.

Loke, M. H. (1999), Electrical Imaging Surveys for Environmental and Engineering Studies, edited, pp. 1-60, Universiti Sains Malaysia, Malaysia.

Mallat, S. G. (1989), A Theory for Multiresolution Signal Decomposition: the Wavelet Representation, *IEEE transactions on pattern analysis and machine intelligence*, *11*(7), 674-693.

McGlaun, M., S. L. Thompson, and M. G. Elrick (1990), CTH: a Three-Dimensional Shock Wave Physics Code, *International Journal of Impact Engineering*, *10*(1-4), 351-360.

Melosh, H. J. (1989), *Impact cratering: A Geologic Process*, 253 pp., Oxford University Press, New York.

Merrill, G. P. (1922), Meteoric Iron from Odessa, Ector County, Texas, *American Journal of Science*(17), 335-337.

Monnig, O. E., and R. Brown (1935), The Odessa, Texas, Meteorite Crater, *Contributions of the Society for Research on Meteorites*, *1*(1), 1-4.

Muhammad, R. F., and Y. E. Beng (2002), Estimating Limestone Dissolution Rates in the Kinta and Lenggong Valleys Using the Micro Erosion Meter; a Preliminary Study, *Bulletin Geological Society of Malaysia*, *45*, 253-256.

Nininger, H. H. (1933), 'Meteor Craters' vs. 'Steam Blowouts', *Mines Magazine*.

Nordyke, M. (1962), An Analysis of Cratering Data from Desert Alluvium, *Journal of Geophysical Research*, *67*(5), 1965-1974.

O'Neill, C., and C. Heine (2005), Reconstructing the Wolfe Creek Meteorite Impact: Deep Structure of the Crater and Effects on Target Rock, *Australian Journal of Earth Sciences*, *52*(4-5), 699-709.

Pierazzo, E., D. A. Kring, and H. J. Melosh (1998), Hydrocode Simulation of the Chicxulub Impact Event and the Production of Climatically Active Gases, *Journal of Geophysical Research: Planets*, *103*(E12), 28607-28625.

Pierazzo, E., and H. J. Melosh (1999), Hydrocode Modeling of Chicxulub as an Oblique Impact Event, *Earth and Planetary Science Letters*, *165*(2), 163-176.

Roy, A. (1962), Ambiguity in Geophysical Interpretation, *Geophysics*, *27*(1), 90-99.

Schmidt, R. M., and K. R. Housen (1987), Some Recent Advances in the Scaling of Impact and Explosion Cratering, *International Journal of Impact Engineering*, *5*(1-4), 543-560.

Sellards, E. H. (1927), Unusual Structural Features in the Plains region of Texas, *Geological Society of America Bulletin*, *28,* 149-149.

Sellards, E. H., and G. L. Evans (1941), Statement of Progress of Investigation at Odessa Meteor Craters*Rep.*, 1-15 pp, University of Texas, Bureau of Economic Geology.

Shoemaker, E. M. (1959), Impact Mechanics at Meteor Crater, Arizona*Rep. 2331-1258*, 1-55 pp, US Geological Survey.

Shoemaker, E. M., and R. E. Eggleton (1961), Terrestrial Features of Impact Origin, paper presented at Proceedings of the Geophysical Laboratory–Lawrence Radiation Cratering Symposium.

Smith, D. I., M. A. Greenaway, C. Moses, and A. P. Spate (1995), Limestone Weathering in Eastern Australia. Part 1: Erosion Rates, *Earth Surface Processes and Landforms*, *20*(5), 451-463.

Stephenson, W. J., and B. L. Finlayson (2009), Measuring Erosion with the Micro-Erosion Meter-Contributions to Understanding Landform Evolution, *Earth-Science Reviews*, *95*(1), 53-62.

Stöffler, D. (1971), Progressive Metamorphism and Classification of Shocked and Brecciated Crystalline Rocks at Impact Craters, *Journal of Geophysical Research*, *76*(23), 5541-5551.

Streich, R., and J. Van der Kruk (2007), Accurate Imaging of Multicomponent GPR Data Based on Exact Radiation Patterns, *IEEE Transactions on Geoscience and Remote Sensing*, *45*(1), 93-103.

Trudgill, S. T. (1986), Limestone Weathering Under a Soil Cover and the Evolution of Limestone Pavements, Malham district, North Yorkshire, UK, in *New direction in Karst*, edited by K. Paterson and M. M. Sweeting, pp. 461-471, Geo books, Norwich.

Wiggins, J. W. (1984), Kirchhoff Integral Extrapolation and Migration of Nonplanar Data, *Geophysics*, *49*(8), 1239-1248.

Wünnemann, K., G. S. Collins, and H. J. Melosh (2006), A Strain-Based Porosity Model for Use in Hydrocode Simulations of Impacts and Implications for Transient Crater Growth in Porous Targets, *Icarus*, *180*(2), 514-527.

Yilmaz, Ö. (2001), *Seismic Data Processing*, Society of Exploration Geophysicsists, Tulsa, Ok.